CNWRA 94-013

GEOPHYSICS REVIEW TOPICAL REPORT: APPLICATION OF SEISMIC TOMOGRAPHIC AND MAGNETIC METHODS TO ISSUES IN BASALTIC VOLCANISM

Prepared for

Nuclear Regulatory Commission
Contract NRC-02-93-005

Prepared by

Center for Nuclear Waste Regulatory Analyses
San Antonio, Texas

June 1994

CNWRA 94-013

GEOPHYSICS REVIEW TOPICAL REPORT: APPLICATION OF SEISMIC TOMOGRAPHIC AND MAGNETIC METHODS TO ISSUES IN BASALTIC VOLCANISM

Prepared for

Nuclear Regulatory Commission
Contract NRC-02-93-005

Prepared by

Charles B. Connor

Center for Nuclear Waste Regulatory Analyses
San Antonio, Texas

Christopher O. Sanders

Department of Geology
Arizona State University

June 1994

PREVIOUS REPORTS IN SERIES

Number	Name	Date Issued
20-5704-141-001	Technical and Regulatory Bases for the Study of Recently Active Cinder Cones	8/93

ABSTRACT

Models of the probability and consequences of volcanic activity in the Yucca Mountain region (YMR) indicate that: (i) volcanism is of regulatory concern, and (ii) the recurrence rate of volcanism in the YMR changes by more than two orders of magnitude within 20 km of the candidate repository site. This distance is on the scale of many geologic structures, including faults and dikes. This, in turn, indicates that additional geologic and geophysical data and the incorporation of these data into volcanism models may provide realistic bounds on probability estimates of volcanic hazards in the YMR. Four areas of research in basaltic volcanism in which geophysical methods may be used to reduce uncertainty are: (i) identification and mapping of shallow igneous features that lack surface expression, (ii) identification and mapping of high-temperature subsolidus or partial-melt zones in the upper mantle and crust, (iii) estimation of the volume of rock likely disrupted by effusive and explosive volcanism, and (iv) determination of the relationship between igneous features and geologic structure. The goal of this study is to review the utility and limitations of seismic tomographic and magnetic methods for use in reducing uncertainties related to volcanic processes in the YMR.

Seismic tomography has been demonstrated to be an effective technique for mapping magmatic bodies in volcanic fields. Techniques in seismic tomography for the inversion of traveltime residuals are reviewed. Comparatively low resolution is achieved in experiments using teleseisms in contrast to active sources. Results of a synthetic tomography experiment, using current velocity models for the YMR, indicate that small-velocity anomalies can be distinguished in the shallow crust using approximately 100 stations distributed over a 100-km^2 area and eight high explosive detonations located 50 km from the site. This type of detailed survey is important to site characterization. Seismic tomography and refraction experiments suggest that volume percent intrusives beneath cinder cone alignments and isolated cinder cones can be determined for expected intrusion volumes. Longer term, passive tomography experiments using teleseisms may be useful in identifying thermal anomalies associated with Recent basaltic volcanism.

Aeromagnetic and ground magnetic methods are capable of resolving shallow igneous rocks in fortuitous circumstances. Parametric studies and literature review indicate that shallow basalts cannot be unambiguously identified in tuff or shallow alluvium overlying a magnetic basement using magnetic methods. Estimates of the recurrence rate of volcanism in the YMR should account for this uncertainty. Numerical experiments using digital elevation models indicate the effects of magnetized topography on anomalies produced by shallow dikes. Frequency domain filtering of low-level (150 m) draped aeromagnetic data, especially calculation of the second vertical derivative of total magnetization, provides evidence of the extent of buried dikes. Large shallow dikes or dike swarms cannot be imaged by aeromagnetic surveys made at elevations of 450 m or more in basaltic terrains.

Integrated geophysical surveys across cinder cone alignments in alluvium or sedimentary rock hold the most promise for imaging dike geometry and volume at repository depths.

CONTENTS

CONTENTS (Cont'd)

CONTENTS (Cont'd)

FIGURES

FIGURES (Cont'd)

TABLES

NOMENCLATURE

Symbols used in Section I: Introduction

m = number of near-neighbor volcanoes
t_i = time elapse since the formation of the i^{th} nearest-neighbor volcano
u_i = area of a circle whose radius is the distance from the point (x,y) to the i^{th} nearest volcano

Greek:

$\lambda_r(x,y)$ = recurrence rate at a point

Symbols used in Part I: Seismic Tomography

$\mathbf{A}$ = matrix with partial derivatives of the traveltimes
A = seismic wave amplitude
A_0 = initial seismic wave amplitude
A_P = amplitude of the P-wave
A_R = amplitude spectrum along reference ray
A_r = amplitude spectrum of seismic waves along r
A_S = amplitude of the S-wave
$\mathbf{C}$ = covariance matrix relating error in solution to data error
$\mathbf{d}$ = vector of hypocentral and slowness model parameters adjustments
f = wave frequency
G = geometric spreading
$\mathbf{G}$ = vector of geometric spreading factors
$\mathbf{H}$ = matrix with partial derivatives of traveltime with respect to hyprocentral parameters
$\mathbf{h}$ = vector of adjustments of hypocentral parameters
I = instrument response
$\mathbf{I}$ = identity matrix
k_1 = constant relating instrument response to incident waves
k_2 = constant relating slowness of P-and S-waves at source
k_3 = constant ratio of average Q_P/Q_S in crust
$\mathbf{L}$ = matrix of raypath lengths in individual blocks
L_r = total length of ray r
$\mathbf{M}$ = matrix with partial derivatives of traveltime with respect to slowness model parameters
$\mathbf{m}$ = vector of adjustments to slowness model parameters
l = distance along a raypath
l_{rb} = length of raypath r in block b
P = primary wave
P_g = P-wave refracted on Gutenberg Discontinuity
P_n = P-wave refracted on Mohorovitchic Discontinuity
PMP = P-wave that has passed through the mantle
Q = spatial attenuation factor
Q_i = spatial attenuation factor for seismic wave at receiver i

NOMENCLATURE (Cont'd)

Q_P = P-wave spatial attenuation factor
Q_S = S-wave spatial attenuation factor
$\mathbf{R}$ = resolution matrix
R = reference raypath
r = a seismic raypath
S = secondary wave
S_V = vertical component of the S-wave
$\mathbf{s}$ = vector of slowness perturbations
s = wave slowness
s_{est} = least-squares estimate of s
t = traveltime
$\mathbf{t}$ = vector of traveltime residuals
t_a = arrival time
t_o = origin time
t_P = P-wave traveltime
t_R^* = attenuation along a reference raypath
t_r^* = attenuation along raypath r
t_S = S-wave traveltime
t_t = total traveltime
V = seismic wave velocity
V_b = average block velocity
V_i = velocity of seismic wave at receiver i
V_P = velocity of the P-wave
V_S = velocity of the S-wave
$(V_P/V_S)_O$ = reference (average) value of V_P/V_S in the study volume

Greek:

ΔQ = deviation from the regional homogeneous Q along ray r
ΔQ_b = deviation from regional Q due to block b
Δs = slowness perturbation
Δs_b = slowness perturbation of block b
Δt_r = traveltime residual for ray r
Δt_t = traveltime residual
Δt_r^* = differential attenuation along raypath r
ΔV = deviation in velocity along raypath r
$\Delta(V_P/V_S)_b$ = V_P/V_S perturbation in block b
κ = bulk modulus
μ = shear modulus
ρ = density

σ_d^2 = variance of data
θ^2 = damping parameter
ν = Poisson's ratio

Symbols used in Part II: Magnetic Methods

$\mathbf{B}$ = magnetic induction
D_o = declination of the Earth's magnetic field
D_r = declination of remanent magnetization vector
$F(x,y)$ = Fourier transform of a magnetic map
$f(x,y)$ = grid representation of a magnetic map
$G(k_x,k_y)$ = product of Fourier transform of a magnetic map and map filter
$g(x,y)$ = grid representation of a filtered magnetic map
$\mathbf{H}$ = Earth's magnetic field
H = magnitude of the Earth's magnetic field
$H(k_x,k_y)$ = map filter
I_o = inclination of the Earth's magnetic field
I_r = inclination of remanent magnetization vector
i = imaginary number
$\mathbf{J}$ = intensity of magnetization
$\mathbf{J}_i$ = intensity induced magnetization
$\mathbf{J}_r$ = intensity of remanent magnetization
$\mathbf{J}_{tot}$ = total intensity of magnetization
J_x = x—component of the total intensity of magnetization
J_y = y—component of the total intensity of magnetization
J_z = z—component of the total intensity of magnetization
k = rock magnetic susceptibility
k_x = wavenumbers in the x direction
k_y = wavenumbers in the y direction
L,M,N = direction cosines for remanent magnetization vector
l,m,n = direction cosines for induced magnetization vector
$\mathbf{R}$ = vector of distance and direction to volume element
R = distance to volume element
T = total magnetic anomaly
V_1-V_6 = volume integrals
x,y,z = orthogonal coordinate system

Greek:

ΔX = magnetic intensity in x direction
ΔY = magnetic intensity in y direction
ΔZ = magnetic intensity in z direction

NOMENCLATURE (Cont'd)

μ = magnetic moment
μ_o = magnetic permeability
Ω = magnetic potential

Acronyms:

ACH = Aki, Christopherson, and Husseby inversion method
ART = Algebraic Reconstruction Technique
CDS = Compliance Determination Strategy
CNWRA = Center For Nuclear Waste Regulatory Analyses
DEM = Digital Elevation Model
DOE = U.S. Department of Energy
FFT = Fast Fourier Transform
KTUs = Key Technical Uncertainties
LARP = License Application Review Plan
LSQR = Least-Squares Regression Algorithm
NeHT = Nercessian, Hirn, and Tarantola inversion method
NRC = Nuclear Regulatory Commission
SI = International System of Units
SIRT = Simultaneous Iterative Reconstruction Technique
SwRI = Southwest Research Institute
TM = Thematic Mapper
YMR = Yucca Mountain region

ACKNOWLEDGMENTS

This report was prepared to document work performed by the Center for Nuclear Waste Regulatory Analyses (CNWRA) for the Nuclear Regulatory Commission (NRC) under Contract No. NRC-02-93-005. The activities reported here were performed on behalf of the NRC Office of Nuclear Regulatory Research, Division of Regulatory Applications. The report is an independent product of the CNWRA and does not necessarily reflect the views or regulatory position of the NRC.

The assistance of Jorge Parra of Southwest Research Institute (SwRI) in preparing some of the codes for magnetic calculations is appreciated. Mike Conway of Florida International University kindly provided details of his magnetic and gravity studies in the San Francisco volcanic field. Ron Martin was instrumental in preparing the digital elevation data and Landsat Thematic Mapper data used in this report. Stefan C. Ponko, Joyce Foegelle, and Ken D. Mahrer helped with literature compilations. Cathy Garcia, Esther Cantu, and Arturo Ramos formatted this report. The SwRI Publication Services provided important editorial and production assistance. The comments of H. Lawrence McKague, Renner Hofmann, and Ronald Green substantially improved this document.

QUALITY OF DATA, ANALYSES, AND CODE DEVELOPMENT

DATA: CNWRA-generated laboratory and field data contained in this report meet quality assurance requirements described in the CNWRA Quality Assurance Manual. This reader is referred to the original source documents for information regarding the quality assurance provisions used in collection and processing of other data.

ANALYSES AND CODES: Scientific/engineering computer codes used in analyses contained in this report are: ARC/INFO, and Spyglass Transform. These packages are standard and commercially available. Seismic tomographic and magnetic codes developed as part of this project meet quality assurance standards as outlined in the CNWRA Quality Assurance Manual.

EXECUTIVE SUMMARY

The objectives of this investigation are to review the application of geophysical methods in use in the YMR as part of site characterization, discuss the application of these methods in the context of volcanism studies, and explore the utility and limitations of geophysical methods in volcanism studies through presentation of parametric models and the results of numerical experiments. In the context of volcanism studies in the YMR, geophysical methods have, to date, been used primarily in the exploration for volcanic features that lack surface expression. This has included the use of broadband seismic tomographic methods to characterize the velocity structure of basaltic source regions in the mantle and aeromagnetic and ground magnetic surveys to search for buried basaltic centers in the Amargosa Valley. These two geophysical methods - seismic tomography and magnetics - will likely continue to be used to great extent in site characterization efforts related to volcanism. Furthermore, applications of these two methods currently hold the greatest promise of reducing uncertainties related to basaltic volcanism in the YMR. Although both of these methods have been used primarily for the exploration and identification of features related to basaltic and silicic volcanism, both methods hold potential for further application to other issues in volcanology, including characterization of intrusion volume and geometry, and determination of volumetric intrusion to extrusion ratio in the YMR. As a result, it is critical to grasp both the utility and limitations of these two geophysical methods in particular. This report reviews these two geophysical methods in detail and in the context of basaltic volcanism in the YMR.

A principle criticism of current models of volcanism, including probability models of the potential for volcanic disruption of the candidate repository, has been that these models have failed to incorporate basic geologic information in an adequate way. Results of this study indicate that probability models based on the distribution and timing of cinder cone volcanism can be significantly enhanced through the application of geophysical methods. Models of the consequences of volcanism on repository performance can also be improved through geophysical investigations. Therefore, an important consideration in future geophysical research in the YMR should be that this research encompass specific issues in volcanism related to probability and consequence model development. Basic areas of research in basaltic volcanism in which geophysical methods may be used to reduce Key Technical Uncertainties are:

- Identification and mapping of shallow igneous features that lack surface expression
- Estimation of the volume of rock at repository depths disrupted by magmatic activity
- Demonstration of the relationship between igneous features, such as cinder cones and dikes, to regional tectonic setting and local structures
- Identification and mapping of high-temperature subsolidus or partial-melt zones in the YMR

This report is divided into two parts. The first part, including sections 2 through 6, describes the use of seismic tomographic methods; the second part, sections 7 through 10, describes the application and limitations of magnetic methods.

In Section 2, the physical and mathematical foundations of seismic tomography are discussed. Seismic tomographic methods use perturbations in the arrival time of seismic waves and attenuation of these waves to (i) model the velocity structure of the earth, and (ii) differentiate between causes of these velocity anomalies, including rock saturation, pore and fracture density, and the presence of partial melt,

high-subsolidus temperatures, and gas. Seismic tomographic methods have been used successfully to delineate thermal anomalies in the Coso Volcanic Field, California, and other volcanic areas in the western United States.

Tomographic studies of regions with volcanic and geothermal activity are reviewed in section 3. This review is important because these investigations indicate the utility and limitations of tomographic methods and because it is possible to apply these or similar methods to problems in basaltic volcanism in the YMR. Seismic tomographic surveys conducted to date at the Nevada Test Site are also reviewed in this section. These surveys at the Nevada Test Site use comparatively low resolution techniques to identify broad low-velocity anomalies in the mantle beneath the YMR. Because first arrivals of P-waves were used, it is not possible to constrain the geologic cause of these anomalies, but they are likely related to the presence of anomalously high-temperature zones in the mantle.

Sections 4 and 5 discuss the application of seismic tomographic methods to (i) delineate small magma bodies at intermediate and shallow crustal depths, and (ii) determine intrusion volume and geometry beneath cinder cones, and cinder cone alignments. Three seismic tomography experiments are discussed in detail. The first of these experiments is a synthetic seismic tomographic survey centered on the Yucca Mountain site, involving the use of 100 sesimometers over an area of 100 km^2. Such a survey, using 8 high explosive detonations, is capable of resolving small (about 2 percent) velocity anomalies within 1 km^3 blocks. The second experiment describes a two-dimensional (2D) method of imaging deep and intermediate level magma bodies in cinder cone fields, and the third experiment describes tomographic and basic traveltime delay methods for imaging intrusion geometries. A 0.01 s delay is easily observed using common methods, a delay likely produced by intrusions related to cinder cone alignments if these intrusions consist of dike swarms rather than individual thin dikes.

Magnetic methods are reviewed in sections 7 through 10. Specific topics addressed include (i) discussion of the physical bases for magnetic methods and their application in geophysics, (ii) a brief review of the application of ground magnetic and aeromagnetic surveys to investigations in selected volcanic areas, (iii) a parametric study of the amplitude and wavelength of magnetic anomalies produced by dikes in the Tiva Canyon Tuff and alluvial valleys of the YMR, (iv) an investigation of the impact of magnetized terrain on our ability to identify intrusive structures near basaltic cinder cones and lava flows, and (v) application of frequency-domain map enhancement techniques for the delineation of subtle magnetic anomalies in complex, noisy magnetic environments.

Section 7 reviews the application of magnetic methods to the study of basaltic volcanic areas, including the Amargosa Desert. The identification of basalts related to aeromagnetic anomalies in the Amargosa Desert is important for two reasons. First, recognition of the anomalies indicates that shallow, buried extrusive, volcanic centers in the YMR can be identified using aeromagnetic data. By the same token, the aeromagnetic anomalies associated with these centers indicates the limitations of the method. These anomalies would not be identified in shallower parts of the Amargosa basin, where shallow basement and outcrops of Miocene tuff produce complex magnetic anomalies. Second, the anomalies are located close to Lathrop Wells and the cinder cones of Crater Flat. Recognition of the Amargosa Valley volcanic centers increases the number of volcanic centers in the area and indicates that small-volume basaltic volcanism has been widespread in the vicinity of Yucca Mountain since the Pliocene. The change in magnetic polarity of some of the anomalies indicates that these buried volcanic centers likely formed over a long period of time.

Parametric studies of ground and aeromagnetic anomalies related to igneous dikes are presented in Section 8. The results of the parametric study indicate that practical bounds can be placed on the utility of ground magnetic data for the identification and mapping of basaltic dikes and other volcanic features. It is apparent that the minimum amplitude anomaly likely to be resolved using ground magnetic data collected over alluvium in the YMR is on the order of 30 to 200 nT. High-frequency, large-amplitude fluctuations in the magnetization of the Paintbrush Tuff indicate that anomalies would normally need to exceed several hundred to thousands of nanoTeslas in order to be identified unambiguously. The magnitudes of these anomalies places bounds on the geometries of igneous dikes likely to be identified using magnetic methods. A 10-m-wide dike in alluvium, for example, penetrating to within 200 m of the surface would create a mappable ground magnetic anomaly. The same dike would not produce a mappable ground magnetic anomaly if it intruded the Tiva Canyon Tuff. A 1-m-wide dike would need to reach to within 20 m of the surface in alluvium to produce a magnetic anomaly similar to a 10-m-wide dike at repository depths.

Section 9 describes magnetic terrain corrections and the utility of frequency-domain map enhancement methods. It may be possible to map shallow igneous dikes beneath cinder cone alignments in some circumstances, but the anomalies associated with these dikes are likely to be subtle. Identification of dikes, the geometry of which is important in estimates of the probability and consequences of volcanism, is most likely through the use of draped aeromagnetic surveys at flight elevations of less than 150 m. Interpretation of this type of data likely requires the use of map enhancement techniques, including calculation of the second vertical derivative, in order to resolve the anomalies produced by intrusions. Forward modeling techniques are not as useful as map enhancement techniques for the identification and mapping of these dikes in most circumstances.

Identification of subsurface igneous features is a basic aspect of site characterization. The simulations and parametric studies presented in this report provide some bounds on the capability of seismic tomographic and magnetic surveys for the identification of subsurface igneous features. Basic conclusions with regard to application of these methods to this identification and mapping process are:

- Numerous seismic tomographic studies have demonstrated that this method is capable of resolving high-temperature and partial-melt zones in the crust and upper mantle. Recognition of these potential source zones for basaltic magma, or increased confidence in their absence, can help resolve uncertainty related to the application of probability models.

- The volume of the velocity anomalies that can be identified depends on survey design, the number of stations deployed and the station spacing, and the depth of the target anomaly.

- Synthetic tomography experiments at the site indicate that $1 \times 1 \times 1$ km low-velocity anomalies can be identified at shallow depths (<5 km) using approximately 100 stations distributed regularly in a 100-km^2 area. The results of such a survey would facilitate characterization of the geology of the site generally, and may help bound the intrusion/extrusion ratio of basalts in parts of the YMR. This detailed survey, coupled with lower resolution, deeper surveys may have an impact on probability calculations for volcanic disruption of the candidate repository and the results of these surveys should be considered in this context.

- Tomography surveys in other, younger, basaltic fields may provide evidence of the longevity of velocity anomalies related to small-volume basaltic volcanism.

- Ground and aeromagnetic data will not be useful in identifying shallow igneous features in the YMR, except where these features are located in alluvium that is deep with respect to the level of the igneous features. Therefore, recognition and mapping of aeromagnetic anomalies in the Amargosa Valley does not, in itself, indicate that all buried centers or significant intrusive structures have been identified in the YMR.

- Any result or interpretation of the recurrence rate of volcanism in the YMR based on the application of aeromagnetic methods must address the uncertainty of the geophysical method employed.

Analyses in this study indicate that specific seismic tomographic and refraction experiments can be designed to investigate the structure of feeder dike systems beneath cinder cone alignments. These experiments could be coupled with aeromagnetic and ground magnetic surveys. In both geophysical methods, the ability to resolve and map intrusion geometries depends on dike volume and contrast with the surrounding media. Numerous parameters, such as topographic complexity and magnetization contrast, impact the dike geometries that can be resolved using magnetic methods. Resolution of magnetic data can, under some circumstances, be enhanced through the application of frequency domain map enhancement techniques and statistical analysis of magnetic data. Thus, both methods are capable of resolving large shallow dikes or dike swarms that may be related to alignments or polycyclic activity. Conversely, neither of these methods is likely to identify small features, such as individual dikes, at repository depths. In either case, an investigation of a cinder cone alignment, for example the Crater Flat alignment, or a similar feature would place valuable constraints on models of repository disruption due to volcanism. Such data are not currently available. An investigation of this kind would impact volcanism models and performance assessment because: (i) the interpretation of structural controls on alignment evolution and understanding of the dynamics of this process may change; (ii) as a result, probability models may change; and (iii) such an investigation may alter current models of the volume of rock disrupted, and therefore the repository area affected, by igneous activity.

The relationship of basaltic volcanism to regional tectonic setting and structure is also best approached through integrated surveys. Determination of the tectonic setting of volcanic fields should include cross-correlation of LandSat Thematic Mapper data, long-wavelength geophysical data including gravity and magnetics, topographic information, and geological information. Cross-correlation is best handled quantitatively on a geographic information system platform. This approach will simplify superposition of disparate data sets such as aeromagnetic anomalies and TM imagery, and facilitate use of map enhancement techniques. Forward or inverse modeling of geophysical data, although valuable in many circumstances, is not likely to be as helpful as quantitative map analysis for establishing relationships between structure and magmatism in basaltic volcanic fields. On local scales, surveys can be designed to search for interaction between individual faults and dikes in three-dimensions. The strength of this approach lies in formulation of the volcanological problem rather than in application of geophysical methods.

1 INTRODUCTION

The Yucca Mountain region (YMR) has been the site of recurring small-volume basaltic eruptions during the last 10 million years (Crowe et al., 1983; Smith et al., 1990). This volcanic activity has led to the formation of numerous cinder cones, eight of which are less than 1.6 million years old. These volcanoes likely represent a range of eruptive activity, from extremely explosive eruptions to comparatively gentle effusive volcanic eruptions (Amos et al., 1983; Crowe et al., 1983, 1986; Valentine et al., 1992, 1993). The technical objectives of the Field Volcanism project are to better characterize the effect of this type of volcanic activity on repository performance and, as a result, better constrain probability models of disruption of the repository. This characterization will be possible through investigation of the: (i) mechanics of mafic cinder cone eruptions, (ii) extent and characteristics of shallow hydrothermal systems and diffuse degassing associated with small-volume mafic eruptions, and (iii) nature and distribution of mafic intrusions in the YMR. Investigation of the third item, nature and distribution of mafic intrusions, requires the use of geophysical methods to explore for and describe igneous features. As geophysical methods are generally indeterminate, it is critical to understand the application and limitations of these methods in the context of their use in site characterization in general, and in issues related to basaltic volcanism specifically.

This report summarizes Center for Nuclear Waste Regulatory Analyses (CNWRA) research conducted during 1993 and 1994 on the applications and limitations of geophysical methods to the study of intrusive or buried extrusive basalts. The objective of this summary is to review the application of geophysical methods in use in the YMR as part of site characterization (e.g., Oliver et al., 1990), discuss the application of these methods in the context of volcanism studies (Crowe et al., 1993; Connor and Hill, 1993; Valentine et al., 1992), and explore the utility and limitations of geophysical methods in volcanism studies through presentation of parametric models and the results of numerical experiments. In the context of volcanism studies in the YMR, geophysical methods to date have been used primarily in the exploration for volcanic features that lack surface expression. These methods have included the use of broadband seismic tomographic methods to characterize the velocity structure of basaltic source regions in the mantle (Evans and Smith, 1992) and the use of aeromagnetic and ground magnetic surveys to search for buried basaltic centers in the Amargosa Valley (Langenheim et al., 1993; Ponce et al., 1992). These two geophysical methods — seismic tomography and magnetic — will likely continue to be used to great extent in site characterization efforts related to volcanism (Crowe et al., 1993). Furthermore, applications of these two methods currently hold the greatest promise of reducing uncertainties related to basaltic volcanism in the YMR. Although both methods have been used primarily for the exploration and identification of features related to basaltic and silicic volcanism (Evans and Smith, 1992; Langenheim et al., 1993), they hold potential for further application to other issues in volcanology, including characterization of intrusion volume and geometry and determination of volumetric intrusion to extrusion ratio in the YMR. As a result, it is critical to understand both the utility and limitations of these two geophysical methods in particular. This report reviews these two geophysical methods in detail in the context of basaltic volcanism in the YMR.

1.1 REGULATORY FRAMEWORK

This review of the application and limitations of seismic tomographic and magnetic methods in the study of basaltic volcanism in the YMR will be used to support specific sections of the License Application Review Plan (LARP). Insight into the frequency, distribution, and volume of basaltic magmatism in the YMR, the areas most affected, both at repository and regional scales, and the

relationship between volcanism and regional tectonic and structural settings, form an integral part of site characterization activities (evidence of igneous activity as a potentially adverse condition, LARP Section 3.2.1.9; and impact of volcanism on groundwater movement, LARP Section 3.2.2.7), and the description of overall system performance (assessment of compliance with the requirement for cumulative releases of radioactive materials, LARP Section 6.1). The Compliance Determination Strategy (CDS) associated with evidence of Quaternary volcanism is of Type 5, indicating that independent research must be conducted to evaluate Key Technical Uncertainties (KTUs) associated with volcanism and that volcanism poses a high risk to the Nuclear Regulatory Commission (NRC) of reaching unwarranted conclusions regarding compliance with 40 CFR Part 191 and 10 CFR 60.122(c)(15). For example, until the limitation of knowledge of the frequency and volume of Quaternary-ages basaltic dikes in the YMR has been ascertained, it will be difficult to ascertain compliance with 10 CFR Part 60.

Four KTUs related to igneous activity, identified as part of the CDS concerned with evidence of Quaternary igneous activity, are addressed through application of geophysical methods in volcanology. These KTUs are:

- Low resolution of exploration techniques to detect and evaluate igneous features
- Inability to sample igneous features
- Development and use of conceptual tectonic models as related to igneous activity
- Prediction of future system states (disruptive scenarios)

Evaluation of these KTUs requires detailed safety review supported by analyses (Type 4), independent tests, and other investigations (Type 5).

In addition to evaluation of these KTUs, independent research in volcanism is needed to provide a basis to question how the U.S. Department of Energy (DOE) research will address the potential consequences of igneous activity on repository performance, and to evaluate the DOE responses to these questions.

1.2 TECHNICAL BASIS FOR REVIEW OF GEOPHYSICAL METHODS IN VOLCANOLOGY

A principal criticism of current models of volcanism, including probability models of the potential for volcanic disruption of the candidate repository, has been that these models have failed to adequately incorporate basic geologic information (Trapp and Justus, 1992). Probability models for the potential magmatic disruption of the candidate repository are generally based on the timing and distribution of past events. In Performance Assessment activities, the probability of volcanism and the consequences of such activity are used to make a risk assessment for this disruptive scenario class. Probability models that have been used to estimate the probability of disruption to date include:

- Homogeneous Poisson
- Weibull-Poisson

- Near-neighbor nonhomogeneous Poisson
- Spatio-temporal Markov

These models are based on the distribution and timing of past volcanic events. For example, in the nonhomogeneous Poisson model, the recurrence rate at a point, $\lambda_r(x,y)$, is estimated based on the age and distribution of near-neighbor volcanoes. A nonparametric estimate of $\lambda_r(x,y)$ can be found using varying numbers of near neighbors

$$\lambda_r(x,y) = \frac{m}{\sum_{i=1}^{m} u_i t_i} \tag{1-1}$$

where m near-neighbor volcanoes are determined as the minimum, $u_i t_i$, t_i is the time elapsed since the formation of the i^{th} near-neighbor volcano, and u_i is defined as the area of a circle whose radius is the distance from the point (x,y) to the i^{th} nearest volcano, with $u_i \geq 1$ km^2 (Connor and Hill, 1993). Using this approach, it is possible to estimate the probability of a volcanic event within a given area over the YMR. Using an area of 8 km^2, roughly the area of the repository, and a 10,000-yr period of interest, a spatially and temporally nonhomogeneous Poisson model can be used to calculate a probability map (Figure 1-1). This map indicates the probability of volcanism occurring in a given location in the YMR during the next 10,000 yr. The map indicates that the probability of volcanism in the next 10,000 yr is greatest in the Crater Flat area, roughly 15 km from the proposed repository site, and decreases with distance from this area. The probability of volcanic disruption of the repository itself is between 1×10^{-4} to 3×10^{-4} using this model. This range of estimates results from uncertainty in the ages of volcanoes in the YMR and uncertainty in the volume of rock likely disrupted by future volcanism.

Other probability models yield other estimates of the probability of disruption. But two general statements can be made at this time with confidence about volcanism in the YMR based on models proposed to date (Crowe et al., 1993; Ho et al., 1991; Connor and Hill, 1993). First, the probability of volcanic disruption of the repository is greater than 1 in 10,000 in 10,000 yr. This probability indicates that the volcanism disruptive scenario is of regulatory concern. Second, the probability of a new volcano forming in a specific location varies across the YMR, from comparatively high probabilities in the Crater Flat area to comparatively low values east of the candidate repository site. This probability variation, all within 20 km of the candidate site, occurs over a distance comparable to the scale of many geologic structures, such as faults and dikes or dike swarms. Therefore, it seems evident that it is auspicious to evaluate and enhance probability models through the investigation and integration of geological and geophysical data.

The application of geophysical methods to volcanological problems may directly influence probability calculations. For example, all recurrence rate models for basaltic volcanism in the YMR depend on the frequency and distribution of past volcanism [e.g., Eq. (1-1)]. A straightforward application of geophysics is the identification and mapping of volcanic centers that have been buried by sedimentation in alluvial basins. Recognition of buried centers through aeromagnetic surveys (Langenheim et al., 1993) has changed estimates of the recurrence rate of volcanism in the YMR. Another example of the application of geophysical methods in volcanic hazard assessment involves the use of seismic tomography. As presented in the section on seismic tomographic applications in volcanic fields, a

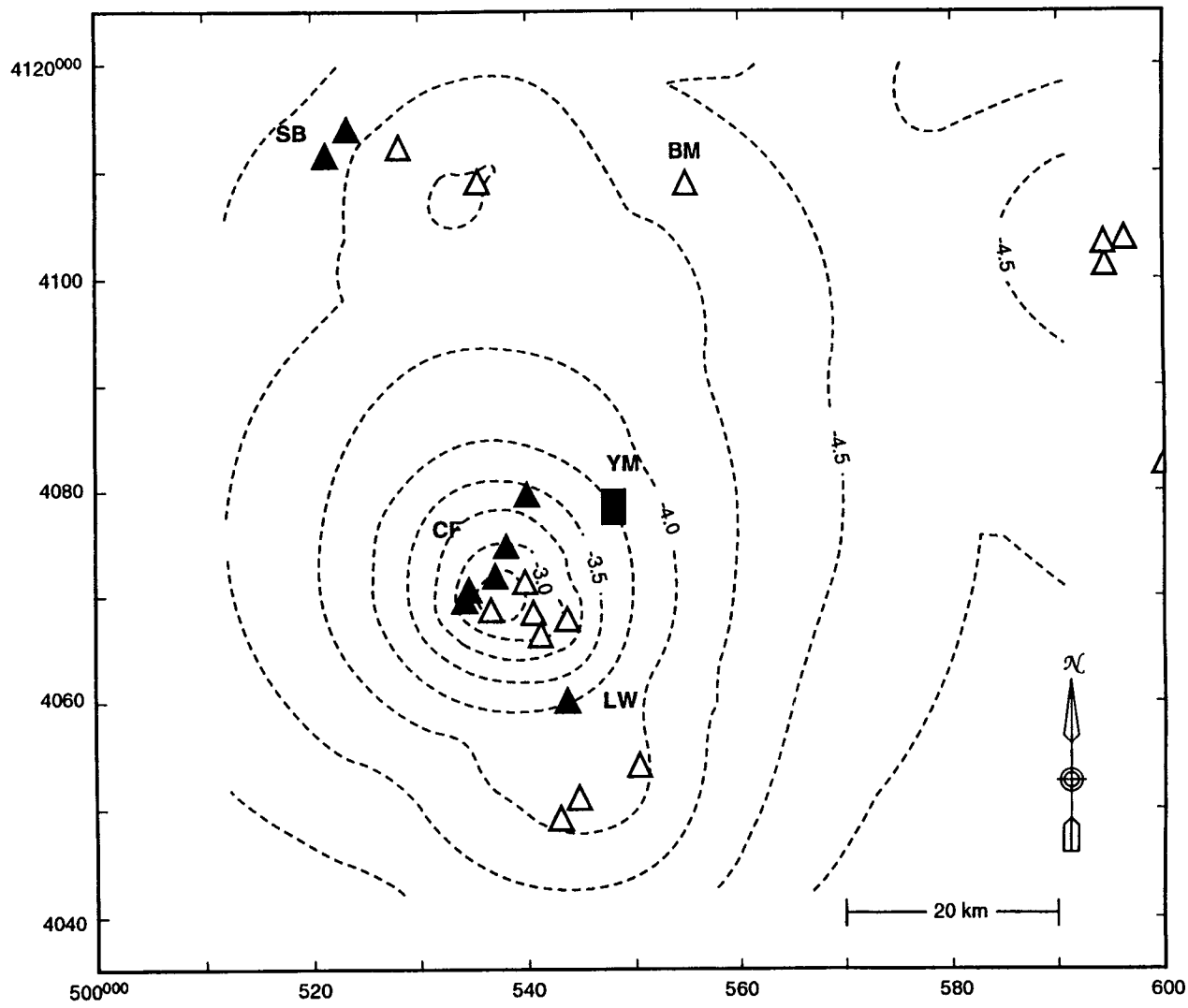

Figure 1-1. Example of a probability calculation for volcanism in the YMR. The probability of a volcano forming within an 8 km^2 area in 10,000 yr is contoured logarithmically. Note that the probability of volcanism changes by more than two orders of magnitude across the map area. Details of this calculation are presented in Connor and Hill (1993). Solid triangles — Quaternary centers, open triangles —Pliocene centers.

midcrustal low-velocity zone, likely related to partial melt, is located near, but south of the bimodal Coso volcanic field, California (Duffield and Roquemore, 1988; Sanders et al., 1988). Volcanism in this field has shown a progressive southward shift through time (Duffield et al., 1980), and the location of the velocity anomaly is consistent with this shift. The tomographic information supports a shift in the locus of volcanism, based on patterns and in the distribution and timing of cinder cone eruptions. Such empirical evidence can lend credence to the application of probability models and identify their limitations. However, the limitations of the geophysical methods themselves must also be thoroughly accounted for if such an application is to be used with confidence.

Four basic areas of research in basaltic volcanism in which geophysical methods may be used to reduce KTUs and enhance models of volcanic processes are:

- Identification and mapping of shallow igneous features that lack surface expression
- Estimation of the volume of rock at repository depths disrupted by magmatic activity
- Demonstration of the relationship between igneous features, such as cinder cones and dikes, to regional tectonic setting and local structures
- Identification and mapping of high-temperature subsolidus or partial-melt zones in the YMR

To date, geophysical methods have been applied to two of these problems: identification and mapping of shallow igneous features that lack surface expression, through the application of aeromagnetic methods (Langenheim et al., 1993; Crowe et al., 1993), and the search for high-temperature subsolidus or partial-melt zones in the YMR, through the application of teleseismic tomographic methods (Evans and Smith, 1992).

1.2.1 Identification and Mapping of Shallow Igneous Features

Most probability models for disruption of the candidate repository are based on the number and distribution of volcanic vents (e.g., Connor and Hill, 1993). This type of model may not encompass the hazards due to magmatic activity, if the number of magmatic events in the region is under-represented by the number of exposed volcanic centers. The recognition of the Amargosa Valley aeromagnetic anomalies, and subsequent determination that these anomalies are caused by buried extrusive basalts (Langenheim et al., 1993), is indicative of the need to thoroughly understand of the relationship between mappable volcanic units and magmatic events.

Furthermore, it is possible that dike intrusion, without accompanying eruptive activity, may impact repository performance. For example, a dike may propagate upward to shallow depths, then degas quietly over a long period of time. This event may alter the regional hydrologic setting, and volcanic gases escaping from the cooling dike may adversely affect geochemical transport near the repository site. Also, as the candidate repository is planned to be located 300 m below the crest of Yucca Mountain, a shallow intrusion that normally would not have reached the surface may intersect the repository, causing direct magmatic disruption. Consequently, it is important to attempt to quantify the intrusion to extrusion ratio, especially the number and volume of dikes that reach the near surface (<1 km) without accompanying eruptive activity.

It is difficult to quantify this ratio in active and recently active volcanic fields, simply because the extrusive rocks often form a thick sequence. There is little chance that intrusive rocks will actually crop out in this type of setting. The application of magnetic and seismic tomographic methods to these problems is discussed in detail in the following sections.

1.2.2 Areas Disrupted by Magmatic Activity

Models for the probability of volcanic disruption of the candidate repository are strongly affected by the volume, orientation, shape, and frequency of dike intrusion used in performance assessment and related models (e.g., Barr et al., 1993). This large effect is primarily because the number of containers that are affected by igneous intrusion depends on the shape and volume of the intrusion. Single thin basaltic dikes, for example, will not intersect as many waste packages as wide dikes or a dike swarm. Furthermore, more explosive styles of small-volume basaltic volcanism, such as hydromagmatic events (Crowe et al., 1986; Valentine et al., 1993), would likely disrupt a larger area than simple dike injection.

Potential field methods have been used to gain insight into the structure of basaltic volcanoes and style of volcanic eruptions (e.g., Rout et al., 1993). Geophysical methods can assist in the determination of the areas and depths to which country rock is disrupted by explosive eruptions. For example, M. Conway[1] made a gravity and magnetic survey across a tuff ring in the San Francisco volcanic field, Arizona. This tuff ring contains abundant crustal xenoliths, including Vishnu Schist, indicating transport of crustal xenoliths from depths greater than 300 m. Conway found a robust -3 mGal gravity anomaly across the tuff ring. He modeled this anomaly using a series of concentric circular disks of varying radii, and reaching a depth of approximately 300 m. The radius of the deepest disk was 25 m in Conway's model. As gravity data are indeterminate, other equally valid models could be developed. One method of addressing this indeterminacy is through the use of other geophysical surveys and geologic data. In this case, the presence of abundant Vishnu xenoliths supports the idea that significant areas of country rock were brecciated at depths of several hundred meters, creating the observed gravity anomaly.

Identification of the area affected by dike injection is more problematic. Dike injection will not produce the volume-density contrast needed for successful application of gravity methods. However, in some cases magnetic methods have provided substantive insight into dike geometry and distribution (e.g., Cole and Hunt, 1968). In the following sections, magnetic and seismic tomographic methods for mapping dike injection beneath cinder cones and related features are discussed in detail.

1.2.3 Relationship of Dikes and Cinder Cones to Regional Tectonic and Local Structural Setting

Potential field and seismic methods are commonly used to develop a three-dimensional (3D) view of geologic structures, particularly on a regional scale. This is one of the primary goals of geophysical exploration in the YMR (Oliver et al., 1990). Numerous authors have noted the link between regional tectonic setting, local structures such as mappable faults, and cinder cone distribution on several scales (Nakamura, 1977; Connor, 1990; Parsons and Thompson, 1991; Stirewalt et al., 1992; Connor

[1] Conway, M.F. 1994. Written communication to C.B. Connor.

et al., 1992). The relationship between tectonic features and cinder cones in several volcanic fields in the western Great Basin has been reviewed by Connor and Hill (1994). Several probability models for volcanic disruption of the repository have suggested that structural control, and subsequent cinder cone alignment development, may greatly increase the risk of volcanic disruption of the repository (Ho et al., 1991; Smith et al., 1990). Models for the interaction between faults and dikes indicate that ascending dikes may be captured along steeply dipping fault zones over a range of depths (McDuffie et al., 1994; Connor et al., 1994), resulting in the lateral transport of magma as it ascends from depth. Thus, the relationship between magmatism and structure likely encompasses several scales and, likewise, may impact repository performance and our understanding of that performance in several ways. Geophysical data collected in the YMR (Oliver et al., 1990) and elsewhere in the western Great Basin may provide important insights into the relationship between magmatism and specific structural features at several scales.

Especially on regional scales, the identification of geophysical trends such as aeromagnetic anomalies, volcanological data such as cinder cone distribution and age information, and related data including radar and satellite imagery, can provide additional evidence of the regional settings of basaltic volcanic fields (e.g., Zoback et al., 1994). Such comparisons have been difficult in the past because of the varied data involved. However, development of regional tectonics and volcanological databases (Connor and Hill, 1994) will likely facilitate these types of comparisons.

1.2.4 Presence of Partial-Melt Zones and Magmatic Bodies

As discussed above, determining if partial-melt zones or magmatic bodies exist at mantle to intermediate crustal levels in the YMR would clearly impact estimates of the probability of volcanic disruption of the repository. Until recently, such an investigation would not have been tenable. However, seismic tomographic methods have been developed at a rapid rate that are capable of both identifying low-velocity zones and delineating their likely origin. These methods are applicable to a broad set of problems in volcanology and will no doubt constitute an important part of site characterization and evaluation (Evans and Smith, 1992; Crowe et al., 1993). As a result, it is critical to review tomographic methods and discuss their limitations, practicality, and utility for investigation of issues in basaltic volcanism.

1.3 SUMMARY AND RECOMMENDATIONS

Results of this study, presented in detail in the following sections, indicate that probability models based on the distribution and timing of cinder cone volcanism can be significantly enhanced through the application of geophysical methods. Models of the impact of volcanism on repository performance can also be improved through geophysical investigations. Therefore, an important consideration in future geophysical research in the YMR should be that this research encompass specific issues in volcanism related to probability and consequence model development. This does not mean that geophysical data, such as tomographic data, need be collected for the use of volcanologists alone, rather that the data should be used to address specific research goals in volcanology and that survey design should consider these issues. Basic areas of research in basaltic volcanism in which geophysical methods may be used to reduce KTUs and enhance models of volcanic processes are in the identification and mapping of igneous features, including high-temperature zones and dike geometries, and in the investigation of the relationship between volcanism and tectonics. Integration of geophysical surveys into

basic volcanological investigations can resolve regulatory uncertainties associated with these research topics.

Identification of subsurface igneous features is a basic aspect of site characterization. The simulations and parametric studies presented in this report provide some bounds on the capability of seismic tomographic and magnetic surveys for the identification of subsurface igneous features. Some basic conclusions with regard to application of these methods to this identification and mapping process are:

- Numerous seismic tomographic studies have demonstrated that this method is capable of resolving high-temperature and partial-melt zones in the crust and upper mantle. Recognition of these potential source zones for basaltic magma, or increased confidence in their absence can help resolve uncertainty related to the application of probability models.

- The volume of the velocity anomalies that can be identified depends on survey design, the number of stations deployed and the station spacing, and the depth of the target anomaly.

- Synthetic tomography experiments at the site indicate that $1 \times 1 \times 1$ km low-velocity anomalies can be identified at shallow depths (< 5 km) using approximately 100 stations in a 100-km^2 area. The results of such a survey would facilitate characterization of the geology of the site generally, and may help bound the intrusion/extrusion ratio of basalts in parts of the YMR. This detailed survey, coupled with lower resolution, deeper surveys may have an impact on probability calculations for volcanic disruption of the candidate repository and the results of these surveys should be considered in this context.

- Tomography surveys in other, younger, basaltic fields may provide evidence of the longevity of velocity anomalies related to small-volume basaltic volcanism.

- Ground and aeromagnetic data will not be useful in identifying shallow igneous features in the YMR, except where these features are located in alluvium that is deep with respect to the level of the igneous features. Therefore, recognition and mapping of aeromagnetic anomalies in the Amargosa Valley does not, in itself, indicate that all buried centers or significant intrusive structures have been identified in the YMR.

- Any result or interpretation of the recurrence rate of volcanism in the YMR based on the application of aeromagnetic methods must address the uncertainty of the geophysical method employed. Our parametric studies summarize the limits of the resolution of the magnetic methods [Figures 8-7(a) and 8-7(b)] for the identification of basaltic features in various magnetized terrains.

Analyses in this study indicate that specific seismic tomographic and refraction experiments can be designed to investigate the structure of feeder dike systems beneath cinder cone alignments. These experiments could be coupled with aeromagnetic and ground magnetic surveys. In both geophysical methods, the ability to resolve and map intrusion geometries depends on dike volume and contrast with the surrounding media. Traveltime anomalies on the order of 0.01 s, corresponding to dike volumes on the order of several percent, can be resolved using comparatively straightforward experimental designs. Numerous parameters, such as topographic complexity and magnetization contrast, impact the dike geometries that can be resolved using magnetic methods. Resolution of magnetic data can, under some

circumstances, be enhanced through the application of frequency domain map enhancement techniques and statistical analysis of magnetic data. Thus, both methods are capable of resolving large shallow dikes or dike swarms that may be related to alignments or polycyclic activity. Conversely, neither of these methods is likely to identify small features, such as individual dikes, at repository depths. In either case, an investigation of a cinder cone alignment, for example the Crater Flat alignment, or a similar feature would place valuable constraints on models of repository disruption due to volcanism. Such data are not currently available. An investigation of this kind would impact volcanism models and performance assessment because: (i) the interpretation of structural controls on alignment evolution and understanding of the dynamics of this process may change; (ii) as a result, probability models may change; and (iii) such an investigation may alter current models of the volume of rock disrupted, and therefore the repository area affected, by igneous activity.

The relationship of basaltic volcanism to regional tectonic setting and structure is also best approached through integrated surveys. Determination of the tectonic setting of volcanic fields should include cross-correlation of LandSat Thematic Mapper (TM) data, long-wavelength geophysical data including gravity and magnetics, topographic information, and geological information. Cross-correlation is best handled quantitatively on a geographic information system platform. This approach will simplify superposition of disparate data sets such as aeromagnetic anomalies and TM imagery (e.g., Figures 7-3 and 7-4), and facilitate use of map enhancement techniques. Forward or inverse modeling of geophysical data, although valuable in many circumstances, is not likely to be as helpful as quantitative map analysis for establishing relationships between structure and magmatism in basaltic volcanic fields. On local scales, surveys can be designed to search for interaction between individual faults and dikes in 3D. Again, the strength of this approach lies in formulation of the volcanological problem rather than in application of geophysical methods.

1.4 ORGANIZATION

The following sections provide review and analyses in support of the conclusions made above. These sections are divided into two parts: the first discusses seismic tomographic methods, the second discusses magnetic methods. Each part contains a background discussion on the method, examples of the application of the method in volcanology, and studies of the applicability and limitations of the method to regulatory issues related to basaltic volcanism. Sections 2–5 constitute a review of techniques, a discussion of previous studies, and analysis of the resolution of seismic tomographic methods. A synthetic seismic tomographic experiment is used to explore the application of the method in site characterization, and additional experiments are outlined to demonstrate the use of tomography in addressing issues in basaltic volcanism. Section 6 contains references cited in the seismic tomography sections. Section 7 provides an overview of magnetic methods and their application in volcanology, relying on several case studies of volcanoes. This section is followed by a parametric study used to develop bounds on the geometry of igneous features likely to be identified using magnetic and aeromagnetic techniques. In section 9, an analysis of the effects of magnetized terrain on total magnetic field anomalies is developed, using the Quaternary cinder cones of Crater Flat as an example. This is followed by a discussion of map enhancement techniques and their application to aeromagnetic data. References cited in the part on magnetics are given in section 10.

1.5 REFERENCES CITED IN SECTION 1

Amos, R.C., S. Self, and B.M. Crowe. 1983. Pyroclastic activity at Sunset Crater: Evidence of a large magnitude, high dispersal strombolian eruption. *Eos, Transactions of the American Geophysical Union* 62: 1,085.

Barr, G.E., E. Dunn, H. Dockery, R. Barnard, G. Valentine, and B. Crowe. 1993. *Scenarios Constructed for Basaltic Activity at Yucca Mountain and Vicinity*. SAND91-1653. Albuquerque, NM: Sandia National Laboratories.

Cole, J.W., and T.M. Hunt. 1968. Basaltic dikes of the Tarawera complex, New Zealand. *New Zealand Journal of Geology and Geophysics* 11: 1,203–1,206.

Connor, C.B. 1990. Cinder cone clustering in the TransMexican volcanic belt: implications for structural and petrologic models. *Journal of Geophysical Research* 95: 19,395–19,405.

Connor, C.B., and B.E. Hill. 1993. Estimating the probability of volcanic disruption at the Yucca Mountain site using nonhomogeneous Poisson models. *American Nuclear Society, Focus '93.* 174–181.

Connor, C.B., and B.E. Hill. 1994. *The CNWRA Volcanism Geographic Information System Database.* CNWRA 94-004. San Antonio, TX: Center for Nuclear Waste Regulatory Analyses.

Connor, C.B., C.D. Condit, L.S. Crumpler, and J.C. Aubele. 1992. Evidence of regional structural controls on vent distribution: Springerville volcanic field, Arizona. *Journal of Geophysical Research* 97: 12,349–12,359.

Connor, C.B., S.M. McDuffie, and B.E. Hill. 1994. Field Volcanism Research. *NRC High-Level Radioactive Waste Research at CNWRA, July–December 1993*. CNWRA 93-02S. San Antonio, TX: Center for Nuclear Waste Regulatory Analyses.

Crowe, B., S. Self, D. Vaniman, R. Amos, and F. Perry. 1983. Aspects of potential magmatic disruption of a high-level radioactive waste repository in southern Nevada. *Journal of Geology* 91: 259–276.

Crowe, B.M., K.H. Wohletz, D.T. Vaniman, E. Gladney, and N. Bower. 1986. *Status of Volcanic Hazard Studies for the Nevada Nuclear Waste Storage Investigations*. Report LA-9325-MS, Vol. II. Los Alamos, NM: Los Alamos National Laboratory.

Crowe, B.M., F.V. Perry, and G.A. Valentine. 1993. *Preliminary Draft: Status of Volcanic Hazard Studies for the Yucca Mountain Site Characterization Project.* Los Alamos, NM: Los Alamos National Laboratory.

Duffield, W.A., and G.R. Roquemore. 1988. Late Cenozoic volcanism and tectonism in the Coso Range area, California. *This Extended Land: Geological Journeys in the Southern Basin and Range.* D.L. Weide and M.L. Farber, eds. Geological Society of America, Cordilleran Section Field Trip Guidebook. Las Vegas, NV: University of Nevada: 159–176.

Duffield, W.A., C.R. Bacon, and G.B. Dalrymple. 1980. Late Cenozoic volcanism, geochronology, and structure of the Coso Range, Inyo County, California. *Journal of Geophysical Research* 85 (B5): 2,381–2,404.

Evans, J.R., and M. Smith, III. 1992. Teleseismic tomography of the Yucca Mountain Region: volcanism and tectonism. *Third Annual International High-Level Radioactive Waste Management Conference, Proceedings.* La Grange Park, IL: American Nuclear Society: 2,372–2,380.

Ho, C.-H., E.I. Smith, D.L. Feurbach, and T.R. Naumann. 1991. Eruptive probability calculation for the Yucca Mountain Site, USA: Statistical estimation of recurrence rates. *Bulletin of Volcanology* 54: 50–57.

Langenheim, V.E., K.S. Kirchoff-Stein, and H.W. Oliver. 1993. Geophysical investigations of buried volcanic centers near Yucca Mountain, Nevada. *Third Annual International High-Level Radioactive Waste Management Conference, Proceedings.* LaGrange Park, IL: American Nuclear Society. 1,840–1,846.

McDuffie, S.M., C.B. Connor, and K.D. Mahrer. 1994. A simple model for dike fracture interaction. *Eos, Transactions of the American Geophysical Union* 75: 345.

Nakamura, K. 1977. Volcanoes as possible indicators of tectonic stress orientation — principles and proposal. *Journal of Volcanology and Geothermal Research* 2: 1–6.

Oliver, H.W., E.L. Hardin, and P.H. Nelson. 1990. *Status of Data, Major Results, and Plans for Geophysical Activities, Yucca Mountain Project.* Springfield, VA: U.S. Department of Commerce: National Technical Information Service.

Parsons, T., and G.A. Thompson. 1991. The role of magma overpressure in suppressing earthquakes and topography: Worldwide examples. *Science* 253: 1,300–1,402.

Ponce, D.A., S.B. Kohrn, and S. Waddell. 1992. *Gravity and Magnetic Data of Fortymile Wash, Nevada Test Site, Nevada.* USGS Open-File Report 92-343. Reston, VA: U.S. Geological Survey.

Rout, D.J., J. Cassidy, C.A. Locke, and I.E.M. Smith. 1993. Geophysical evidence for temporal and structural relationships within monogenetic basaltic volcanoes of the Auckland volcanic field, northern New Zealand. *Journal of Volcanology and Geothermal Research* 57: 71–83.

Sanders, C.O., P. Ho-Liu, D. Rinn, and H. Kanamori. 1988. Anomalous shear wave attenuation in the shallow crust of the Coso volcanic region, California. *Journal of Geophysical Research* 85: 2,434–2,440.

Smith, E., D. Feuerbach, T. Naumann, and J. Faulds. 1990. The area of most recent volcanism near Yucca Mountain, Nevada: Implications for volcanic risk assessment. *Proceedings of the International Topical Meeting, High Level Radioactive Waste Management Volume I.* La Grange Park, IL: American Nuclear Society: 81–90.

Stirewalt, G.L., S.R. Young, and K.D. Mahrer. 1992. *A Review of Pertinent Literature on Volcanic-Magmatic and Tectonic History of the Basin and Range*. CNWRA 92-025. San Antonio, TX: Center for Nuclear Waste Regulatory Analyses.

Trapp, J.S., and P.S. Justus. 1992. Regulatory requirements to address issues related to volcanism and magmatism: Code of federal regulations, Title 10, Part 60, disposal of high-level radioactive wastes in geologic repositories. *Proceedings of the International Topical Meeting, High-Level Radioactive Waste Management Volume 2*. La Grange Park, IL: American Nuclear Society: 2,039–2,046.

Valentine, G.A., B.M. Crowe, and F.V. Perry. 1992. Physical processes and effects of magmatism in the Yucca Mountain region. *Proceedings of the International Topical Meeting, High-Level Radioactive Waste Management Volume 2*. La Grange Park, IL: American Nuclear Society: 2,344–2,355.

Valentine, G.A., K.R. Groves, C.W. Gable, F.V. Perry, and B.M. Crowe. 1993. Effects of magnetic processes on the potential Yucca Mountain repository: Field and computational studies. *Focus '93*. La Grange Park, IL: American Nuclear Society: 167–173.

Zoback, M.L., E.H. McKee, R.J. Blakely, and G.A. Thompson. 1994. The northern Nevada rift: Regional tectono-magmatic relations and middle Miocene stress direction. *Geological Society of America*. Bulletin 106: 371–382.

PART I: SEISMIC TOMOGRAPHIC METHODS

2 SEISMIC TOMOGRAPHY METHODS THEORY AND APPLICATION

2.1 DEFINITION OF TOMOGRAPHY

A tomograph is a cross-sectional image of some property of an object. The CAT scans used in medicine are tomographic images of the interior of human bodies. The property that is imaged in a CAT scan is the relative opaqueness of the various human tissues to x-ray propagation; that is, those tissues that absorb (attenuate) x-rays more readily will be distinguished from those tissues that allow x-rays to pass through with less energy loss. In the earth, the rock properties that are commonly imaged are the seismic wave velocity or seismic wave attenuation. Data from seismic waves with typical frequencies on the order of 1–10 Hz are used to make the images, in contrast to the much higher frequency x-rays used in medical tomography.

Seismic tomography involves the solution of multiple equations (derived from seismic data) for multiple unknowns (earth model). The equations are line integrals or discrete summations representing the propagation of seismic waves along particular raypaths in the earth from known sources to known receivers. For instance, the traveltime of a seismic wave is the integral of its slowness (inverse velocity) along the raypath (time = distance/velocity). The unknowns are the spatial distribution of rock properties in the volume traversed by the seismic waves. The solution to the problem is usually found with techniques of linear algebra whereby a matrix of the equations is inverted for the model matrix (the spatially varying seismic properties).

Seismic tomographic methods are enhanced by investigation of specific aspects of the seismic waveform, including the relative velocity of the compressional and shear waves, and attenuation of the waves. Laboratory studies (e.g., Ito, 1990) and field measurements (e.g., Sanders, 1993) indicate that partial melt, gas-rich zones, and alteration zones may be identified using seismic tomographic methods if several aspects of the waveform are included in the investigation. In the following, the most common methods for inverting seismic data for the seismic structure of the earth are described; these include both direct matrix inverse and approximate inverses using iterative algebraic algorithms.

2.2 BASIC SEISMOLOGICAL RELATIONS

2.2.1 Description of Seismic Wave Velocity and Attenuation

Although the medium through which seismic waves propagate is often described, for mathematical convenience, as a homogeneous, isotropic, elastic solid, the reality is that Earth is heterogeneous at many scales, is anisotropic in many regions, and is inelastic to some degree. The local departures from an ideal elastic solid are caused by the juxtaposition of different rock types due to geological processes, by the natural porosity and fracturing of the rock, by infiltration of aqueous or magmatic fluids or gases into permeable rock, by local geochemical or mechanical alteration of the rock, and by spatial variations in temperature. Thus, the elastic moduli that control the propagation of seismic waves are effectively average moduli within the volume of rock through which the wave propagates; this volume is related to the wavelength of the seismic wave. Because we seek to map 3D heterogeneity and anelasticity in tomographic studies of volcanic regions, we choose seismic waves with wavelengths generally the same size or smaller than the sizes of the heterogeneities. The recordings of these waves

hold information on the bulk elastic and inelastic properties of the rock within the wave propagation volume. A description of how the measurable seismic wave properties of velocity and attenuation are related to the various factors that give rise to spatial variations in elastic moduli and anelasticity of rocks is provided as follows.

Two basic types of seismic waves are generated by earthquake sources: P waves and S waves. Explosive sources usually generate only P waves, although with special design, S waves can be generated as well. P and S waves are also called body waves because they travel through the body of Earth. In contrast, surface waves, such as Love and Rayleigh waves, travel along Earth's surface, where they are formed from the interaction of P and S waves. Nearly all detailed tomographic studies of the crust and mantle in volcanic regions have used data from body waves because of the greater depth of penetration and resolution possible compared to the surface waves.

P waves are also called primary waves or compressional waves because they are the first to arrive at a seismograph station and because they propagate by compression and dilatation of the rock. The strain associated with P-wave propagation is purely volumetric. The velocity of propagation of P waves is described by

$$V_P = \sqrt{\frac{\kappa + \frac{4\mu}{3}}{\rho}} \tag{2-1}$$

Thus, the P-wave propagation velocity is dependent on the bulk modulus (incompressibility), κ, the shear modulus (rigidity), μ, and the density, ρ.

S waves are also called secondary waves or shear waves because on seismograms of local or regional earthquakes they are the second major phase to arrive and because they propagate as a shear strain through the rock. The strain associated with S-wave propagation is purely distortional. The velocity of propagation of S waves is described by

$$V_S = \sqrt{\frac{\mu}{\rho}} \tag{2-2}$$

Thus, the S-wave propagation velocity is dependent on the shear modulus and the density. The ratio of the P- and S-wave velocities is given by

$$\frac{V_P}{V_S} = \sqrt{\frac{\kappa}{\mu} + \frac{4}{3}} = \sqrt{\frac{(1-\nu)}{(0.5-\nu)}} \tag{2-3}$$

Thus, the V_P/V_S ratio is dependent on the ratio of the bulk and shear moduli or on Poisson's ratio. Because κ and μ are always positive and ν, Poisson's ratio, can have a value from 0.0 to 0.5, V_P/V_S is always greater than 1; that is, P waves always travel faster than S waves. As reference, we commonly assume that $\nu = 0.25$ (Poisson solid), in which case $V_P/V_S = 1.73$.

Seismic attenuation is defined as the loss of wave energy with time or distance traveled. Attenuation occurs because the rocks of Earth have some anelasticity. Due to defects in the rock matrix and rock mass, the cyclic transfer of kinetic to potential energy and back again associated with wave

propagation is not complete; some of the energy is converted to heat or is used to make permanent deformation. This attenuation of a wave with initial amplitude A_0 can be described by

$$A = A_0 \exp\left[\frac{(-\pi f l)}{(VQ)}\right] \tag{2-4}$$

where the value Q, the spatial attenuation factor, sometimes called the quality factor, controls the exponential decay of the amplitudes of waves with frequency, f. As the distance, l, that the wave has traveled at velocity, V, increases then wave amplitude, A, decreases exponentially according to the value of Q.

2.2.2 Traveltimes and Velocity

Seismic wave traveltimes are the data used to image the seismic velocity structure of a region. The traveltime of a seismic wave is the time required for the wave to travel from the source that generated the wave to the seismograph that records the wave. The traveltime can be considered as a line integral of the slowness (inverse velocity) along the raypath joining the source and receiver; the traveltime is described by

$$t_t = t_a - t_o = \int s \, dl \tag{2-5}$$

where t_o is the origin time, t_a is the arrival time, s is the slowness along some length element dl of the raypath, and the integral is along the raypath. In general, the relationship between traveltime and slowness is nonlinear, because the raypaths depend on the slowness distribution; however, for small slowness perturbations, and thus insignificant raypath deviations, an approximate linear relation can be derived (Aki et al., 1977; Fawcett and Clayton, 1984), which is written

$$\Delta t_t = \int \Delta s \, dl \tag{2-6}$$

The slowness perturbations, Δs, are the differences between the actual slowness and the assumed reference slowness. The traveltime residuals, Δt_t, are the difference between the observed traveltimes and those predicted by the reference slowness model. The problem is to use measured values of Δt_t to solve for the 3D distribution of Δs in the study volume. The problem can be discretized by dividing the study volume into a set of 3D blocks, where the slowness is assumed constant within each block. The discrete linear relation can be written as

$$\Delta t_r = \sum_b \Delta s_b \, l_{rb} \tag{2-7}$$

where the summation is over all blocks, b. Here Δt_r is the traveltime residual of the rth ray, Δs_b is the slowness perturbation in the bth block, and l_{rb} is the ray length of the rth ray in the bth block (Figure 2-1). If all of the traveltime residual is attributed to slowness perturbation in block b, a single raypath can be used to calculate the slowness perturbation because the length of the ray within the block is assumed to be known. To solve for two blocks with different slowness perturbations, at least two separate raypaths, each intersecting both blocks, are needed. Again, the geometry of the raypath is assumed to be known. The two raypaths may be traced from a single hypocenter, using two seismometers, or may be traced from waves from two separate hypocenters, measured at the same seismometer. Clearly, where there are many blocks and many raypaths, techniques in linear algebra must

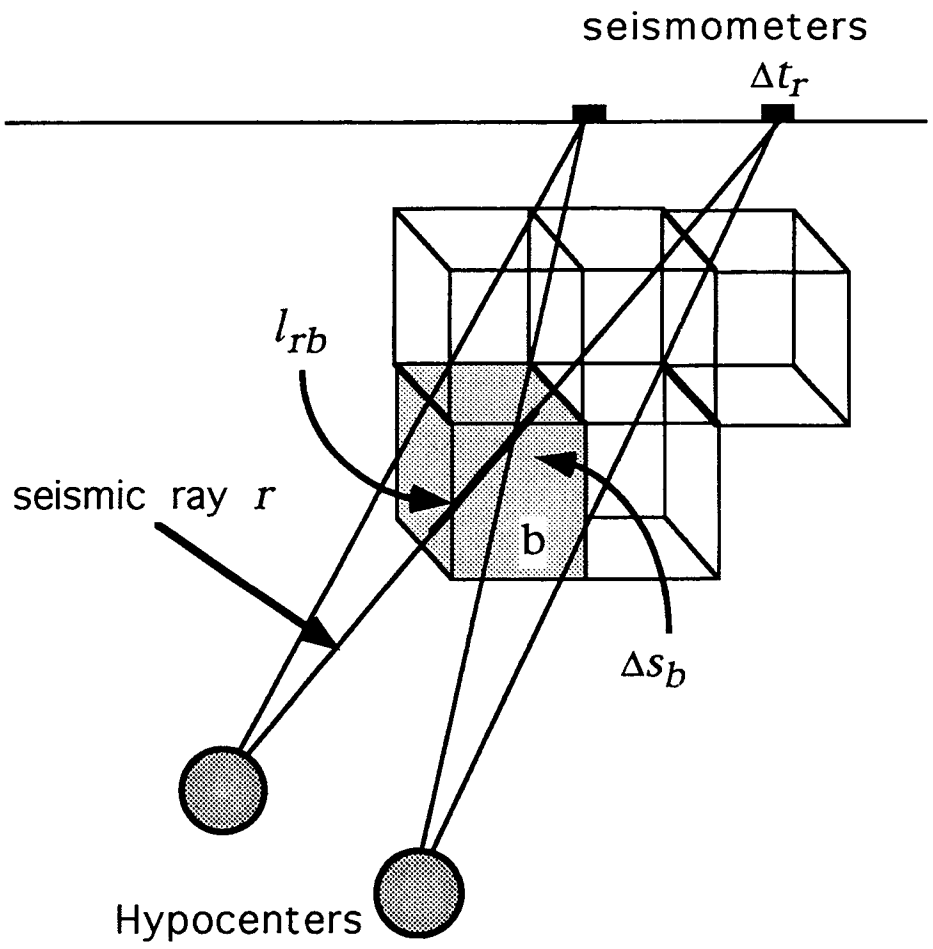

Figure 2-1. Schematic diagram illustrating the seismic tomographic method using Eq. (2-7). Multiple raypaths extend from earthquake hypocenters to seismometers. Block b has a slowness of Δs_b. Ray r has a length l_{rb} within block b, contributing to a traveltime residual, Δt_r, measured at the seismometer.

be used to solve Eq. (2-7). Because most raypaths may not intersect a given block, algebraic techniques for the inversion of large, sparse matrices are particularly important.

2.2.3 Amplitudes and Attenuation

In addition to slowness perturbation, seismic attenuation and phase amplitude can be used to infer 3D geologic structure. The basic data for studies of seismic attenuation structure are measurements of: (a) the Fourier amplitude spectra of phases on seismograms, (b) the amplitudes of phases on passband filtered seismograms, or (c) the pulse-widths of phases on seismograms. Most tomographic studies of crustal attenuation structure using local sources have utilized data of the form (a) or (b), and only these studies will be discussed in this review.

The amplitude spectrum A_r of seismic waves which traveled along ray r is related to the spectrum of the seismic waves that leave the source, A_0, and the modifications to this source spectrum by travel of the waves through the earth and the receiver. This is written as

$$A_r = A_0 \, I \, G \exp\left(-f \, \pi \, t_r^*\right) \tag{2-8}$$

with

$$t_r^* = \int \frac{dl}{V_i Q_i} \tag{2-9}$$

where l is distance along the raypath, f is frequency, I is the instrument response, G is geometric spreading, Q is the spatial attenuation factor, V is velocity, and the integral is along the raypath (e.g., Teng, 1968). The goal of most studies of seismic attenuation structure is to determine Q from measurements of A_r. In this relation, Q is an effective Q and includes the effects of intrinsic (inelastic) and apparent (scattering) attenuation.

In Eqs. (2-8) and (2-9) the principal unknowns besides Q are A_0, I, G, and the ray-path. Various analysis techniques have been developed to deal with these unknowns. The basic tactic is to either assume values or functional forms for the unknowns based on theory or observation, or to remove the unknowns from the problem by spectral division. For instance, Q is often assumed to be independent of f over some range of frequencies, A_0 is often assumed to be proportional to f^{-2} at high frequencies and to be independent of direction from the source, A_0 may be found from focal mechanism plots (Teng, 1968). Attenuation through small blocks caused by geometric spreading and $G \approx 1/r$ is assumed for body waves from local earthquakes. Also, I can be measured in the laboratory, and the raypath can be closely approximated by ray tracing through an experimentally determined P-wave velocity structure. The various techniques used to solve Eq. (2-8) for crustal attenuation structure and Eq. (2-7) for slowness perturbation using local sources or teleseisms and examples of applications of these techniques are discussed below.

2.3 INVERSION TECHNIQUES

2.3.1 Damped Least Squares for Teleseisms

The damped least squares inversion technique is commonly used in seismic tomography problems (e.g., Aki et al., 1977). For instance, the discretized traveltime perturbation relation Eq. (2-7) can be written in matrix form as

$$\mathbf{t} = \mathbf{L}\,\mathbf{s} \tag{2-10}$$

where **t** is the vector of traveltime residuals, **L** is the matrix of raypath lengths in individual blocks, and **s** is the vector of slowness perturbations. **s** has a length equal to the total number of blocks in the discretized study volume, therefore **G**, now a matrix of geometric spreading coefficients, has dimensions equal to the total number of traveltime residuals times the total number of blocks in the study volume. The damped least squares solution to Eq. (2-10) is

$$\mathbf{s}_{est} = (\mathbf{L}^T\mathbf{L} + \theta^2\mathbf{I})^{-1}\mathbf{L}^T\mathbf{t} \tag{2-11}$$

where $\mathbf{s}_{est}$ is the least-squares estimate of **s**, θ^2 is the damping parameter, and **I** is the identity matrix (Levenberg, 1944; Marquardt, 1963). The resolution matrix

$$\mathbf{R} = (\mathbf{L}^T\mathbf{L} + \theta^2\mathbf{I})^{-1}\mathbf{L}^T\mathbf{L} \tag{2-12}$$

measures how **s**, which represents the true slowness distribution, is smoothed into $\mathbf{s}_{est}$, the model slowness distribution. The covariance matrix relating the error in the solution to the error in the data is

$$\mathbf{C} = \sigma_d^2(\mathbf{L}^T\mathbf{L} + \theta^2\mathbf{I})^{-1}\mathbf{R} \tag{2-13}$$

where σ_d^2 is the variance of the data. The standard error of the solution is equal to the square root of the diagonal elements of **C**. The choice of θ^2 has the effect of removing eigenvalues smaller than θ^2, which promotes solution stability at the expense of resolution (Aki et al., 1977). The inverse is commonly found by singular-value decomposition.

2.3.2 Damped Least Squares for Local Earthquakes

When the earthquakes that are used as seismic wave sources are located in the study volume, then the problem of solving for the 3D velocity perturbation structure is coupled to the problem of locating the earthquakes. The earthquake locations depend on the *a priori* velocity model and the traveltime residuals used to solve for the new velocity perturbation model depend on the earthquake locations. To solve this problem a technique of parameter separation is used (Pavlis and Booker, 1980). Following Kissling (1988), the traveltime residuals are related to the model parameters (slowness perturbations in the model blocks plus earthquake hypocenters and origin times) by

$$\mathbf{t} = \mathbf{Ad} \tag{2-14}$$

where **t** is the vector of traveltime residuals, **A** is the matrix with partial derivatives of the traveltimes with respect to the model parameters, and **d** is the vector of hypocentral and slowness model parameter adjustments. **A** may be separated formally into two matrices

$$\mathbf{A} = \mathbf{H} + \mathbf{M} \tag{2-15}$$

where **H** is the matrix with partial derivatives of traveltime with respect to hypocentral parameters, and **M** is the matrix with partial derivatives of traveltime with respect to slowness model parameters. Thus, the coupled inverse problem can be separated into two inverse problems

$$\mathbf{Ad} = \mathbf{Hh} + \mathbf{Mm} \tag{2-16}$$

with **d** the vector of adjustments to all unknowns, **h** the vector of adjustments to hypocentral parameters, and **m** the vector of adjustments to slowness model parameters. This separation allows solving either problem separately without neglecting the other part of the coupled problem. The solution is usually accomplished with an iterative damped least squares technique. The implementation of this technique by Thurber (1983) is the most widely used in studies of volcanic regions.

2.3.3 Algebraic Reconstruction Techniques: Simultaneous Iterative Reconstruction Technique

Because the direct inversion of large matrices can be impractical due to computer memory and time limitations, other inverse techniques have been developed. These approximate inverse techniques were largely spurred by the development of CAT scan technology in the medical sciences, which required the relatively rapid inversion of thousands of x-ray intensity observations for detailed images of human body structure. There are several algorithms that have been developed to solve this problem; these include the Algebraic Reconstruction Technique (ART) (Herman et al., 1973) and the Simultaneous Iterative Reconstruction Technique (SIRT) (Gilbert, 1972; Dines and Lytle, 1979). A variant of the SIRT algorithm, which has been one of the most widely used tomographic techniques in seismological studies of earth structure, is discussed here.

A SIRT formula commonly used has been described in Walck and Clayton (1987; see also Humphreys and Clayton, 1988) based on a derivation by R. Comer and R. Clayton (unpublished manuscript, 1986). The formula for inverting traveltime residuals, Δt for slowness perturbations, Δs, is

residual
$$\Delta t_r^{(k)} = \Delta t_r^{(0)} - \sum_{rb} l_{rb} \Delta s_b^{(k)} \tag{2-17}$$

update
$$u_b = \frac{\sum_{rb} \left[\Delta t_r^{(k)} \frac{l_{rb}}{L_r} \right]}{\sum_{rb} (l_{rb} + \mu)} \tag{2-18}$$

result
$$\Delta s_b^{(k+1)} = \Delta s_b^{(k)} + u_b \tag{2-19}$$

where $\Delta t_r^{(0)}$ is the traveltime residual of the rth ray (these are the data), l_{rb} is the length of the rth ray in the bth block, L_r is the total length of the rth ray, μ is the damping parameter, $\Delta t_r^{(k)}$ is the remaining traveltime residual of rth ray through the updated slowness model after the kth iteration, and $\Delta s_b^{(k)}$ is the slowness perturbation in the bth block after the kth iteration. The damping parameter μ reduces the effect of poorly constrained parts of the solution (poorly hit blocks). In practice, a damping parameter with a value similar to the average of the sum of ray lengths through the model blocks gives satisfactory convergence. With multiple iterations, the SIRT solution approaches the least-squares solution (Ivansson, 1983).

2.3.4 Least-Squares Regression Techniques

The Least-Squares Regression (LSQR) algorithm (Paige and Saunders, 1982) is a technique for iteratively solving the least-squares problem using a conjugate gradients technique. The details of the algorithm will not be reviewed here, but are discussed in detail by Van der Sluis and van der Vorst (1987). Spakman and Nolet (1988) have compared LSQR, SIRT, and standard damped least squares and have found that LSQR is preferable to SIRT in situations when some model regions are poorly interrogated. LSQR puts less weight on the solution in the poorly resolved modeled regions. Also, LSQR converges to the solution more rapidly than SIRT.

2.4 APPLICATIONS

2.4.1 Velocity Structure

2.4.1.1 Teleseismic Source — ACH

The ACH inversion method of Aki, Christopherson, and Husseby (1977) is a damped least-squares method developed for teleseismic tomography. The explanation that follows is excerpted from Evans and Zucca (1988) and Achauer et al. (1988). This inversion relies on a linearization of the traveltime integral in the form of Eq. (2-6) and a discretization in the form of Eq. (2-7). The model volume is discretized by dividing it into horizontal layers with constant reference slowness (inverse velocities), and then subdividing each layer into a grid of rectangular blocks. Each block is assigned an independent parameter that describes the slowness fluctuation in the block from the layer reference slowness. In the top layer, each seismograph station is assigned a block, and the layer thickness includes the station's elevation. The source-station raypaths for any given source are assumed to be essentially identical between the source and the bottom of the model volume; therefore, all of the traveltime residual

differences are assumed to be due to the slowness structures along the divergent raypaths within the model volume. Raytracing through the model volume blocks is calculated through the one-dimensional (1D) reference slowness model; this assumes that any refraction due to 3D inhomogeneities is insignificant.

2.4.1.2 Local Source — Passive

Techniques for inverting arrival time data from local earthquakes to determine the local 3D velocity structure have taken primarily two forms. The form first developed was the simultaneous inversion for earthquake locations and velocity using the damped least-squares technique and parameter separation (e.g., Aki and Lee, 1976; Roecker, 1982; Thurber, 1983). Because the standard damped least-squares inverse is used in this technique the number of model parameters and data are limited. To overcome this limitation on model size and data quantity, techniques of a second form using SIRT or LSQR have been developed (e.g., Walck and Clayton, 1987; Lees and Crosson, 1989). In either of these techniques the earthquakes that are used as sources are also located within the study volume. In these techniques the earthquakes are located as accurately as possible using 1D velocity structures. These velocity structures are determined from seismic refraction surveys and sometimes from simultaneous inversions for 1D velocity structure, earthquake locations, and station corrections. The earthquake locations are then fixed and the inversion is only for the 3D velocity model parameters.

Both techniques have advantages and disadvantages. The advantage of the simultaneous inverse technique is that both earthquake locations and velocity structure are considered variables to be determined, which is appropriate. However, this technique suffers from the small number of velocity model parameters that can be determined by inversion, which in some cases limits the spatial resolution of the model. This can be a problem if the true heterogeneity in the study volume occurs on a smaller scale than the resolution of the model, as the velocity will be averaged over a large region, and the heterogeneity will not be imaged. Thus, for resolution on the order of 1 km, unless the total study volume is quite small, the SIRT or LSQR techniques must be used for simultaneous inversion of arrival times.

2.4.1.3 Local Source — NeHT

The NeHT technique for imaging shallow crustal structure uses a dense array to record crustal body-wave phases produced by earthquakes or large explosions at regional distances. The technique was first reported in the general scientific literature by Nercessian, Hirn, and Tarantola (1984) and therefore is commonly referred to by the acronym NeHT. The unique feature of the technique is the use of high-frequency crustal phases such an P_n or mid-crustal P_g to illuminate the shallow-crustal target volume from below with rays that are generally upward traveling throughout the target volume. The primary differences between this technique and the teleseismic (e.g., ACH) technique are two. Regional earthquakes or explosive sources are used rather than teleseismic earthquakes. This is an advantage if explosions are used because placement of the sources can be designed to achieve maximum azimuthal interrogation of the target volume. However, if explosion sources are used, the analysis is limited to compressional wave properties only. Another difference is the wave frequencies recorded are generally greater than 1 Hz, with peak frequencies on the order of 5 Hz, compared to wave frequencies of generally less than 1 Hz for waves recorded from teleseismic sources. This is due to the generally smaller sizes of the explosion and regional earthquake sources and to the lack of significant attenuation of the high-frequency waves along the relatively short travel paths. The use of these high-frequency waves allows maximum spatial resolution in the target volume on the order of 1 km or so, compared to maximum resolution in the crust of about 10 km for teleseismic studies. The NeHT and ACH techniques have similar overall geometry in that no sources or ray turning points occur in the model volume.

In the NeHT technique, a ring of explosive sources is deployed around a small dense array of seismographs located above the target volume. The explosive sources are located at distances from the seismograph array that will guarantee that the first arriving phases or later significant phases are upward traveling waves that have refracted, reflected, or turned in the mid-crust or at the Moho; in the three studies discussed later, this distance has been in the range of about 40 to 85 km. The spatial resolution within the target volume depends on two factors, the wavelengths of the waves recorded and the average distance between seismographs. The maximum resolution possible depends on the wavelengths of the waves recorded. For instance, if dominant frequencies are about 7 Hz and upper crustal velocities are about 6 km/s, then the dominant wavelengths and maximum resolution will be about 1 km. However, to obtain this maximum resolution the seismographs must have average separation distances equivalent to the dominant wavelengths. If the seismographs are separated by greater distances, then the effective spatial resolution will be similar to the average seismograph spacing. If the average seismograph spacing is less than the dominant wavelength, effective spatial resolution will not increase, though perhaps detection of structural gradients will be improved. The maximum depth of 3D resolution depends on the angle from the vertical that rays travel through the target volume. Assuming for reference incidence angles of about 45°, experience with the NeHT method indicates the maximum depth of resolution will be about 0.35 times the diameter of the array. Note that in this technique the crustal structure outside of the target volume traversed by the waves is assumed to be the same for all waves from a particular source and is removed from the problem. This results in the loss of information about absolute parameter values. Instead, relative parameter values are found in the target volume. The traveltime residuals can be inverted for the 3D velocity perturbation structure in the target volume using several different inversion algorithms.

2.4.2 V_P/V_S Structure

Several methods have been used to determine the V_P/V_S structure of the crust. The most apparent technique would be to invert P- and S-waves separately for the P- and S-wave velocity structures and then to simply divide the P-wave velocity by the S-wave velocity for particular locations. In practice, however, P-wave arrival times are picked by the regional seismic network operators much more commonly than S-wave arrival times. Also, P-wave arrival time picks are usually more accurate. Thus, in those studies that have attempted separate inversions for P- and S-wave velocity structure, the error in the S-wave structure prohibited meaningful estimation of the V_P/V_S ratio in much of the study volume. Other techniques that use the S- and P-wave arrival times from high-quality one- or three-component seismograms have been developed, and have proven to be effective in imaging the 3D V_P/V_S structure. These are reviewed below.

Walck (1988) developed a technique for imaging the 3D V_P/V_S structure in the crust using S- and P-wave arrival time data from local earthquakes. The details of the technique can be found in that paper. Just as P-wave traveltime residuals can be related to the slowness perturbation structure in the study volume by Eq. (2-3), the P- and S-wave arrival times can be related to V_P/V_S structure by

$$\Delta\left[t_S - \left[\frac{V_P}{V_S}\right]_0 t_P\right]_r = \sum_b (s_{0P} + \Delta s_P)_b \, \Delta \left[\frac{V_P}{V_S}\right]_b l_{rb} \qquad (2\text{-}20)$$

where r stands for ray, b stands for block, t_S is the S-wave traveltime, t_P is the P-wave traveltime, $(V_P/V_S)_0$ is the reference (average) value of V_P/V_S in the study volume, $(s_{0P} + \Delta s_P)_b$ is the P-wave slowness in block b determined from inversion of the P-wave traveltimes for 3D P-wave velocity structure, $\Delta(V_P/V_S)_b$ is the V_P/V_S perturbation in block b, and l_{rb} is the length of ray r in block b. Back projection of the left-hand side of Eq. (2-14) yields $(s_{0P} + \Delta s_P)_b \, \Delta \, (V_P/V_S)_b$. To obtain the values of $\Delta(V_P/V_S)_b$ it is necessary to divide out the $(s_{op} + \Delta s_{pb})$ determined from a separate inversion for P-wave velocity structure. Thus, even though two inversions are needed in this technique, the formulation specifically solves for V_P/V_S structure.

2.4.3 Attenuation Structure

2.4.3.1 Spectral Ratio or t* Technique — Teleseismic Source

This spectral ratio technique uses a reference spectrum to form the common denominator in all ratios. A reference spectrum is constructed for each source. The reference spectrum may be chosen as the spectrum for one receiver outside the study area or from the average of spectra for several receivers outside the study area whose seismograms are assumed to be minimally affected by the attenuation structure of the study volume. The reference spectrum may also be taken as the average spectra for all the receivers in the study area. Reference spectra constructed from averages have been found to be smoother (the influence of individual site responses is lessened) and to yield more stable results.

The technique as described by Solomon and Toksoz (1970, modified from Teng, 1968) is given here. Assume that the attenuation term in Eq. (2-8) is described by $\exp[-f\pi(t_r^* + \delta t_r^*)]$, where t_r^* given by Eq. (2-9) accounts for the regional homogeneous Q, and

$$\Delta t_r^* = \int \frac{dl}{V_r \, \Delta Q_b} \qquad (2\text{-}21)$$

where ΔQ is the deviation from the regional homogeneous Q along ray r (ΔQ assumed much larger than ΔV). Additionally, assume that $\Delta t_R^* = 0$, where R denotes the reference raypath. Calculate the Fourier spectrum of a window of the P or S phase on each seismogram which recorded the earthquake or explosion. Take the ratio of the spectrum of the signal at receiver i to the reference spectrum. This process cancels the frequency dependence of I if all instruments have the same response. The frequency dependence of the source A_0 cancels as well if the effect of source directivity is minimal. The resulting equation to be solved is

$$\ln\left[\frac{A_r}{A_R}\right] = \ln(a_{rR}) + \pi\left(t_R^* - t_r^* - \Delta t_r^*\right) f \qquad (2\text{-}22)$$

where a_{rR} contains the frequency-independent components of the source and propagation, and Q is assumed independent of frequency within the measured frequency band. Equation (2-22) is the equation

of a line with slope = $\pi\ (t_r^* - t_r^* - \Delta t_r^*)$. This slope can be determined from a least-squares fit to the plot of the logarithm of the spectral ratio versus frequency, and both t_R^* and t_r^* can be calculated from Eq. (2-9) with an assumed homogeneous regional Q. Thus, the differential attenuation Δt_r^* can be determined. The measurements of Δt_r^* are related to ΔQ structure by Eq. (2-21). If the study volume is divided into blocks of constant ΔQ and V then the relation is

$$\Delta t_r^* = \sum_b \left[\frac{l_{rb}}{V_b}\right] \left[\frac{1}{\Delta Q_b}\right] \tag{2-23}$$

where r is the ray number, and b is the block number for blocks traversed by ray r (Young and Ward, 1980). Equations (2-21) or (2-23) can be used to invert for ΔQ structure. The V_b are determined from the local crustal velocity structure, and the l_{rb} (the distance traveled by ray r in block b) are found by raytracing.

Studies using local sources and the spectral ratio technique described above have primarily relied on explosion sources and have investigated crustal P-wave attenuation structure. Use of explosive sources eliminates the directional dependence of the source radiation, thus simplifying the problem somewhat. However, with surface sources and receivers and typical velocity models the raypath location near the turning point may be poorly constrained, thus adding uncertainty to the problem.

2.4.3.2 Spectral Ratio or t* Technique — Local Source

In the traditional spectral ratio technique described above, a site correction is not made. The correction is not made because the attenuation in the upper 1 to 2 km of the crust affects only a fraction of a wavelength of the teleseismic waves used, and therefore the amplitudes of the waves are little changed. In local earthquake tomography, however, we utilize shorter wavelengths that are much more sensitive to the small-scale ($\sim$ 1 km) variations in the attenuation structure of the upper crust. These high frequencies necessitate the removal of site effects.

The site effect for a particular station can be removed from a spectrum by taking the spectral ratio of a body wave phase recorded at that station and the average spectra of that phase for all earthquakes recorded at the same station (Ponko and Sanders, 1994). The site effect terms will cancel because the site effect is near surface and all of the rays will be subjected to the same transfer function. Also the instrument effects are removed from the spectrum of interest because the instrument response terms are identical at the same station. Once the site and instrument responses have been removed, the spectrum of the source modified by the crustal response is left. However, if we choose to analyze the attenuation in a frequency range that lies below the source corner frequency (easy to do if earthquakes with $M<2$ are used), then there is no frequency dependency in the source term (directivity assumed insignificant) and it becomes a constant that will not effect the slope of the spectral ratio. With an assumed average value for the regional attenuation, Eqs. (2-22) and (2-23) can be solved for the differential attenuation.

2.4.3.3 S-to-P Ratio Technique

A technique for determining S-wave attenuation structure has been developed by Ho-Liu et al. (1988) [see also Ho-Liu (1988), Sanders et al. (1988), and (Ho-Liu et al. (1989)]. This technique was

developed to take advantage of the large quantity of vertical-component, narrow-band data that has been collected by regional seismic arrays. In this technique, S- and P-wave amplitudes (A_S and A_P) on passband filtered seismograms are measured, and the ratio A_S/A_P is calculated. The ratios from many seismograms are then inverted for the spatial distribution of the S-wave attenuation quality factor Q_S. This technique is effective for imaging relative attenuation structure. Because the formulation contains some constants whose values may be poorly known, absolute values of attenuation are less well constrained. The following derivation is from Ho-Liu et al. (1988).

The problem of solving for the spatial distribution of Q_S can be cast in a form similar to the problem of solving for the spatial distribution of seismic slowness perturbation Δs. If the study volume is divided into blocks, then the traveltime perturbation relation is as given by Eq. (2-7). For the attenuation problem the following equation is derived relating the A_S/A_P ratios to Q_S:

$$-\ln\left[\left[\frac{1}{k_1 k_2}\right]\left[\frac{A_{0P}}{A_{0S}}\right]\left[\frac{A_S}{A_P}\right]\right] = \sum_b \pi\, l_{rb}\, s_b \left[\frac{f}{Q_b}\right]\left[\frac{1 - s_p}{k_3 s_S}\right] \qquad (2\text{-}24)$$

where the value of (A_{0P}/A_{0S}), the ratio of the P-wave and S-wave amplitudes at the source, is found from focal mechanism plots and double-couple radiation relations. Equation (2-24) can be written

$$a_r = \sum_b m_{rb}\, q_b \qquad (2\text{-}25)$$

where $a_r = -\ln[(1/k_1 k_2)\ [A_{0P}(\theta,\phi)/(A_{0S}(\theta,\phi)](A_S/A_P)]$, $m_{rb} = \pi\, l_{rb} s_b$, *and* $q_b = (f/Q_b)(1 - s_p/k_3 s_S)$. Because Eq. (2-25) has the same form as Eq. (2-7), techniques used to invert for Δs_b can also be used to invert Eq. (2-25) for q_b.

Three constants in Eq. (2-24), k_1, k_2, and k_3, need to be evaluated. The most straightforward is $k_2 = (s_{0S}/s_{0P})^3$ in which the initial amplitudes of the S and P phases are related by the P- and S-wave slowness at the source. For normal crust, k_2 has a value near 5. The constant k_1 relates the response of a vertical-component seismometer to the incident P wave and S_V wave. If seismic velocities are low near the surface the incidence may be near vertical, in which case k_1 will be a small number, probably in the range 0.1–0.5. Without detailed velocity structure information beneath each seismograph, k_1 cannot be evaluated precisely. Ho-Liu et al. (1988) showed that though the magnitude of the resultant Q structure is somewhat sensitive to the value of k_1 used, the spatial geometry is not. Thus, the positions of anomalous structure can be imaged confidently. If three-component seismograms are available, then the traces may be rotated to obtain the maximum P- and S-wave amplitudes, in which case $k_1 = 1$ (Nixon, 1992). The constant k_3 is equal to the ratio of the average P- and S-wave Q in the crust. For normal crustal rocks $k_3 = 1$ to 2.3 (Ho-Liu et al., 1988). If attenuation is influenced by a fluid phase, then k_3 may exceed 2.3. The term $(1 - s_P/k_3 s_S)$ in Eq. (2-24) will have values of from 0.8 to 0.4, for k_3 from 2.3 to 1. As with k_1, the magnitude of the Q structure will be sensitive to the value of k_3 chosen, however the relative geometry of the structure will not. The inverted q_b need only be multiplied by $(1 - s_P/k_3 s_S)$ in order to include the effect of k_3 on the absolute values.

The SIRT formula for inverting Eq. (2-25) for q_b is

residual
$$a_r^{(k)} = a_r^{(0)} - \sum_b m_{rb}\, q_b^{(k)} \qquad (2\text{-}26)$$

update
$$u_b^{(k)} = \frac{\frac{\sum_r a_r^{(k)} m_{rb}}{L_r}}{\sum_r m_{rb} + \mu} \tag{2-27}$$

result
$$q_b^{(k+1)} = q_b^{(k)} + u_b^{(k)} \tag{2-28}$$

where $a_r^{(0)}$ is the data. If amplitude measurements at individual frequencies f are made, then the Q_b structure at each frequency can be determined.

2.5 INTERPRETATION OF SEISMIC RESULTS FOR GEOLOGICAL PROPERTIES

2.5.1 Factors Influencing Seismic Wave Velocity and Attenuation

The primary influences on seismic wave velocity and attenuation are the mineralogy of the rock, the abundance of pores and fractures in the rock, the presence of aqueous or magmatic fluids or gases in the pores and fractures, and the temperature. Here, the laboratory, theoretical, and field studies that bear on the relation of the seismic parameters V_P, V_S, V_P/V_S, Q_P, and Q_S to the rock properties are reviewed. Except where noted the wave frequencies used in the laboratory studies are usually in the sonic (kHz) or ultrasonic (MHz) range. Thus, it must be assumed that the relations observed are similar at seismic frequencies. Assume for reference an unfractured, nonporous, isotropic, elastic rock mass at ambient surface temperature and pressure. The affect of changing geologic conditions on seismic parameters is summarized in Table 2-1. However, specific conditions often complicate the relations shown in Table 2-1, and they are only intended as a general overview.

2.5.1.1 Dry Fractures and Pores

The introduction of voids (fractures, pores) filled with air into the rock mass causes the effective incompressibility, rigidity, and density to decrease. Though the effective density will be a volumetric average of the air and rock density, the effective incompressibility and rigidity will vary depending on the abundance, aspect ratios, and orientations of the voids. Because incompressibility and rigidity decrease more than density decreases, by Eqs. (2-1) and (2-2) both V_P and V_S decrease. In general, incompressibility is reduced more than rigidity, because even with the introduction of low-rigidity voids, the remaining interconnected rock framework keeps the bulk rigidity close to the original value. Thus, V_P is reduced more than V_S, and V_P/V_S decreases (O'Connell and Budiansky, 1974, 1977). Thin voids (fractures) have a much greater effect on the elastic moduli than rounded voids (pores) (Toksoz et al., 1976).

2.5.1.2 Aqueous Fluids

When aqueous fluids are introduced into the fractures and pores, the bulk incompressibility and density of the rock mass will increase, because the incompressibility and density of water are greater than that of the air that was replaced. The incompressibility increases more, however; therefore, V_P will

Table 2-1. Normal response of seismic parameters to increase the volume percent fractures or pores, saturation of rock with fluid or gas, pressure, and temperature

Parameter	Dry Fractures and Pores	Aqueous ‡ Fluids	Gas * (145 °C)	Pressure ¥	High Temperatures and Partial Melt
V_P	decrease	increase	decrease	increase	decrease
V_S	decrease	no change	increase	increase	decrease
V_P/V_S	decrease	increase	decrease	decrease	increase
Q_P	no change	decrease	no change	increase	decrease
Q_S	decrease	decrease	decrease	increase	decrease
Q_P/Q_S	increase	no change	increase	decrease	increase

‡ strongly dependent on saturation
* strongly dependent on gas temperature Q_P decreases at water-steam cotectic
¥ dependent on saturation and temperature

increase (Nur and Simmons, 1969; Toksoz et al., 1976). The bulk rigidity will not change significantly; therefore, V_S will not change and V_P/V_S will increase toward the value in unporous rock (O'Connell and Budiansky, 1974, 1977; Toksoz et al., 1976; Ito et al., 1979). If the abundance of fractures is increased in a fractured saturated rock, then V_P and V_S will decrease and V_P/V_S will increase (O'Connell and Budiansky, 1974, 1977; Moos and Zoback, 1983). Pearson et al. (1983) observed this at the Fenton Hill geothermal experiment where V_P/V_S between boreholes increased with time, probably due to cracking of the rock induced by cooling.

In porous sedimentary rocks at conditions similar to the shallow crust, as saturation increases Q_P and Q_S decrease, and Q_P/Q_S=0.66; however, above about 95 percent saturation, Q_P increases until at full saturation, Q_P/Q_S=2.5 (Winkler and Nur, 1979; Murphy, 1983; Burkhardt et al., 1986). Under saturated, subcritical conditions, seismic energy loss in compression may be negligible, and the relation $Q_P \approx 1.8 - 2.5\ Q_S$ may hold (Anderson et al., 1965). In partially saturated rocks, bulk compressional energy loss is about twice shear energy loss (Winkler and Nur, 1979). In fully saturated rocks, shear attenuation is much larger than compressional attenuation possibly due to fluid flow between cracks (O'Connell and Budiansky, 1977; Winkler and Nur, 1979). Small amounts of water distributed in thin cracks can significantly decrease Q (e.g., Mavko and Nur, 1979). However, the effect is strongly dependent on rock type; rocks with low surface areas (such as limestones) show negligible change in attenuation, indicating that adsorption of water in thin layers on free surfaces is the primary cause of this attenuation (Clark et al., 1980).

2.5.1.3 Gas

The results of Ito et al. (1979) and Winkler and Nur (1979) provide insight into the seismic velocity and attenuation in porous rocks (sandstone) that are dry (gas in pores), partially saturated (gas and fluid in pores), or fully saturated (fluid in pores). In both studies the results were obtained at a confining pressure of 300 bars, which is equivalent to a crustal depth of about 1 km. Ito et al. (1979) adjusted the pore pressure in hot, water-saturated rock so that the pore fluid changed continuously from water to steam through the water-steam transition. From measurements of wave velocity they found the following: at 19 °C (room temperature), both V_P and V_S remained constant during a pore pressure change of 10 bar; at 145 °C, V_P decreased 2–3 percent from water- to steam-saturated, with an additional 1-percent decrease in a narrow pressure range at the water-steam transition; at 198 °C, V_P increased less than 1 percent from water- to steam-saturated, with a 2-percent decrease in a narrow pressure range at the water-steam transition; at 145 °C and 198 °C, V_S increased by 3–4 percent from water- to steam-saturated, with no local anomaly at the water-steam transition. These velocity results can be summarized as changes in the V_P/V_S ratio V_P/V_S decreased by 4–6 percent from water- to steam-saturated rock. At constant pore pressure and with either water, steam, or water/steam in the pores, both V_P and V_S decreased with increasing temperature.

From measurements of wave amplitudes, Ito et al. (1979) found that at both 145 and 198 °C, S-wave amplitudes were 50 percent lower in water-saturated rock compared to steam-saturated rock. The change in amplitude occurred in a narrow band of pressures bounding the water-steam transition pressure. Thus, Q_S is lower in hot water-saturated rock than in steam-saturated rock. The P-wave amplitudes were more complicated. At 145 °C, P-wave amplitudes decreased by 50 percent at the water-steam transition, but were approximately equivalent when the pores were saturated with either all water or all steam. Thus, Q_P is anomalously low only at the water-steam transition when both water and steam are present. At 198 °C P-wave amplitudes were 20 percent lower through water- than through steam-saturated pores; the

decrease occurred at the water-steam transition, but no local minimum was present. Winkler and Nur (1979) found that in dry rocks Q_P is larger than Q_S, in saturated rocks Q_P is much larger than Q_S, and in partially saturated rocks Q_P is smaller than Q_S. In summary, these two studies show that Q_P is lowest when the ratio of bulk incompressibility to bulk density is lowest; this occurs during partial saturation or when a small percent of gas is mixed with fluid in the pores. Q_S is lowest in either dry rocks or fully saturated rocks.

2.5.1.4 Pressure

Increasing the pressure is analogous to increasing the depth beneath the surface. Increasing pressure has the effect of closing fractures and pores and expelling the gas or fluid contained within them. With increasing pressure both V_P and V_S increase (Nur and Simmons, 1969; Toksoz et al., 1976) and Q_P and Q_S increase (Winkler and Nur, 1979; Jones and Nur, 1983). V_P/V_S decreases with depth in the upper few kilometers of the crust (Moos and Zoback, 1983; Nicholson and Simpson, 1985).

2.5.1.5 Temperature and Partial Melt

Studies of wave velocity and attenuation in metal alloys that are heated through the melting temperature at a set pressure (solidus) have revealed the following. Mizutani and Kanamori (1964) found that prior to melting, V_S decreased about 9 percent and V_P decreased 2 percent. Thus, V_S decreased four times faster than V_P as temperature increased to near the solidus, implying that V_P/V_S increases as temperature increases below the solidus. The V_S drop through the solidus was 100 percent, while the V_P drop was about 20 percent; thus V_P/V_S increases significantly after melting occurs. About 90 percent of the decrease in V_S and V_P occurred in a narrow temperature range around the solidus. They also found that Q_P is about 90 percent lower in liquid compared to solid alloy. Stocker and Gordon (1975) found that the V_P decrease rate as melt fraction increased in a partially molten alloy depended on the dihedral angle of the alloy; the smaller the angle, the more rapid the V_P decrease. From a plot of data from several studies of partially molten alloys, a relation between percent V_P decrease and percent partial melt emerged. For example, a 7-percent V_P decrease may be due to 4-percent partial melt if the dihedral angle is 60° (melt distributed in tubes at grain boundaries) and 0.005 percent partial melt if the angle is 0° (melt distributed as film between grain faces).

The only study of S-wave velocity and attenuation in volcanic rocks at high temperature (but room pressure) is that of Kampfmann and Berckhemer (1985). In their laboratory experiments they used waves with frequencies in the seismic band. They found that for the basaltic rocks they studied, in general, Q_S decreased with temperature by two orders of magnitude (from about 1,000 to less than 10) in the temperature range 600 to 1100 °C. The decrease of Q_S with temperature was not linear, however, except in the temperature range of about 700 to 900 °C, where the following relation holds for waves with frequencies between 0.1 and 10 Hz,

$$\text{Temperature} = 100 - 150 \log Q_S \ (\pm 50\ ^\circ C) \qquad (2\text{-}29)$$

From about 900 to 1000 °C, Q_S was relatively constant; and at temperatures greater than the solidus temperature of about 1000 °C, Q_S again decreased with increasing temperature at a rate similar to that in the 700 to 900 °C temperature range. These data indicate that high attenuation does not require partial melting; in fact, most of the two-decade decrease in Q_S occurred at subsolidus temperatures. From measurements of the rigidity and electrical resistivity Kampfmann and Berckhemer (1985) found that "the

influence of the melt phase on anelasticity is by far smaller than on elastic and electrical properties." That is, though V_S decreased with increasing temperature below the solidus, the decrease rate increased substantially once melting occurred; however, the rate of decrease of Q_S was primarily related to temperature and was influenced little by the onset of melting. Murase and McBirney (1973) measured P- and S-wave velocity and attenuation in basaltic, andesitic, and rhyolitic rocks and glasses at room pressure and increasing temperatures through the solidus. They found that V_P decreased by about 50 percent from the solid to the molten state. In the temperature range 0 to 1500 °C Q_P decreased continuously from about 3,000 to less than 10, with no extra decrease at the solidus. S-wave amplitudes decreased dramatically at temperatures above the solidus.

Sato and Sacks (1989) and Sato et al. (1989) report on the effect of temperature on P-wave attenuation and velocity at frequencies of 60–880 kHz in dry peridotite at pressures from 0.20–1.0 GPa (70–350 km depth) and temperatures from 950 to 1280 °C. They found that V_P decreased about 2 percent per 100 °C below the solidus; however, there was a sudden rapid decrease by up to several tens of percent once the solidus was exceeded and the melt fraction exceeded a couple of percent. They also found that Q_P decreased by a factor of six linearly and smoothly through the solidus. This is similar to the amount of decrease in Q_S found by Kampfmann and Berckhemer (1985) in peridotite in this same temperature range but room pressure.

Sato and Manghnani (1985) measured V_P and Q_P in mafic melts at temperatures from 1100 to 1400 °C, at room pressure, and with wave frequencies around 1 MHz. They found that both V_P and Q_P decreased as temperature increased in the melts. The dependence of V_P and Q_P on frequency was weak at the higher temperatures and strong at the lower temperatures.

When melt is distributed as thin films or tubes at grain boundaries, localized fluid flow processes may dominate attenuation of seismic waves (e.g., O'Connell and Budiansky, 1977; Mavko, 1980). Under these conditions, the rigidity will drop considerably while the incompressibility will drop only slightly (Walsh, 1969), leading to a larger decrease in Q_S than in Q_P.

2.5.1.6 Hydration

Hydration affects a rock's seismic properties. Ito's (1990) measurements of seismic velocities of hydrous peridotites at mantle conditions (1 GPa pressure) indicate that seismic velocities decrease 5–25 percent upon hydration of the rock; the decrease totals 21–44 percent when the fluid phase is released upon dehydration at temperatures greater than 600 to 800 °C. Though this experiment was with ultramafic rocks at upper mantle conditions, it suggests that low-velocity zones in active volcanic and geothermal regions could be related to the presence of hydrated (altered) crustal rock or free water rather than partial melt. In addition, Umino and Hasegawa (1984) studied Q_S in the Japan subduction zone and found that the mantle region where hydrous minerals and perhaps a free fluid phase should be located is a region of relatively normal S-wave attenuation.

2.5.2 Possible Geological Conditions

Measurements of the seismic-wave attenuation and velocity properties of the rocks provide evidence about the 3D elastic and inelastic nature of the crust and mantle. Below a few kilometers depth, besides the probably typical fractured crystalline rock, there may be zones of partial melt with various melt percentages, accumulations of magma of various shapes and sizes and with various percentages of

crystals, zones with high but subsolidus temperatures and possibly viscous rheology, zones with subcritical or supercritical hydrothermal fluids in fractures, zones of hydrothermal alteration (hydrated minerals), or various combinations of these. Each of these local crustal conditions has its own effect on the seismic wave propagation.

The laboratory results suggest that by measuring the seismic attenuation and velocity properties in the crust and mantle of active volcanic regions we can distinguish among normal crustal rock, zones of magma or partial melt, and zones of supercritical hydrothermal fluids. Low Q, especially low Q_S, and high V_P/V_S values suggest the existence of high temperatures and perhaps partial melt. Low Q_P/Q_S and low V_P/V_S suggest supercritical hydrothermal fluids.

3 TOMOGRAPHIC STUDIES OF REGIONS WITH ACTIVE VOLCANISM

Tomographic studies of regions with volcanic or geothermal activity are reviewed below. General review papers include Iyer (1984, 1988). Reviews are subdivided based on dominant geochemical type into investigations of silicic, andesitic, and basaltic centers, complexes, and volcanic fields. Some of these volcanic centers and fields are bimodal, such as the Coso volcanic field and the San Francisco peaks area within the San Francisco volcanic field. Consideration of a broad range of geochemical types is necessary because seismic tomographic methods have been used to investigate the potential for continuing silicic volcanism in the YMR, as well as the basaltic volcanism (Evans and Smith, 1992). Review of other areas, such as the Milos Island geothermal field, Greece, is worthwhile because of the detail of these investigations, and the possibility of applying similar methods to problems in basaltic volcanism in the YMR or elsewhere in the western Great Basin.

3.1 SILICIC VOLCANOES

3.1.1 Yellowstone, Wyoming

The 3D P-wave velocity structure of the crust and upper mantle beneath Yellowstone caldera has been imaged by Iyer et al. (1981). They used 1,382 P-wave residuals from 221 teleseismic earthquakes recorded at 50 seismograph stations to image the velocity structure in a 200-km diameter by 200-km deep study volume. The ACH inversion technique was used, and the spatial resolution was about 10 km. The results of this study were quite significant. Reduced P-wave velocities were imaged in both the crust and mantle. P-wave velocities beneath the caldera were reduced by 15–20 percent in the upper crust, by 5–10 percent in the lower crust, and by 2–8 percent in the upper mantle. The diameter of the anomalous region averaged about 40 km. The authors interpreted this large zone of low P-wave velocities as a zone of partial melting in the crust and upper mantle beneath Yellowstone.

The 3D P-wave velocity structure of the upper 16 km of the crust beneath Yellowstone was studied by Benz and Smith (1984). They used P-wave arrival times from 30 selected local earthquakes at 16 local stations and 6 local explosions. A technique for simultaneously inverting for velocity structure and earthquake locations was used. This technique was similar to Thurber's (1983) except that the study volume was discretized into blocks instead of nodes, and a different 3-D ray tracer was used. The study was discretized into blocks with dimensions of 21×18 km in two layers with thicknesses of 2 and 14 km. The results agree well with gravity data and indicate two low-velocity regions in the second layer, one in the northeast corner of the caldera that coincides with a gravity low and the largest area of hydrothermal activity in Yellowstone, and one in the southwest corner of the caldera that coincides with the Old Faithful area.

The 3D P-wave velocity structure of the upper 20 km of the crust beneath Yellowstone caldera was investigated by Kissling (1988). He used arrival times from 3,500 selected local earthquakes and explosions recorded at subsets of the 40 permanent and over 200 temporary stations deployed in the area between 1973 and 1985. An approximate ACH technique for simultaneously inverting for 3D velocity structure and hypocenters was employed. The primary result is the image of low velocities directly beneath the caldera in the depth range of 7–14 km.

The 3D P-wave attenuation structure of the upper 12 km of the Yellowstone caldera crust was investigated by Clawson et al. (1989). They measured spectra of P waves from 6 explosions recorded on 90 stations. The spectra from 2 to 16 Hz were measured from 0.5 s windows using the maximum entropy method. The reduced-spectral-ratio ($t*$) technique was used to determine the differential attenuation. The reference spectrum was the average of the spectra at three stations located on bedrock sites at the periphery of the study volume. The 70×150 km study volume was discretized into a surface layer from 0 to 2 km depth and an upper crustal layer from 2 to 12 km depth and blocks with horizontal dimensions of 14×15 km. A weighted least squares algorithm was used to invert the spectral ratios for differential attenuation. The results show relatively high attenuation in the upper layer probably related to unconsolidated sediments, fracturing, and possibly a steam hydrothermal system. In the 2 to 12-km layer attenuation was generally lower except for two regions of high attenuation, one associated with an area of thick sediment, and the other associated with a region of intense hydrothermal activity, low gravity, and 20-percent reduced P-wave velocities. The latter region was interpreted as a region of steam-rich hydrothermal system or partial melt. Chatterjee et al. (1985) found 9–14 percent low V_P/V_S in the geothermally active caldera at Yellowstone.

3.1.2 Long Valley Caldera and Mono Craters, California

The 3D seismic structure of the crust and upper mantle beneath Long Valley Caldera, California, has been tomographically imaged by several groups using several different techniques. Long Valley has been the site of bimodal volcanism for several million years, however the major and most important volcanism has been rhyolitic. Long Valley may be the most extensively studied volcanic area in the world, with both geological and geophysical studies. The tomographic studies are reviewed below.

The 3D P-wave velocity structure of the crust and upper mantle beneath the Long Valley Mono region has been investigated by Steeples and Iyer (1976), Achauer et al. (1986), and Dawson et al. (1990). The study by Dawson et al. (1990) provides the most recent results and so will be discussed here. All three studies have consistent results. Dawson et al. (1990) used P-wave travel time residuals from teleseismic earthquakes recorded on local seismographs and an ACH inversion to determine the velocity structure. The 90-station seismic array formed a 75×45-km array centered on Long Valley and including the Mono Craters north of Long Valley. The average station spacing was about 5 km, and the average wavelength of the 1-Hz waves recorded was about 6 km. The 1–2 Hz seismograph stations were from the permanent local network and from temporary deployments during two summers. The seismograms were recorded in analog format, and later were digitized at 100 samples/s. The relative P-wave arrival times were measured at a distinct peak or trough in the first wave cycle using a phase correlation technique with an estimated accuracy of about 0.05 s. Over 3,200 usable arrival times were provided by 180 earthquakes. The absolute travel time residuals were calculated from the difference between the theoretical travel time (Herrin, 1968) and the observed travel time. The relative travel time residual was calculated by subtracting the weighted mean residual for each earthquake from the absolute residuals of every station for that earthquake. The relative travel time residuals contain information on the velocity structure beneath the array to a depth about equal to the diameter of the array, in this case about 60 km.

The relative travel time residuals were inverted for 3D P-wave velocity structure using the ACH inversion technique. The study volume was discretized into two different block models: a shallower model which extended to 32 km depth had blocks with a depth dimension of about 5 km and horizontal dimensions of about 3 km; a deeper model which extended to about 62 km had blocks with a depth dimension of about 8 km and horizontal dimensions of about 6 km. Spatial resolution is estimated at about

5–6 km. The resulting velocity-perturbation images are relative to the starting 1D velocity model determined from seismic refraction studies of the region. Two mid-crustal low-velocity bodies are found. The first body is centered between 7 and 20 km depth beneath the resurgent dome of Long Valley and has a volume of 150–600 km^3. The second, with a similar volume, is centered between 10 and 20 km depth beneath the Mono Craters. The Mono anomaly was also imaged in an earlier study using only part of the data set by Achauer et al. (1986). Velocity contrasts between both of these bodies and the surrounding rock are about 6–10 percent. These bodies are interpreted as silicic magma chambers.

The 3D S-wave attenuation structure of the upper 10 km of the crust beneath Long Valley caldera was studied by Sanders (1984; 1993) and Nixon (1992). In Sanders (1993), the S-to-P amplitude ratio technique was used. A total of 1,063 qualitative amplitude ratios from vertical-component seismograms of 248 local earthquakes were used. The amplitude ratios were inverted for S-wave attenuation structure with a SIRT algorithm. The study volume had dimensions of $54 \times 56 \times 15$ km and was discretized into square blocks 1 km on a side. The results indicate a region of anomalously high S-wave attenuation located beneath the resurgent dome at depth of 7 to at least 9 km.

In Nixon (1992), the S-to-P amplitude technique was also used to study the S-wave attenuation structure in the upper 8 km of the Long Valley caldera crust. They used amplitude ratios from 222 three-component and 264 vertical-component seismograms and a SIRT algorithm to invert for attenuation structure. The data were collected during a 6-month U.S. Geological Survey (USGS) field experiment in 1984. This was the same experiment where the data for Dawson et al. (1990) were collected, except whereas they used the teleseismic seismograms, local earthquake seismograms were used. The study volume had dimensions of $54 \times 48 \times 15$ km and was discretized into square blocks with 1-km sides. The primary result is the image of a region of high S-wave attenuation in the 7–8 km depth range beneath the resurgent dome. This gives further support to the results of Sanders (1984; 1993).

The 3D V_P/V_S structure of the upper 8 km of the Long Valley caldera crust was studied by Schwartz (1993). She used 502 high-quality S-minus-P times from 105 local earthquakes recorded during the 1984 USGS experiment. The P-wave arrivals were picked from the vertical-component records, and the S-wave arrivals were picked from the horizontal-component records. In addition, 2,852 P-wave arrival times from the temporary and permanent stations described above were used to invert for the gross 3D V_P structure using the technique of Thurber (1983). This V_P structure and the S-P data were used with the technique of Walck (1988) to invert for the 3D V_P/V_S structure. The results of this study indicate a region of high V_P/V_S beneath the resurgent dome in the 8–9 km depth range, low V_P/V_S in the 6–7 km depth range beneath the resurgent dome, and low V_P/V_S in the 4–5 km depth range beneath Mammoth Mountain. In conjunction with the results of Sanders (1993), Nixon (1992), and Ponko and Sanders (1994), these results are interpreted as indicating a zone of very high subsolidus temperatures or magma accumulation beneath depths of 7 km beneath the resurgent dome. Above this zone and at 4–5 km beneath Mammoth Mountain are possible gas-rich hydrothermal regions.

The 3D P- and S-wave attenuation structure of the upper 10 km of the crust beneath Long Valley caldera was investigated by Ponko and Sanders (1994). A form of the spectral ratio ($t*$) technique and the LSQR algorithm were used to tomographically invert for the attenuation structure. Seismograms of about 100 local earthquakes recorded at 21 three-component local stations were analyzed. The seismograms were selected to have a signal-to-noise ratio of at least four. The spectra of 0.5 s windows of the P- and S-waves were calculated. The final data set consisted of 378 P-wave spectra and 295 S-wave

spectra. Unlike the traditional reduced-spectral-ratio technique where the reference spectrum is usually the average of all spectra from one earthquake, in this study where local earthquakes are used and thus wavelengths are short and the site effect is significant, the most appropriate reference spectrum is the average of all earthquake spectra at each station. Thus, the spectral ratio consists of the spectrum of a wave at a particular station divided by the average spectrum recorded at that station. This effectively cancels the site effect, though it does not cancel the source as is done in the traditional spectral-ratio technique. However, the source contribution to the spectra can be considered to be similar for each earthquake, because the spectra are taken in frequency bands that are below the corner frequency for these small earthquakes. The study volume was centered on Long Valley caldera and had dimensions of $48 \times 54 \times 18$ km. The rays were traced through the 1D P-wave velocity model determined for Long Valley from seismic refraction studies and inversions for 1D velocity structure. The study volume was discretized into blocks 1 km on a side, and the inversion was for the value of differential attenuation in each block. The reference value of Q was 800 for the frequency range of 11–20 Hz. The final results indicate zones of high P-wave attenuation at 4–5 km depth beneath the east flank of Mammoth Mountain and at 6–8 km beneath the resurgent dome. Also, a zone of high S-wave attenuation was imaged at 7–8 km beneath the resurgent dome. The P-wave attenuation anomalies are interpreted as geothermal fluid zones with compressible, possibly gas-rich fluids. The S-wave attenuation anomaly was interpreted as a very hot or partially molten zone.

3.1.3 Coso Volcanic Field and Geothermal Area, California

The Coso volcanic field is bimodal characterized by a central Pleistocene rhyolite field that is flanked by basalt flows (e.g., Bacon et al., 1980; Duffield et al., 1980). Several seismic tomography studies of the crustal structure have been carried out in the Coso area.

The P-wave velocity structure of the upper 22 km of the crust beneath Coso was studied by Reasenberg et al. (1980). They used P-wave arrival times of rays from 137 teleseismic earthquakes. The relative arrival times at approximately 40 stations were picked using a phase correlation technique, and the traveltime residuals were calculated relative to the Herrin (1968) velocity model. The traveltime residuals were inverted using the ACH technique. The study volume was centered on the Coso Range and was discretized into three layers of blocks with dimensions of $5 \times 5 \times 7.5$ km. Spatial resolution was on the order of the average station spacing which was about 4–5 km. The results indicate a low-velocity volume directly beneath the rhyolite domes near Devil's Kitchen in the second and third model layers (about 5–20 km deep) that has lateral dimensions on the order of one block size (5 km). The maximum velocity contrast is in the range 6–8 percent.

The 3D P-wave attenuation structure of the upper 20 km of the crust beneath Coso was investigated by Young and Ward (1980). Spectra of 5-s windows of the P waveform were calculated for 53 teleseismic earthquakes recorded at 32 stations. The spectral ratio ($t*$) technique and a linear generalized inversion (similar to ACH) were used to invert the spectral amplitude data for attenuation structure. The study volume was discretized into blocks 5 km on a side in three layers from 0 to 5, 5 to 12, and 12 to 20-km depth. A shallow zone of high attenuation in the upper 5 km beneath the main region of high heat flow is interpreted as a shallow vapor-liquid zone associated with the geothermal system or some other highly attenuating surface lithology. Between 5 and 12 km, no zones of abnormal attenuation were imaged. High attenuation was imaged in the 12–20-km depth layer, which is interpreted to contain the heat source for the shallow geothermal system.

The 3D P-wave velocity of the upper crust in the Coso region was studied by Walck and Clayton (1987). They used 4,036 P-wave traveltime residuals from 429 local earthquakes and a SIRT algorithm to invert for velocity variations in the upper 10 km of the crust. The traveltime residuals were calculated relative to the Coso-specific 1D velocity structure that was determined previously from seismic refraction studies. The earthquakes had been recorded at stations of the regional southern California seismic array and located using routine arrival time data picks. The 429 earthquakes used in the study were selected to be well-located and to provide good azimuthal and depth interrogation of the study volume. Most of the earthquakes used lie shallower than 8 km, though a few are located as deep as 15 km. The model volume had dimensions of $70 \times 80 \times 10$ km, and was divided into 11,200 blocks with dimensions of $2 \times 2 \times 2$ km. The primary result of the inversion was the image of a region of relatively low P-wave velocities (as much as 7 percent slower) in the 3–5 km depth range beneath an alluvial valley south of the Coso volcanic area. Significantly, the velocities in the upper 10 km of the crust directly beneath the Coso volcanic area was relatively normal. These results suggest that no accumulation of magma larger than about 2 km in diameter exists in the upper crust beneath Coso; however, a significant body of magma may exist in the shallow crust about 30 km south of Coso.

The 3D V_P/V_S structure of the upper crust in the Coso region was studied by Walck (1988). She used 2,966 P-S traveltime pairs from 976 local earthquakes recorded by up to 37 local stations. The earthquakes were relocated using a Coso specific 1D velocity model and close-in stations. The average V_P/V_S value for the crust in the region was determined from a modified Wadati diagram to be 1.71. The S- and P-wave travel times were inverted for the V_P/V_S perturbation structure using the technique described above. The study volume was discretized into 5×5-km wide blocks in five depth layers (0–2, 2–5, 5–10, 10–15, and 15–20 km). The results indicate that in the 0–2 km layer low values of V_P/V_S correlate with the Coso geothermal field, suggesting a steam-dominated field. Also, in the 2–5 and 5–10 km layers, high V_P/V_S is seen beneath Indian Wells Valley in locations similar to those where high S-wave attenuation was imaged by Ho-Liu et al. (1988) and Sanders et al. (1988). This gives further support to interpretations of partial melt.

The 3D S-wave attenuation structure of the upper crust in the Coso region was studied by Sanders et al. (1988) and Ho-Liu et al. (1988). For these studies, 329 vertical-component seismograms of 16 well-located and well-distributed local earthquakes were analyzed for the S- and P-wave amplitudes. The S-to-P amplitude ratio technique (Ho-Liu, 1988) was used to tomographically invert the amplitudes for 3D S-wave attenuation structure. Rays were traced through the same 1D P-wave velocity model used by Walck and Clayton. Spatial resolution is on the order of 2–5 km. The primary result of these studies was the image of a very attenuating region in the 3–7 km depth range with overall dimensions of about 30×30 km. This attenuating region does not lie beneath the Coso volcanic field, however, it lies about 30–50 km south beneath a deep alluvial valley near the eastern frontal fault of the Sierra Nevada range. This is the same general location as the low-P-wave anomaly of Walck and Clayton. Attenuation in the upper 10 km of crust beneath the Coso volcanic field is relatively normal, suggesting no magma accumulation larger than a couple of kilometers in diameter.

3.1.4 Valles Caldera, New Mexico

The P-wave velocity structure of the Valles caldera was investigated by Roberts et al. (1991). Three-component, 1-Hz seismographs were deployed in two, NW-SE oriented, linear arrays; one array had a 32 km aperture with spacing between stations of about 5 km, and the other array had a 14-km

aperture with station spacing of about 2 km. P-wave arrival times from 24 teleseisms which had azimuths within 20° of the array azimuth (Alaska, Japan, South America earthquakes) were used to forward model the general crustal velocity structure beneath the array. For each source travel-time delays were calculated at all of the stations relative to a station near the caldera rim. Forward modeling of these delays resulted in 2D model of the P-wave velocity structure. The primary feature in the final model is a lens-shaped low-velocity zone about 17 km wide, centered at about 10–13 km depth, and greater than about 8 km thick. The velocities in the anomalous zone are reduced by about 30 percent relative to the surrounding rock, which suggests that the zone may contain partial melt.

3.1.5 Roosevelt Hot Springs, Utah

The 3D P-wave velocity structure of the Roosevelt Hot Springs was investigated by Robinson and Iyer (1981). They used P-wave arrival times of teleseismic earthquakes recorded on a closely-spaced, 2D array of 15 seismographs. The inversion technique was similar to the ACH technique. From 5–35 km directly beneath the geothermal area a low-velocity volume was imaged, with a maximum velocity contrast of about 7 percent.

3.2 ANDESITIC VOLCANOES

3.2.1 Mont Dore, France

The NeHT technique has been used in three studies. The technique was first used by Nercessian et al. (1984) in their study of the 3D P-wave velocity structure of Mont Dore volcano, France. They detonated five 1-ton borehole explosions at distances of about 80 km from the volcano and at five widely varying azimuths and recorded the critical Moho (28 km deep) reflected phase PMP at 96 seismographs in a 20×20 km array. The maximum frequencies recorded were about 15 Hz, and the average station spacing was about 2 km, so the spatial resolution of the image of P-wave velocity structure beneath the volcano was about 2 km. The rays traveled through the target volume at angles of about 45°, so the region of crossing rays and thus of 3D resolution extended to about 7 km depth. For each explosion the relative arrival times at the different stations of the PMP phases, which were not the first arriving phases, were measured by first correlating the phases among the seismograms in the 2–8 Hz passband and then picking the first zero crossing on seismograms filtered with 4–16 Hz passband. The authors estimate the relative time-picking accuracy at 0.01 s. They inverted the traveltime deviations for P-wave velocity perturbations using the no-block inversion technique of Tarantola and Nercessian (1984). They found two zones with significant low P-wave velocities. One zone is located directly beneath the summit caldera at depths above 1 km and is interpreted as an accumulation of sediments in the structural depression associated with the caldera, and the other zone is located at depths of 2–5 km and is interpreted as perhaps the remnants of a small magma chamber with dimensions on the order of 2–3 km.

3.2.2 Newberry Caldera, Oregon

The NeHT technique was used by Achauer et al. (1988) in a study of the 3D P-wave velocity structure of Newberry volcano, Oregon. In this study, nine borehole chemical explosions were used, six at about 39 km distance and three at about 85 km distance from the seismograph array. The seismic waves generated by the explosions were recorded on 120, 2-Hz seismographs deployed in a 13-km-diameter array above the summit caldera of the volcano. The average seismograph spacing was 1.1 km, and the dominant wave frequency was about 7 Hz, so the estimated spatial resolution was 1.25

km. From analysis of refraction data for the same region, the authors estimated that the first arrivals from the 39-km sources were impulsive P_g that refracted along a crustal boundary at about 6-km depth, and the first arrivals from the 85-km sources were a mid-crustal reflected or refracted phase. The raypaths followed by these phases allow resolution to about 5-km depth in the study volume. The velocity model used for the ray tracing was determined from analysis of one refraction line crossing the study volume. For each source a least squares linear regression fit of arrival time versus distance was made; the differences between the observed and best fitting traveltimes (the "residuals") were used as the data in the inversion. The authors assumed that outside of the study volume, the rays from a source traveled through essentially similar crustal structure and therefore did not have significant differences in travel time from the source to the target volume. Therefore the traveltime residuals represent solely the differences in travel time through the study volume relative to the average travel time due to the spatially varying velocity structure in the study volume. These residuals were inverted for P-wave velocity perturbation structure using the ACH block inversion method (Aki et al., 1977) and an offset-and-average smoothing technique (Evans and Zucca, 1988) that reduces the effect of artifacts related to the artificial block boundary formulation. The primary results of the inversion are: (i) a ring of high velocities coincident with the mapped caldera ring fractures, and (ii) a small low-P-wave-velocity anomaly (about 6 percent lower) located about 2.5–4 km below the summit caldera. They interpret the low-velocity zone as a possible magma chamber less than a few tens of cubic kilometers in volume. The resolution matrices suggested that results in adjacent layers may have been somewhat coupled, that is that anomalies may have been elongated somewhat in the vertical direction.

The 3D P-wave velocity structure of the upper 40 km of the crust and mantle beneath Newberry volcano was studied by Stauber et al. (1988). They used P-wave arrival times from teleseismic earthquakes recorded on a 40×60-km array of 15 portable seismographs. The average station spacing was about 5 km, and the stations were operated for 2 months. The study volume was discretized into six layers with blocks measuring 5 km on a side horizontally and about 8 km deep. The relative travel time residuals were inverted for the velocity structure using the ACH technique. The principal finding was a region of relatively high velocities located beneath the volcano from about 5–25 km depth. This zone was interpreted as a region of solidified mafic intrusions, with overall higher density than the surrounding felsic crust.

3.2.3 Medicine Lake Volcano, California

At about the same time as the study at Newberry, Evans and Zucca (1988) completed a similar study of Medicine Lake volcano, northern California. In this study, 140 2-Hz seismographs were deployed in a 12×16-km array over the summit caldera and easternmost rim. The average station spacing was 1.3 km. Eight 1,360- to 1,810-kg chemical explosive sources were deployed in a circular pattern around the array at distances of about 50 km. Previous refraction work indicated that at this distance the first-arriving phase was impulsive P_g with a turning point at a depth of about 5 km. Resolution beneath the array extended to a depth of about 5 km. As with Achauer et al. (1988), the relative first arrival times were picked using a correlation method with an accuracy of about 0.01 s. Then for each source the least squares linear regression fit of arrival time versus distance was made, and the relative travel time residuals calculated. These residuals were inverted for P-wave velocity perturbation structure using the ACH inversion technique with the offset-and-average smoothing technique. In addition to P-wave velocity, Evans and Zucca determined the P-wave attenuation structure beneath Medicine Lake volcano. They used the ($t*$) technique developed by Teng (1968) and used previously to determine attenuation structure in volcanic or partially molten regions using teleseismic sources by Ward and Young (1980),

Young and Ward (1980), and Solomon and Toksoz (1970). The basic operation in this technique is a spectral ratio, which isolates the effects of attenuation in the study volume by removing the effects of the source, common path, and receiver from the problem. For each P-wave seismogram the Fourier spectrum of a windowed portion is found. This spectrum is then divided by the Fourier spectrum of a reference signal. The resultant plot of amplitude versus frequency has a best-fitting line with a slope that is related to the difference in attenuation (differential attenuation) experienced by waves traveling to the particular seismograph and the reference seismograph or seismographs. In this study, the reference spectrum was the average log spectrum per source. In other words, for each seismogram from a given source the amplitude spectrum of the windowed P-wave signal was calculated, then all of spectra, with the amplitudes expressed as logarithms, were averaged to form one average spectrum. Use of the average spectrum as the reference spectrum has the advantage that the reference spectrum is relatively smooth with few spectral holes and thus forms a relatively stable denominator in the spectral division. The spectral-ratio slopes are used as data in an ACH inversion for the differential attenuation structure. The resultant image of differential attenuation in the study volume is relative to the average attenuation in the study volume. The principal results from Evans and Zucca are: (i) relatively high velocity, average attenuation in the upper 2 km of the caldera; (ii) a zone, no larger than a few tens of cubic kilometers, of relatively low velocity (about 6 percent low) and high attenuation at about 2 to 4 km depth beneath the caldera summit, interpreted as a small magma chamber; and (iii) a larger zone of low velocity and high attenuation beneath the southeast flank of the volcano, in an area with no Holocene vents, interpreted as porous, saturated volcaniclastic sediments ponded on the downthrown side of a normal fault cutting the edge of the volcano.

3.2.4 Mount St. Helens, Washington

The P-wave velocity structure in the upper 20 km of the crust beneath andesitic Mount St. Helens volcano has been studied by Lees (1992) and Lees and Crosson (1989). The most detailed results are presented in Lees. The study volume had horizontal dimensions of 27×21 km centered on the summit crater and extended 20 km deep. The volume was parameterized into 22,680 cubic blocks with sides 0.5 km in length. A total of 35,475 P-wave arrival times from 5,454 local earthquakes recorded at 39 local stations were used to invert for the 3D velocity structure in the study volume. The inversion technique required two steps. First, assuming the earthquake locations found with a 1D velocity model and station corrections, LSQR was used to invert for the 3D velocity model. Next, the earthquakes were relocated using the new velocity model and 3D raytracing (Um and Thurber, 1987). These steps were repeated until an acceptable final velocity model was found. During the LSQR inversion in the horizontal direction, the velocity values in adjacent blocks were constrained to vary smoothly according to a Laplacian operator. Because of the smoothing, effective resolution was about 1–2 km. The principal results are as follows: (i) from 0–1.5 km depth beneath the summit crater a zone of relatively high velocities was imaged and was interpreted as a solidified intrusive plug; (ii) from 1.5–3.5 km depth beneath the summit a 2-km-wide zone of relatively low velocities was imaged and interpreted as a hot magma conduit; (iii) from 3.5–6 km depth beneath the summit, the low-velocity zone broadens to about 5 km diameter and is interpreted as a possible shallow magma reservoir; (iv) from 6–9 km depth beneath the summit velocities are relatively high suggesting a plug of solidified intrusive material; and (v) beneath 9 km depth, data are sparse, however velocities are relatively low which would be consistent with the presence of a magma chamber suggested by other seismic, geological, and geodetic studies.

3.2.5 San Francisco Peak, Arizona

The two-dimensional (2D) P-wave velocity structure of the crust and mantle to depths of about 90 km beneath the San Francisco Peaks was investigated by Stauber (1982). He used P-wave arrival times from teleseismic earthquakes recorded on a 250×50 km cross-shaped seismograph array centered on San Francisco Peak. Inversions of relative traveltime residuals for the 2D velocity perturbation structure beneath the linear arms of the array were performed with the ACH technique. He found a 6-km-wide low-velocity body extending from 12–26 km directly beneath San Francisco Peak, a stratovolcano. The velocity decrease was about 6 percent relative to the surrounding rock. He interpreted this as a zone of either high temperatures, partial melt, or high fracture density with interstitial fluids.

3.2.6 The Geysers Geothermal Field, California

The 3D P-wave velocity structure of the upper 60 km of the lithosphere beneath The Geysers geothermal area was studied by Oppenheimer and Herkenhoff (1981). They used relative P-wave traveltime residuals for 94 teleseismic earthquakes recorded on 44 local 1-Hz seismographs and the ACH technique to invert for the local 3D velocity structure. The relative traveltime residuals were calculated by subtracting the theoretical Herrin (1968) traveltimes from the observed traveltimes and then subtracting the mean residual per event. The study volume was discretized into blocks with dimensions of 10×10×15 km in four layers. The results indicate a large volume of rock with low P-wave velocities. In the upper 15 km, velocity reductions reach 20 percent; the low-velocity volume diminishes in magnitude with depth, but seems to extend to at least 60 km depth. The low-velocity volume has a diameter of about 20–30 km and is centered about 10 km northeast of the producing geothermal field. Gravity field perturbations predicted from the velocity perturbations compare well with the observed gravity field. Together these suggest reduced densities possibly due to partial melting.

The 3D P-wave velocity structure of the upper 5 km of the crust beneath The Geysers geothermal area was investigated by Eberhardt-Phillips (1986). She used Thurber's (1983) technique to simultaneously invert traveltimes of P waves from over 100 local earthquakes and a couple of explosions for the 3D velocity structure and earthquake locations. The 18×16×5-km study volume was parameterized with grid points every 2–3 km. The results indicate somewhat lower velocities (5–10 percent low) in the 2–5-km depth range beneath the steam production field. Majer and McEvilly (1979) found low V_P/V_S in the steam-dominated production zone at The Geysers.

3.2.7 Larderello Geothermal Field, Italy

The P-wave velocity structure in the crust and upper mantle beneath the Larderello geothermal field, Italy, was investigated by Foley et al. (1992). The authors used teleseismic arrival times from 101 earthquakes out of 224 recorded during 1985–1987 and the ACH inversion method to determine the seismic structure in the 6–41-km depth range. The velocity structure in the upper 6 km was taken from seismic reflection results. The block model had a 35×40×41-km volume with block dimensions of 7×7×5 km from 6–21 km and 7×7×10 km from 21–41-km depth. Gravity and seismic reflection data suggest that the Moho lies at less than 20 km depth in this region. The P-wave arrival times were picked using an automated routine, and relative traveltime residuals were calculated with respect to the Herrin (1968) whole-earth velocity model. The maximum traveltime residual difference between the center of the geothermal field and the periphery was 1.0 s, similar to that found at The Geysers geothermal field, California (Oppenheimer and Herkenhoff, 1981). The primary result of the inversion is an approximately

15–20-km-diameter zone centered on the geothermal field with velocities reduced by as much as 16 percent from 6–16 km depth and by as much as 10 percent from 16–31 km depth. Analysis of teleseismic waveforms by Foley et al. (1992) suggests that the low-velocity volume may be formed of many smaller low-velocity bodies. The maximum Bouguer gravity low associated with the geothermal field is 20 mGals, similar to 30 mGals at the Geysers (Iyer, 1984) and 50 mGals at Yellowstone (Ellsworth, 1977). Maximum temperatures of 350 °C are found at 2 km depth in the active geothermal zone. In addition, a prominent seismic reflection horizon shallows toward the center of the geothermal field, in rough agreement with the maximum depth of seismicity. Based on all of these observations, the authors suggest that the low-velocity volume is a zone of solid, partially melted, and fully melted materials.

At the nearby Travale Geothermal Field, Hirn and Ferrucci (1985) analyzed P- and S-wave arrivals from local, regional, and teleseismic earthquakes recorded on a very dense local seismograph network. Twenty stations were located within a 3×3-km area giving a spatial resolution of several hundred meters. The seismographs were three component, so accurate readings of the S- as well as P-wave arrivals could be made. One very significant observation came from the recordings of 1-Hz waves from a M 5.6 earthquake that occurred 5,000 km away. Clear arrival time delays of about 0.2 s were measured at two stations. Because the nearby stations which recorded arrivals without traveltime delay were located from 0.3–1.0 km away, the heterogeneity responsible for the traveltime delay must have dimensions of less than about 1 km and must be located in the upper 1–2 km of the crust. The region in question lies beneath one of the most productive wells in the geothermal field. Thus, it appears that even waves with wavelengths of 4–5 km can provide information on near-surface heterogeneity with dimensions on the order of 1 km. The other result of the study was the observation of high V_P/V_S ratio associated with the water-dominated parts of the field, and low V_P/V_S associated with the steam-dominated parts of the field. Ferrucci and Hirn (1985), using the spectral ratio technique with PMP waves from regional earthquake, find relatively high P-wave attenuation in the geothermal production field.

3.2.8 Milos Island Geothermal Field, Greece

The Milos Island geothermal field, Greece, associated with andesitic volcanism, was investigated by Hirn et al. (1989). The geothermal reservoir appears to be contained in fractured Alpine metamorphic rocks that are covered by about 1 km of recent volcanic rocks. Local earthquakes in the study area are located deeper than about 4 km. The study volume had horizontal dimensions of about 10×10 km and extended about 6 km deep. Thirty triggering, three-component seismographs were deployed for about 3 months; the stations locations were changed several times to give a total of about 100 different station locations. P- and S-wave arrival times from 72 local earthquakes were used in a joint inversion for 3D velocity structure and earthquake locations. The spatial resolution was about 1 km. The primary result was the image of low S-wave velocities and high V_P/V_S ratio in the geothermal zone at about 2 km depth. These results suggest that the geothermal reservoir is in a highly fractured zone with fluid (not gas) filling the fractures, consistent with drilling data.

The Milos geothermal field was investigated also by Ochmann et al. (1989). They used P- and S-wave arrival times of 90 local earthquakes recorded at about 25 three-component, 1-Hz seismograph stations, which did not all operate at the same time (1,067 ray paths), to invert for the 3D P-wave velocity structure and to map the average V_P/V_S ratio in the region. The average station spacing was about 3 km, and the study volume had dimensions of 8×10×8 km. Thurber's (1983) ACH inversion

code was used to simultaneously invert for 3D P-wave velocity structure and earthquake hypocenters. The primary result of the inversion was the image of relatively high P-wave velocity in the upper 3 km of the crust beneath the geothermal production zone. Using the earthquake origin times found during the inversion and the measured P- and S-wave arrival times, the authors then calculated the average V_P/V_S ratio along each ray, and mapped the average V_P/V_S ratio at each station. The resulting map showed relatively low V_P/V_S ratios associated with the geothermal production zone. The authors focusing on these low V_P/V_S ratios suggest that they are due to high temperatures and/or a small amount of gas in the geothermal fluids. However, one inconsistency never discussed by the authors is the relatively high V_P values imaged in the geothermal zone, which would support an opposite conclusion about the properties of the zone.

3.2.9 Campi Flegrei Caldera, Italy

The 3D P- and S-wave velocity structure of the upper 3 km of the crust in the Campi Flegrei were studied by Aster and Meyer (1988). They used arrival times of 1,842 P-waves and 1,006 S-waves from 228 well-located local earthquakes and Thurber's (1983) program to invert for the P- and S-wave velocity structures. The study volume was discretized into nodes 1 km apart. The results indicate a zone with relatively low V_P, low V_S, and high V_P/V_S values (some greater than 2.0) coincident with an aseismic region and with the region of maximum ground uplift. This zone is interpreted as an incompetent, highly fractured volume, saturated with water. This fluid zone lies in the upper 2 km of the crust above an approximately 2-km-thick zone of earthquakes. The earthquakes lie a kilometer or so above the magmatic source region for the ground uplift.

3.2.10 Redoubt Volcano, Alaska

The P-wave velocity structure beneath Redoubt Volcano, Alaska, was imaged from tomographic inversion of arrival time data from local earthquakes and four explosions (Dawson et al., 1990). The study volume laterally covered the flanks of the volcano and extended to a depth of 6 km and was represented by a grid of nodes with a spacing of $1 \times 1 \times 1$ km. The principal results of the inversion are the following: (i) a thin low-velocity layer that drapes a higher velocity core of the volcano, and (ii) a 1–2-km^3 volume with 6-percent lower velocities centered 2 km beneath the crater. The low-velocity volume is found to lie just below the locations of a swarm of long-period tremors, suggesting that the long-period sources were related to pressure release from the interaction of a magma reservoir and the shallow hydrothermal system.

3.3 BASALTIC VOLCANOES

3.3.1 Hawaii

The 3D P-wave velocity structure of the upper 75 km of the lithosphere beneath Kilauea volcano was investigated by Ellsworth and Koyanagi (1977; also Ellsworth, 1977). Relative P-wave traveltime residuals from 160 teleseismic earthquakes recorded at 26 1-Hz seismographs of the Hawaii array were inverted for velocity structure using the ACH technique. The residuals were relative to the Herrin (1968) global model and to the event mean residual. The $70 \times 70 \times 75$ km study volume was discretized into blocks with dimensions of $7.5 \times 7.5 \times 15$ km. The results indicate an absence of strong lateral velocity

variations, in contrast to the results of Iyer et al. (1981) at Yellowstone where a clear low-velocity zone is seen beneath Yellowstone to depths of about 200 km. The principal heterogeneities that do exist are relatively high velocities within the central summit complex and along the two rift zones compared with the nonrift flank of the volcano. Thus, there is no evidence for substantial volumes of partial melt within the crust and mantle to depth of at least 40 km. The results agree well with seismic refraction and gravity results.

The 3D P-wave velocity structure of the upper 10 km of the crust beneath Kilauea volcano and the east and southwest rift zones was investigated by Thurber (1984). He used arrival times of P waves from 85 local earthquakes and 2 explosions recorded at about 20 stations. The data set and method permitted spatial resolution of about 3–4 km. The arrival times were simultaneously inverted for earthquake locations and 3D velocity structure with an iterative least-squares algorithm. Also a fast, approximate 3D raytracing scheme was utilized. The $20 \times 30 \times 10$-km study volume was discretized into nodes with spacing of $4 \times 3 \times 3$ km. Velocity was interpolated between nodes. The results indicate relatively high P-wave velocities at most depths associated with the Kilauea volcano and its rift zones. The exception was a zone of low velocity at about 3 km beneath the volcano summit. This low-velocity zone coincided with an aseismic zone, and is interpreted as a zone of high temperatures and possibly melt accumulation. Relatively low velocities are found in association with the major fault systems in the region.

The 3D P-wave velocity structure of the upper 20 km of the crust beneath Mauna Loa and Kilauea volcanoes, Hawaii, was studied by Rowan and Clayton (1993). They used P-wave arrival times from 12,295 local earthquakes recorded at 42 stations. The traveltime residuals were calculated relative to the 1D P-wave velocity model determined for the region from seismic refraction studies. The earthquakes were located over a wide depth range, with 452 from 0–5 km, 565 from 5–10 km, 196 from 10–15 km, and 19 from 15–20 km. Station spacing varied but was generally in the range of 5–20 km. Two study volumes were identified: a coarse grid ($5 \times 5 \times 5$ km) that included Mauna Loa, Kilauea, and the East Rift Zone, had dimensions of about $100 \times 45 \times 20$ km; and a fine grid, that included only Kilauea and the East Rift Zone, had dimensions of $60 \times 30 \times 8$ km. The traveltime residuals were inverted for velocity structure using the damped SIRT algorithm described above. The results were smoothed with a weighted 9-point average filter, and for the fine model, results in adjacent layers were averaged to give effective block sizes of $1 \times 1 \times 2$ km. The resulting fine-model images show relatively slow velocities in the 0–2-km depth range beneath Kilauea and the East Rift Zone, and relatively fast velocities from 2–6 km depth. The coarse-model images show low velocities between Mauna Loa and Kilauea from 0–10 km depth, and relatively normal velocities from 10–20 km; velocities along the East Rift Zone are generally normal to fast.

The S-to-P amplitude ratio technique with radiation pattern corrections was used by Ho-Liu (1988) to study the shallow magmatic system in the Kilauea-East Rift Zone region of Hawaii. She used 1,380 S-to-P amplitude ratios measured from vertical-component seismograms recorded by the 53-station Hawaiian seismic array. The average station spacing in the study area was between 5 and 10 km. The 63 local earthquakes used were selected from hundreds cataloged to provide good azimuthal and depth coverage. The earthquake depths range from near the surface to about 50 km. Two study volumes were delineated; a larger study volume had block sizes of $2 \times 2 \times 1$ km, dimensions of $92 \times 52 \times 50$ km, and included Mauna Loa, Kilauea, and the East Rift Zone; a smaller study volume with block sizes of $1 \times 1 \times 1$ km had dimensions of $55 \times 22 \times 50$ km focused on Mauna Loa and the East Rift Zone. Rays were traced with the 1D velocity model of Hawaii determined from previous seismic

refraction studies. The amplitude ratios were inverted for Q_S structure using the damped SIRT algorithm. The results reveal the locations of the low-Q_S shallow magmatic system associated with the volcanism at Kilauea and along the East Rift Zone. The low-Q zones beneath Kilauea, Mauna Ulu, and Puu Oo begin in the upper 2 km and extend to about 10 km depth. Other parts of the East Rift Zone, which begins at Kilauea and extends east through Mauna Ulu and Puu Oo, are marked by a curvilinear zone of low-Q that is recognizable in the 2–4 km depth range, is very strong in the 4–6 km depth range, and seems to die out below 6 km. Only a minor low-Q anomaly in the 4–6 km depth range is associated with Mauna Loa. Between 4 and 8 km depth low-Q is associated with the Hilina fault zone area. Ho-Liu (1988) and Ho-Liu et al. (1989) compared the attenuation models resulting from inversion of the S-to-P amplitude ratios with both the SIRT algorithm and a formal inversion without blocks. They find a good comparison between the models resulting from the two inversion techniques.

A special application of the spectral decay technique has been made by Scherbaum (1990). He uses the technique to invert for both Q structure and earthquake source parameters in the Kaoki earthquake zone, Hawaii. In his formulation, the P-wave spectrum is fit with a source model that has a f^2 high-frequency decay rate to obtain the seismic moment and corner frequency and with a path-average Q factor to account for additional high-frequency decay. The spectra from many earthquakes are measured, and the resulting path-average Q values are inverted with an algebraic scheme for the 3D Q structure. Next, this 3D Q structure is used in a formal inversion for improved source parameters, including new path-average Q estimates. These two steps are repeated until model improvement is minimal. In the Kaoki study, Scherbaum and Wyss (1990) correlate the final Q structure with seismicity and surface faulting and suggest that regions of relatively low-Q are related to zones of increased crack density.

3.3.2 East Pacific Rise

The P-wave velocity structure of an 18-km segment of the East Pacific Rise just south of the Clipperton fracture zone was tomographically imaged by Toomey et al. (1990). They used an 18×16-km array of 15 ocean-bottom seismographs and 375 explosions. The explosions were all located within the array, had a uniform size of 54.5 kg, and a spacing of about 0.5 km. In total, 4,278 travel-time observations were inverted for 3D P-wave velocity structure using the ACH inversion code of Thurber (1983) with 3D raytracing (Um and Thurber, 1987). Spatial resolution in the model was about 1 km to a depth of about 5 km. The significant results include: (i) a linear high-velocity anomaly above 1 km depth in the crust, about 1–2 km in width, centered on the rise axis; and (ii) a linear low-velocity anomaly at depths of 1–3 km, centered on the rise axis, with a cross-sectional area of about 2×2 km. The velocities in the low-velocity volume are reduced by 1–2 km/s relative to normal velocities. Murase and McBirney (1973) reported a 1–2 km/s decrease in P-wave velocity when they increased the temperature on laboratory rocks from room temperature to just below the solidus. Thus, the tomographic results are consistent with high subsolidus temperatures in the low-velocity volume. Independent seismic reflection data suggest a liquid sill-like feature at 1.6–2 km depth beneath the rise summit with P-wave velocity of about 3 km/s. Thus, at least the upper part of the low-velocity volume imaged tomographically may contain partial melt.

3.4 SOUTHERN CALIFORNIA

The 3D P-wave velocity structure of the crust and upper mantle to a depth of 750 km beneath southern California has been imaged by Humphreys et al. (1984) and Humphreys and Clayton (1990). They used P-wave arrival times from about 160 teleseismic earthquakes recorded on up to 158 seismographs of the southern California seismic array. The average station spacing in the central portion of the array is about 20 km. A total of about 10,000 arrival times were used. Each station recorded an average of 63 earthquakes, and each earthquakes was recorded by an average of 61 stations. Relative traveltime residuals were calculated by first correcting for station elevation and substation sediment thickness, then Herrin (1968) theoretical traveltimes were subtracted, and finally the average residual for each earthquake was subtracted. The 350×550×750-km study volume was discretized into blocks 15 km on a horizontal side and 30 km deep, for a total of 47,175 blocks. A 1D velocity model specific to the nearby Gulf of California was used to guide the raypaths and as the reference velocity in the model blocks. A SIRT algorithm with added smoothing operations was used to invert the residuals for the velocity perturbation in each block. The results indicate a 60-km wide and 120–250-km deep region of 3-percent high velocities beneath the Transverse Ranges, and a 70–100-km deep region of 3–4-percent low velocities beneath the Salton Trough.

3.5 NEVADA TEST SITE

The 3D P-wave velocity structure of the crust and upper mantle to a depth of about 300 km beneath the Nevada Test Site region in general and beneath Yucca Mountain in particular was investigated by Evans and Smith (1992). They used teleseismic P-wave arrival times recorded during 1979–1980 on seismographs located in a 300-km-diameter analog seismic array centered on the Nevada Test Site for the larger-scale velocity structure study, and they used arrival times recorded in 1982 on a 40-km-diameter digital seismic array centered on Yucca Mountain for the small-scale velocity structure study. The ACH technique as modified by Evans and Zucca (1988) was used to invert the relative traveltime residuals for 3D velocity perturbation structure. The larger study volume was discretized into blocks with dimensions of about 25 km horizontally and about 45 km vertically, and the smaller study volume was discretized into blocks with dimensions of about 4 km horizontally and 8 km vertically. The horizontal dimensions of the blocks are similar to the average station spacing in the arrays. There are four primary results. First, a large volume of high-velocity rock (3 percent higher), circular in plan, is imaged beneath the Silent Canyon caldera and the northern part of the NTS from near the Moho to depths of about 200 km. This is interpreted as possibly the cooled residuum of the source region for the southwestern Nevada volcanic field. Second, a large volume of low-velocity rock (3 percent lower), elongate E-W in plan, is imaged abutting the southeast margin of the Test Site in the same depth range as the high-velocity anomaly described above. This is interpreted as possibly a region of high subsolidus temperatures or partial melt. Third, in the fine-scale study volume, a region of low velocities is imaged beneath Crater Flat in the middle and lower crust. These low velocities are interpreted as possibly indicating high temperatures related to the volcanism in Crater Flat. Fourth, in the fine-scale study, a shallow low-velocity anomaly associated with the Crater Flat basin extends eastward into the repository site, suggesting a possible structural boundary within the site. The large- and fine-scale images clearly rule out magmatism on the scale of Yellowstone or Long Valley. The small-scale images rule out mid-crustal magma chambers larger than 4 km in diameter within 10 km of Yucca Mountain, but cannot be used to resolve finer scale features.

4 POTENTIAL OF TOMOGRAPHY TO IMAGE SMALL VOLUME MAGMA ACCUMULATIONS

The primary constraints on the resolution of the image resulting from tomographic analysis are the number and distribution of sources, the number and distribution and quality of seismograph stations, and the wavelengths of the waves used. In general, spatial resolution will be finer if more stations are used and they are located closer together. Also, in general, resolution and error will improve as more sources are used and as the sources are more evenly distributed so that rays penetrate all regions of the study volume from many different directions. For all techniques, the spatial resolution is thought to be limited to dimensions similar to or larger than the dominant wavelengths of the waves used in the analysis. However, as was noted by Hirn and Ferrucci (1985), local 1-km scale heterogeneity may significantly effect the travel time of 4-km wavelength waves. Thus, perhaps with the use of very tight seismograph arrays the resolution with teleseismic waves can be smaller than the dominant wavelength of the waves, especially in the near surface. For the techniques that use data from teleseismic earthquakes, such as ACH, and for the NeHT technique, the spatial resolution in the horizontal direction can be similar to or larger than the average spacing between stations.

The tomographic imaging studies described in Section 2 reveal a range of possibilities for investigating the crustal and upper mantle structure in regions of recent volcanism. The finest spatial resolution obtained was on the order of 1 km. This resolution was achieved in both studies that used explosions and the NeHT technique to image shallow crustal velocity structure and in those studies that used local earthquakes to image shallow crustal attenuation structure. The finest resolution possible using teleseismic sources was about 4 km horizontally and about 8 km vertically.

Using the NeHT technique and sufficient stations and sources, a spatial resolution of 0.5 km may be possible. With the NeHT technique, the depth dimension of the study volume is limited to less than the diameter of the station array. If local earthquakes are used as sources, then spatial resolution will be limited by the uncontrollable distribution of source locations and also by the error in the hypocentral locations, which for well-located earthquakes is usually on the order of 0.5–1 km. In regions of interest without local earthquakes, either the NeHT technique with explosion sources or techniques that utilize teleseismic sources must be used to image the structure.

There are advantages and disadvantages to each technique. The techniques that utilize earthquakes as sources of seismic waves have the advantage that the sources are provided free of charge. Also earthquakes generate S waves as well as P waves, thus the shear properties of the study volume can be imaged in addition to the compressional properties, helping to reduce ambiguities is interpretations. With teleseismic earthquake sources, the depth dimension of the study volume can extend into the upper mantle; with local earthquake sources, the study volume can be as deep as the deepest earthquakes, usually on the order of 10–20 km. One drawback with earthquake sources is that they may have spatial and temporal distributions that are not optimal for obtaining clear tomographic images. Also, in order to obtain sufficient high quality seismograms for analysis, the seismic array may need to be deployed for many months to a year, thus increasing cost. The NeHT technique that uses explosion sources has the advantage that the positions and number of sources are completely controllable; this allows a more-optimal ray distribution in the study volume, which can improve image clarity. Another advantage is that the experiment can be performed within a relatively short period of time. The disadvantages to the NeHT technique are the expense of drilling and explosive material, the generation of only P waves, and the limited depth of resolution in the study volume.

5 SURVEY DESIGN FOR SEISMIC TOMOGRAPHY STUDY OF A SMALL VOLUME VOLCANIC FIELD

5.1 TYPES OF STUDIES

Three basic types of seismic tomography studies for imaging lithospheric structure beneath a small volume volcanic field are described below. Each study is designed to answer a particular question. Decreasing in degree of complexity the studies are the following: (i) 3D upper crustal structure using NeHT tomography, (ii) 2D crust and upper mantle structure using teleseismic tomography, and (iii) volume of intrusive rock in alluvial basin using refraction. These studies are presented to illustrate how tomographic methods can best be used to identify and map low velocity zones of subsolidus temperatures or, partial melt such as might be present beneath cinder cone clusters and dike complexes beneath cinder cones and cinder cone alignments, like the Crater Flat alignment.

5.2 NeHT TOMOGRAPHY FOR THREE-DIMENSIONAL UPPER CRUSTAL STRUCTURE

5.2.1 Resolution Desired and Station Spacing

The spatial resolution desired is 1 km or less. The spacing between stations of the seismic array will depend on the resolution possible given the wavelength of the incoming seismic waves and on the resolution desired. In general, the spatial resolution of the seismic parameters in the model volume can be no smaller than the average station spacing in the array at the surface. Also, in general, the spatial resolution cannot be much smaller than the dominant wavelength of the seismic waves recorded by the array. In NeHT tomography, where near-regional explosive sources are used, the dominant wavelengths are on the order of 0.5–1 km, thus 1-km spatial resolution is possible, and the average station spacing should be 1 km or less.

5.2.2 Size of Seismic Array

In NeHT tomography, the areal extent of the seismic array will be limited by the distance over which waves from a particular refracting horizon are received as first arrivals (if refracted arrivals are used), the distance over which waves from a particular reflecting horizon are received (if reflected arrivals are used), the instrument spacing desired, and the number of instruments available for use. The depth of the study volume is limited by the bottoming depth of the waves used, which is determined by the depth of major refractor or reflector horizons in the crust. For instance, if the waves used in the analysis have refracted at depths of around 6 km, then the study volume must lie above this depth. Assuming typical ray paths in the upper crust, the seismic array must be about 6 km in diameter in order to image the crust to a depth of 6 km. For array diameters greater than 6 km, no increase in depth of study is obtained, but an increase in the lateral region of study is obtained.

Usually the limiting factor is the number of seismographs available for use coupled with the desired station spacing. If an average station spacing of 1 km is desired, then the number of stations required is about equal to the square of the array diameter in kilometers. For instance, for a 10-km diameter array, about 100 seismographs are needed.

5.2.3 Types of Seismic Equipment

Because the waves recorded are predominately high frequency (> 1 Hz), standard 1- or 2-Hz seismometers are adequate. Also because only P waves are analyzed, only the vertical component is needed at each station. The seismographs should record digitally at 100 samples/s or greater (in order to give arrival time pick accuracy of 0.01 s or less). The seismographs also should not be triggered but should have the capability to begin recording automatically and continuously after a preset time.

5.2.4 Location and Number of Shots

The explosive shot locations are dictated by the crustal velocity structure in the region of the study volume. It is important to have pre-existing information on the 1D or 2D velocity structure of the crust in the study region from refraction profiles. The P waves used in the analysis are either the first arriving waves which have refracted from a velocity discontinuity in the upper crust at depths on the order of about 6 km, or the waves which have reflected from a velocity discontinuity in the mid to lower crust at depths on the order of 15–30 km, or both. The wave or waves used and the depths of refraction or reflection will vary with the velocity structure in the region of the study.

In the YMR, constraint on the upper crustal structure has been obtained from several seismic refraction lines studied by Hoffman and Mooney (1984). Their data suggest that at distances of 45–60 km from a shot location, the first arriving P waves have refracted at about 5–6 km depth, and in addition a later phase is observed that is a reflection from a boundary at about 16 km depth (Figure 5-1). Thus, in order to take advantage of arrival time from both phases, shot locations should be chosen in a radius of 45–60 km from the study area.

The shots are spaced as evenly as possible around the circumference of a circle with the given radius. Access to sites where drilling equipment can be brought and used and where a large underground explosion can be detonated may have some influence on the exact locations of individual shots. At distances of 45–60 km, the shots will be 400–550 kg in size.

The accuracy and resolution of the tomographic images improves generally as the number of shots increases, up to some limiting amount. Previous studies have used from five to eight shots (Nercessian et al., 1984; Achauer et al., 1988; Evans and Zucca, 1988). This is within the range where the resolution and accuracy will improve with the number of shots. The final decision depends on the resolution and accuracy desired and the cost of additional shots. In the synthetic experiment described below, the increase in resolution and accuracy from six to eight shots was significant enough to warrant the expense of the additional shots.

5.2.5 Duration of Field Experiment

The total duration of the field portion of the experiment should be less that about one week. After shot sites have been determined, the driller can be sent ahead of time to drill the 6-inch shot holes to depths of about 30 m. Each hole is then capped and left ready for explosive installation and detonation. The most labor-intensive portion of the experiment is the installation of the seismometers and seismographs. This is best performed relatively quickly (in one or two days) with as many workers as possible. Each seismometer must be buried shallowly in the ground at the selected sites and the seismographs must be attached to the seismometer and power (batteries, solar panels) turned on and

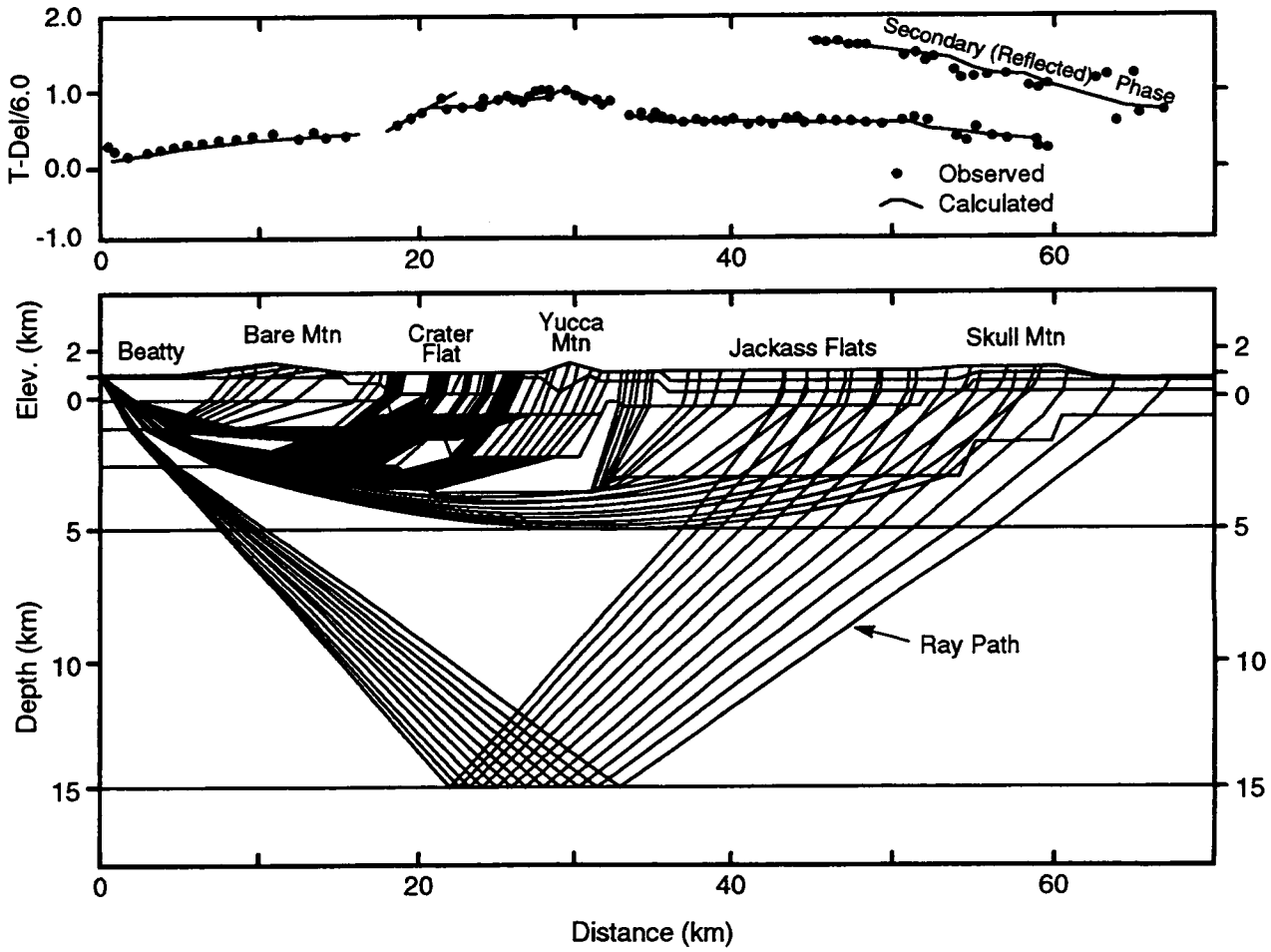

Figure 5-1. Yucca Mountain seismic refraction results and velocity model (Hoffman and Mooney, 1984)

programmed. Once the instruments are in place and operational, the shot holes can be filled with explosives and detonated. This is done usually by one or perhaps two crews, and the shots are detonated in sequence. The seismometer clocks are calibrated throughout the experiment because each uses the same signal transmitted by satellite. Instrument response is only important in some attenuation experiments. If these techniques are used, the seismometers should be calibrated before and after the experiment. After all shots have been successfully fired, the seismographs must be picked up and returned to storage.

5.2.6 Synthetic High-Resolution Tomography Experiment

In order to investigate the experimental requirements for performing a high-resolution (NeHT) tomography survey in an area of potential small-volume basaltic volcanism, such as Yucca Mountain, a synthetic tomography experiment was performed on a computer. The primary goal of a real experiment would be to image the compressional-wave velocity structure with a spatial resolution of 1 km or less in the upper crust beneath the area of interest. This synthetic experiment allowed the various experimental parameters to be investigated in order to meet experimental goals.

As was discussed above, based on the velocity structure in the Yucca Mountain area determined from refraction studies, the distance from the study area to the shot locations was determined to be optimal at 45–60 km. Also, based on previous studies of this type performed elsewhere, the number of shot points was chosen to be eight (Figure 5-2).

Based primarily on an assumption that the number of seismographs available for use would be on the order of 100 (e.g., Achauer et al., 1988; Evans and Zucca, 1988), a 10×10-km square array configuration with stations spaced 1 km apart was simulated. The seismic array was centered on the Yucca Mountain repository site (Figure 5-2). The study volume extended from the surface to 10 km depth, though resolution was significant only down to about 6 km depth. Thus the study volume consisted of 1-km cube blocks within which we inverted synthetic data for velocity anomaly structure (Figure 5-3).

Raypaths of first arriving P waves from the shot points to the stations were traced through the site-specific 1D P-wave velocity model of Hoffman and Mooney (1984). All of these rays refracted at a depth of about 6 km (Figures 5-1 and 5-4).

Two different synthetic anomaly models were tested. In the first synthetic model, an anomalous block with 5-percent low velocity was placed in the 1–2-km layer near the center of the study area, and anomalies with +1 percent or −1 percent were placed alternately in every other block (Figure 5-5). This experiment provides a sense of the resolution that can be achieved easily, where strong velocity heterogeneity is present at shallow depth, for example, associated with high-temperature zones. Synthetic travel-time-residual data were created by tracing each ray through the synthetic anomaly model. To further simulate real conditions, random Gaussian error with standard deviation of 0.005 s (one-half of the arrival time picking accuracy) was added to each data point.

These data were then inverted using the LSQR routine for the velocity perturbation structure in the blocks of the study volume. The results (Figure 5-6) indicate that the position and 76 percent of the amplitude of the −5 percent anomaly was recovered by the inversion. The +1 percent and −1 percent anomalies were not consistently recovered. The depth of significant resolution was 5 km.

In the second synthetic anomaly model, a block with −5-percent velocity was placed in the 2–3-km layer near the center of the study area, a 3×3-km area with +1-percent velocity was placed in the 0–3-km layers near the northwest corner of the study area, and a 3×5-km area with −2-percent

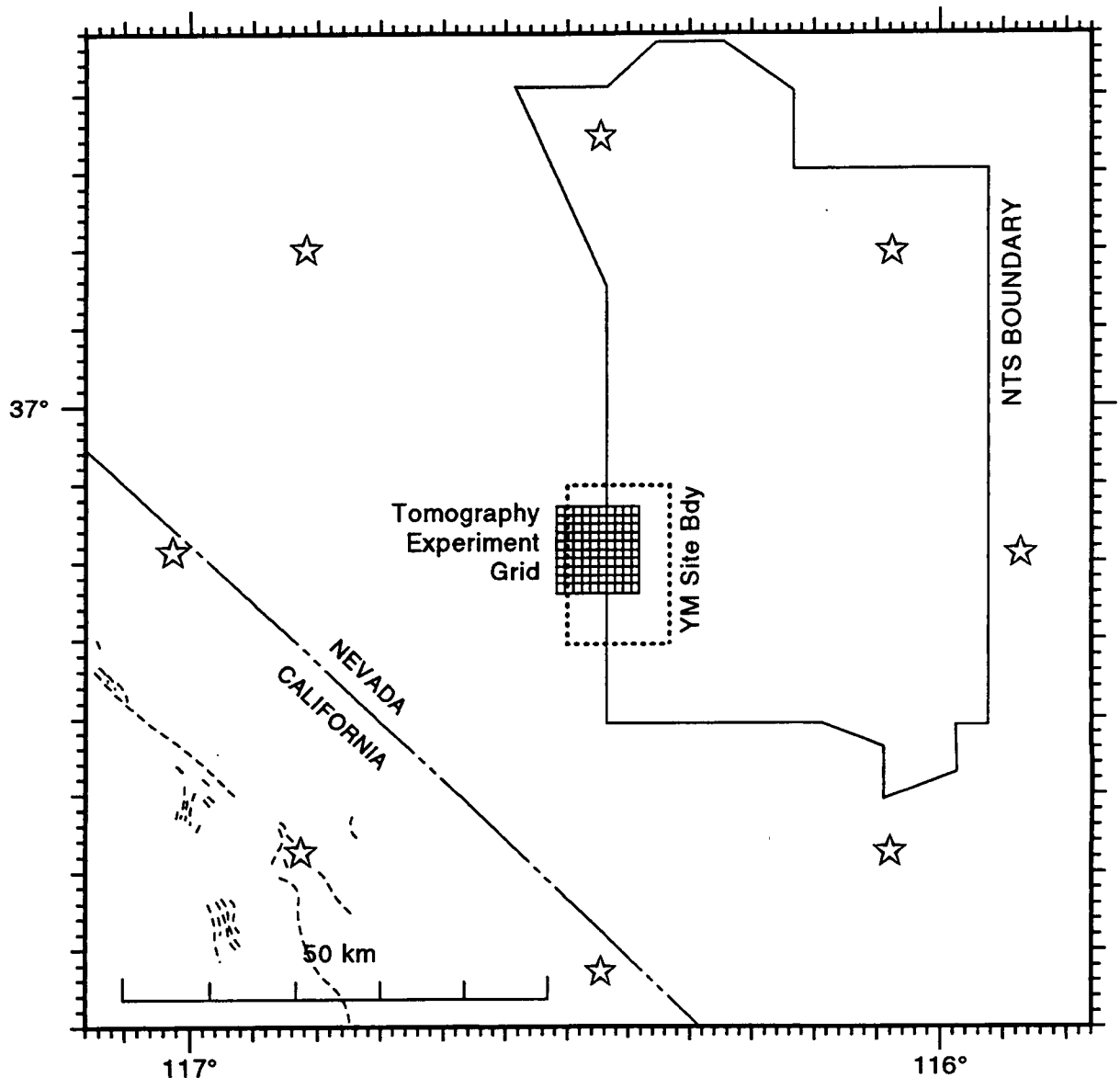

Figure 5-2. Location of synthetic NeHT tomography study at Yucca Mountain. Shot locations are marked by stars, and other boundaries are labeled.

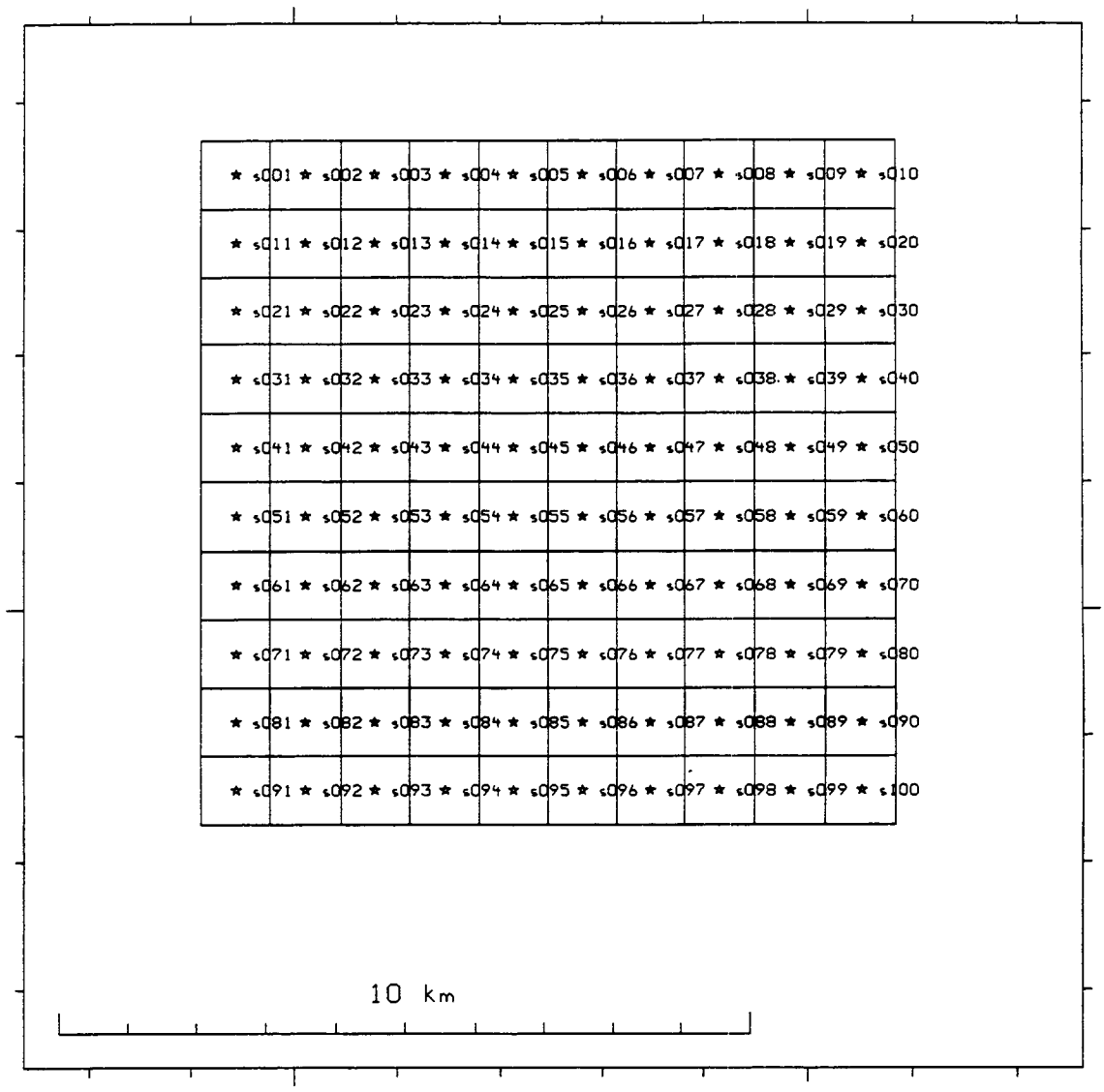

Figure 5-3. Station locations within seismic array in study area

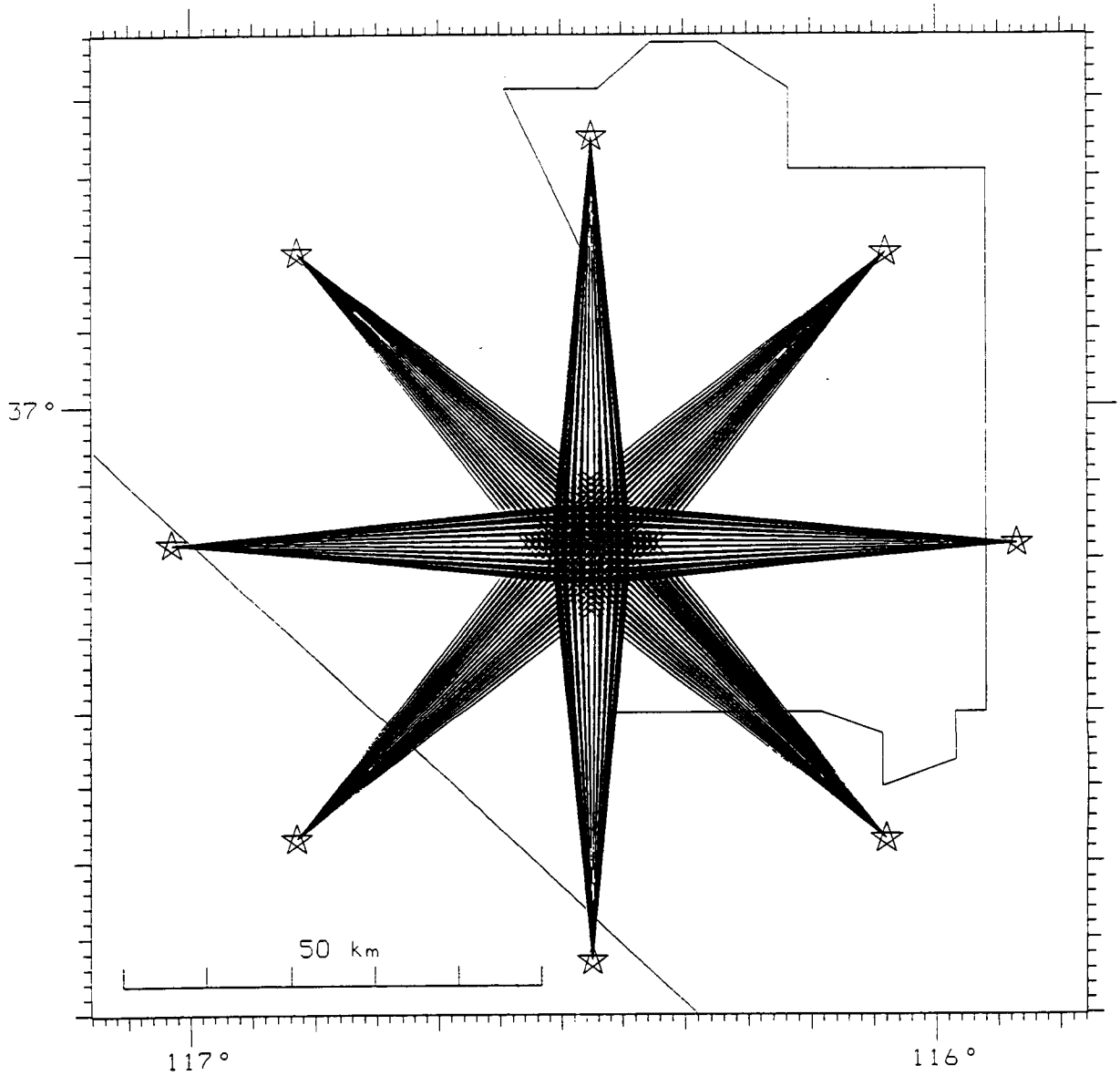

Figure 5-4. Raypaths from the 8 explosion sources to the 100 seismographs of the seismic array

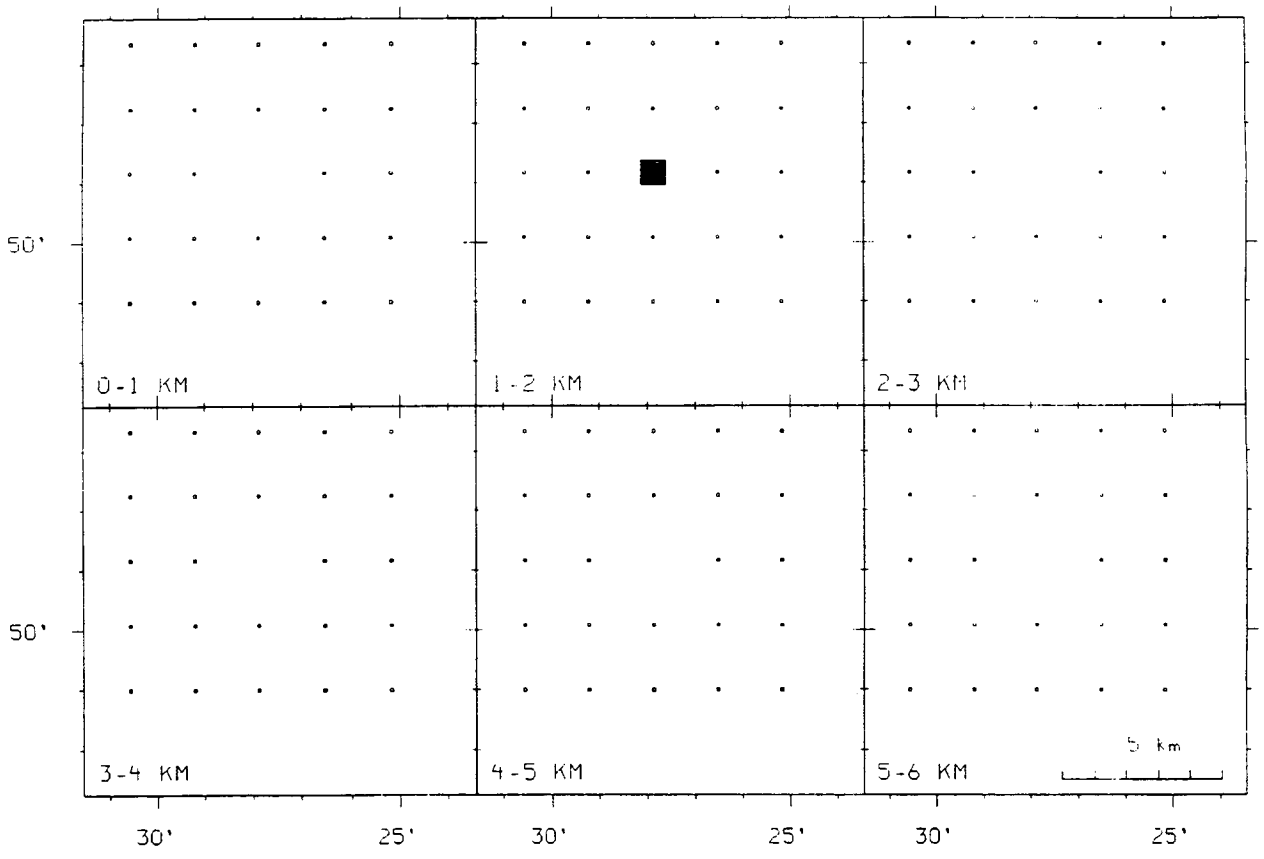

Figure 5-5. Synthetic P-wave velocity model #1. The velocity anomalies are shown at grid points in six, 1-km thick layers. The magnitude of the anomaly scales with the size of the square, and the sign of the anomaly is positive if the square is filled and negative if the square is open. The large filled square in the 1–2-km layer has −5-percent velocity; all other squares shown are either +1 percent or −1 percent.

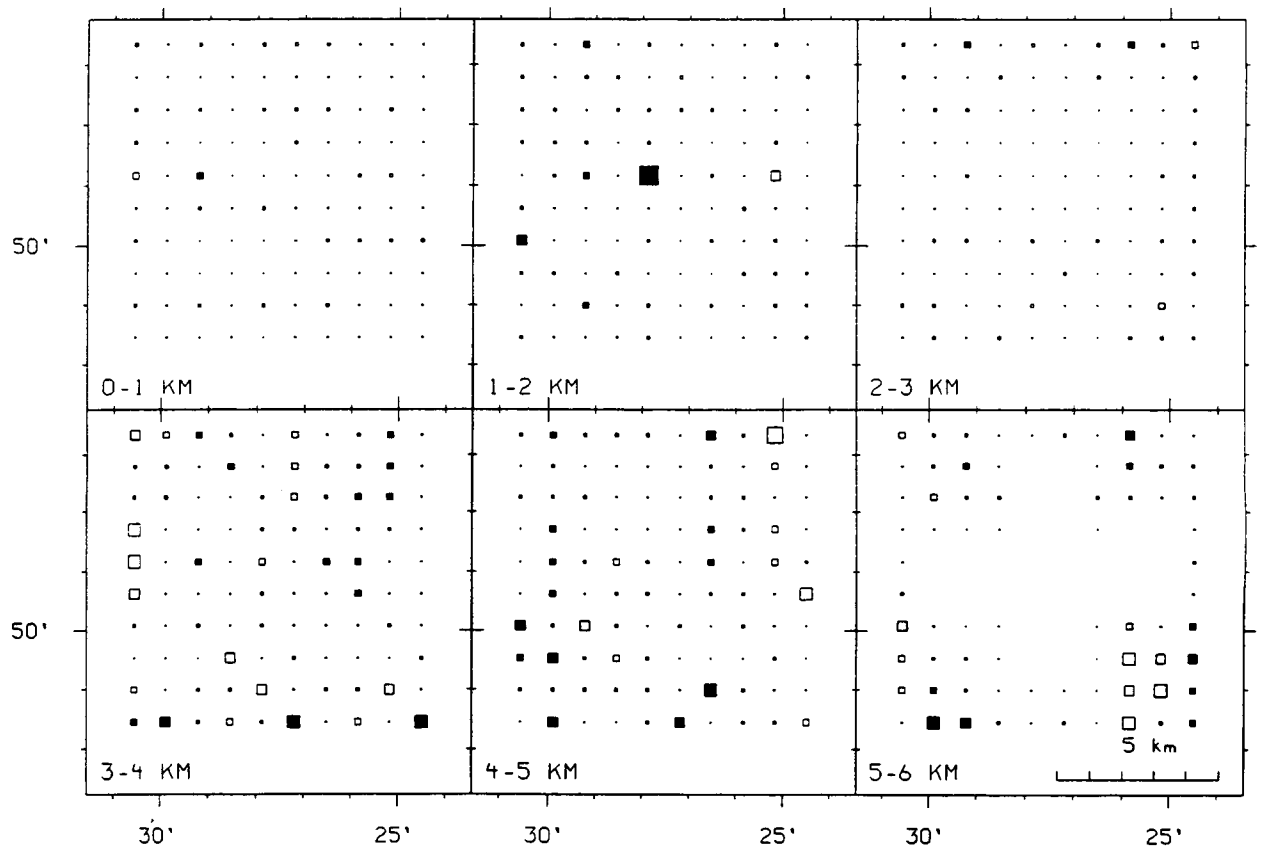

Figure 5-6. Results of inversion of synthetic travel-time delay data from model #1

velocity was placed in the 0–3-km layers near the southwest corner of the study area (Figure 5-7). This velocity model more closely approximates the velocity conditions which might be encountered in the YMR. The shallow −2-percent anomaly is used to represent alluvium in Crater Flat, high velocity rocks to the northwest are a simplified model of the velocity anomalies likely related to the Timber Mountain Caldera complex. The shallow, 2–3-km, −5-percent velocity block might represent a cooling basaltic dike complex, which has heated the rocks around it, a worst case model indeed. Again rays were traced through this synthetic anomaly model to create a synthetic travel-time-residual data set. Also random Gaussian noise was added to the data set as before.

The results of the inversion indicate that the position and 72 percent of the amplitude of the −5-percent anomaly was recovered, the position and on average more than 50 percent of the amplitude of the −2 percent anomalies were recovered, and the +1 percent anomalies were not recovered with confidence (Figure 5-8).

In conclusion, with the experimental setup as described, it appears possible to image in the study volume small, 1-km diameter P-wave velocity anomalies with velocity contrasts of about 4 percent or more, and larger, multi-kilometer diameter anomalies with velocity contrasts of about 2 percent or more. With station spacing decreased to 0.5 km, anomalies on the order of 0.5 km diameter could probably be imaged. Uncertainties in the raypath locations due to uncertainties in the exact 3D velocity structure may cause the results in a real experiment to be somewhat worse than these. The results of the synthetic NeHT tomography experiment indicate that shallow, small velocity anomalies in the YMR can be identified and mapped using this approach. Such an investigation provides insight into the velocity structure of the region that other geophysical methods cannot. In terms of volcanic hazard assessment, this type of tomographic survey could provide empirical evidence of high-temperature zones, such as those previously mapped in the Coso volcanic field, which may alter probability estimates of volcanic disruption of the candidate repository.

5.3 TELESEISMIC TOMOGRAPHY FOR TWO-DIMENSIONAL STRUCTURE IN THE CRUST AND UPPER MANTLE

The goal of this type of experiment would be to obtain an image of the crust and upper mantle velocity perturbation structure along a 2D cross section through a volcanic area with a minimum of cost. The sources for the study would be teleseismic earthquakes with magnitudes of 5.2 or greater. In one possible scenario given for illustration (Figure 5-9), 12 seismographs would be deployed in a 62-km-long linear array centered on the volcano of interest. The spacing between stations would be about 4 km near the volcano and would increase to about 7 km at the ends of the array. This spacing is based on the resolution possible given the wavelengths of the 1-s period waves in the upper crust (4 km wavelength) and lower crust (7 km wavelength). The seismometers used would have broadband frequency response and would record all three components of motion. With these instruments, P- and S-wave velocity (from relative travel times) and attenuation (from relative amplitudes) structure could be studied. Note that in the NeHT study described above, only P-wave velocity was studied. With the addition of S-wave velocity and P- and S-wave attenuation measurements, interpretations of the inversion results in terms of the characteristics of the geologic structure can be much more unique. The seismographs would have digital recording and would be set to record continuously with a sampling rate of about 20 samples/s. If the study area were in the western United States, the array would be oriented northwest-southeast to take advantage of the numerous large earthquakes that occur in the subduction zones in Central and South America and in the northern and western Pacific. The instruments would be deployed for at least six months in order to record a sufficient number of teleseisms. Results of the study would be a cross section

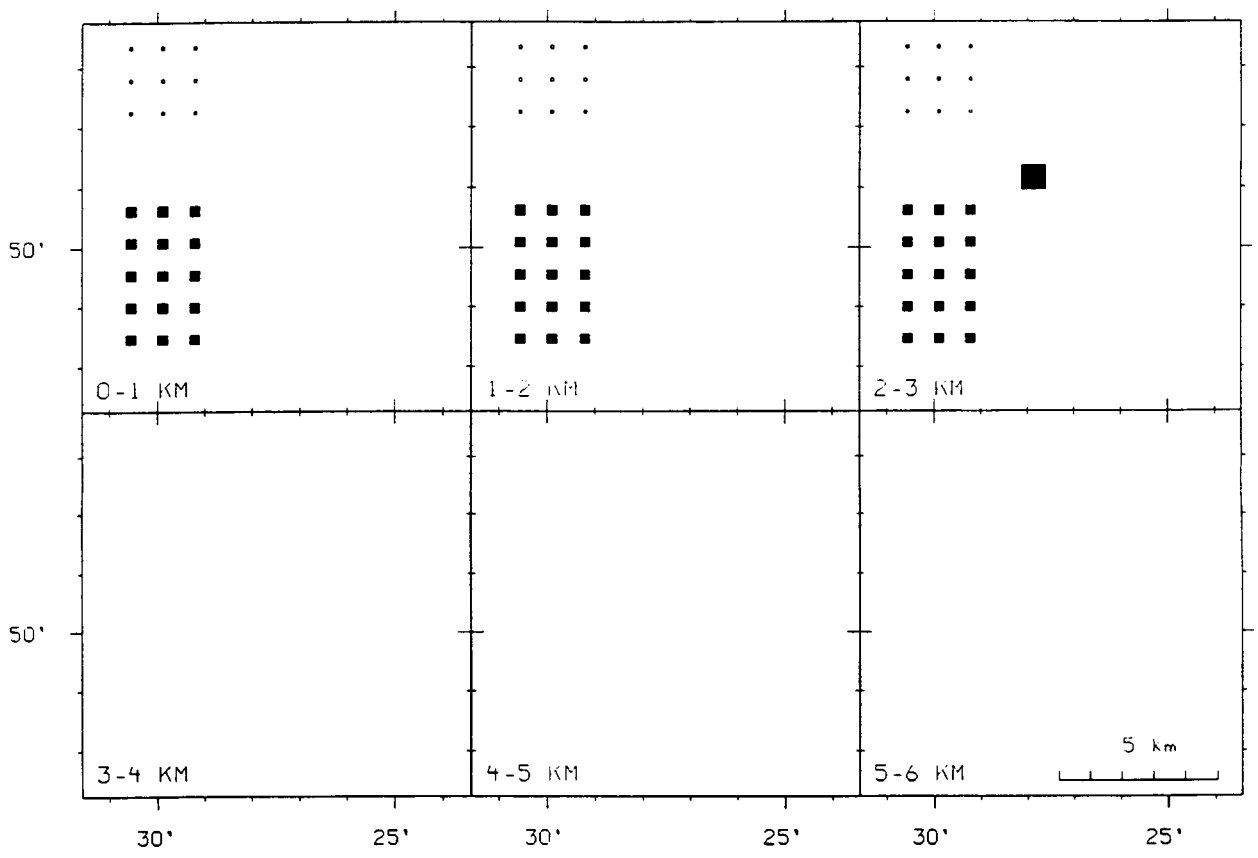

Figure 5-7. Synthetic P-wave velocity model #2. The anomaly symbol scale is as in Figure 5-5. The anomalies are −5, −2, and +1 percent, in the positions indicated.

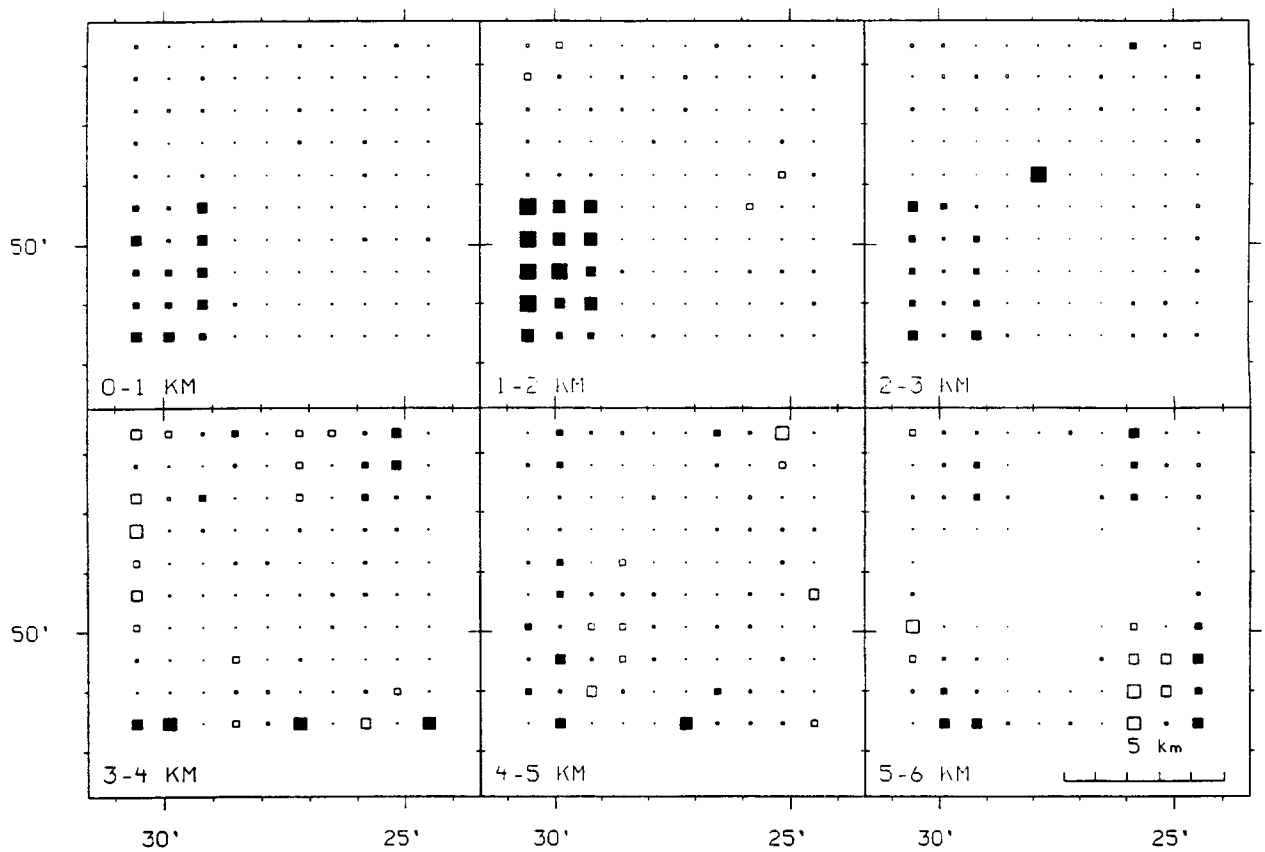

Figure 5-8. Results of inversion of synthetic travel-time delay data from model #2

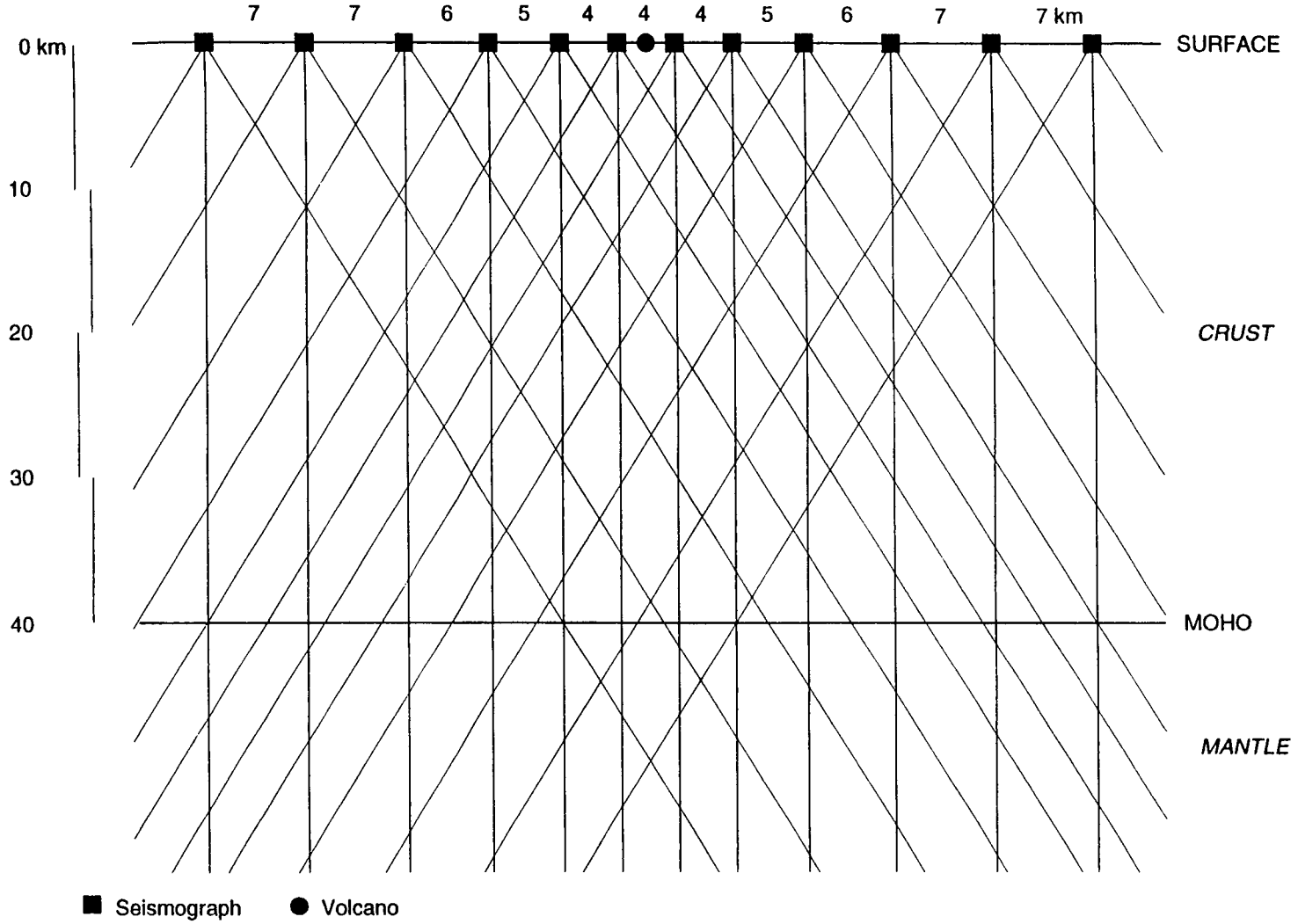

Figure 5-9. Experimental setup for 2D teleseismic tomography study

of the velocity and attenuation structure in the crust and upper mantle beneath the volcano of interest. The feasibility and utility of such a study was demonstrated at the Valles Caldera, New Mexico, by Roberts et al. (1991).

This type of tomography experiment would be useful for identifying slow velocity zones associated with the feeder systems of individual cones or cinder cone clusters. For example, application of the survey to San Francisco volcanic field, Arizona, would provide a sense of the duration and structure of thermal anomalies associated with basaltic volcanism, as Sunset Crater formed approximately 1,000 ybp. Tomographic data of this kind would provide powerful empirical constraints on probability models based on spatial and temporal distributions of cinder cones.

5.4 IMAGING A DIKE COMPLEX AND THE INTRUSION-TO-EXTRUSION RATIO

The goal of this type of experiment would be to obtain a 2D cross section of velocity structure in the upper few kilometers of the sedimentary basin beneath a cinder cone, in particular estimating the subsurface volume of dikes. The experiment takes advantage of the velocity contrast between the intrusive basaltic rock and the unconsolidated sediments in the basin. Seismic waves will travel faster through the intrusive rock, and the total travel time increase may be detected with a seismic refraction experiment. Such an experiment, while simple in design, may yield excellent estimates of the area of rock disrupted by intrusions related to the formation of cinder cones.

A conceptual seismic refraction experiment for determining dike intrusive percent is illustrated in Figure 5-10(a). A linear seismograph array is deployed centered on a basaltic cinder cone in an alluvial basin, and an explosion source is located at one end of the array. This is a classic seismic refraction geometry. For illustration, we show a station spacing of 0.5 km and a total line length of 5 km; the spacing and length may be longer or shorter depending on the spatial resolution and the depth of penetration required.

Compressional waves from the explosion source will travel to the seismographs through the sediment and intrusive that is present in the upper few kilometers of the basin. The waves that have traveled in part through intrusive will have traveled faster overall than the waves that traveled only through sediment. Therefore, the waves that have traveled in part through intrusive will have an arrival time that is earlier than expected for travel through only sediment. This is illustrated schematically in the travel-time curve [Figure 5-10(b)]. When the compressional wave arrival time at each seismograph is plotted against distance from the shot, the increase in arrival time for the faster intrusion-crossing rays is evident, and the value of the arrival-time difference, Δt, can be measured from the plot.

The amount of Δt observed is related to the volume of dike within the sediment if the velocities in the different rock types are known. These seismic velocities are known quite well from previous seismic and laboratory studies (Press, 1966). The seismic velocities in the basin sediment and basalt intrusive increase from about 1.5 and 5.9 km/s, respectively, in the upper few hundred meters to about 4.0 and 6.4 km/s, respectively, at 3-km depth (Figure 5-11). The velocities in the rocks increase with depth due to the closure of cracks and pore spaces from overburden pressure. The velocity contrast between the sediment and intrusive, therefore, decreases with increasing depth. Based on the velocities shown in Figure 5-10(b), we can calculate the value of Δt that will occur for a ray traversing a region of dike intrusion at some depth in the sedimentary basin. The Δt will depend on the volume of dike and

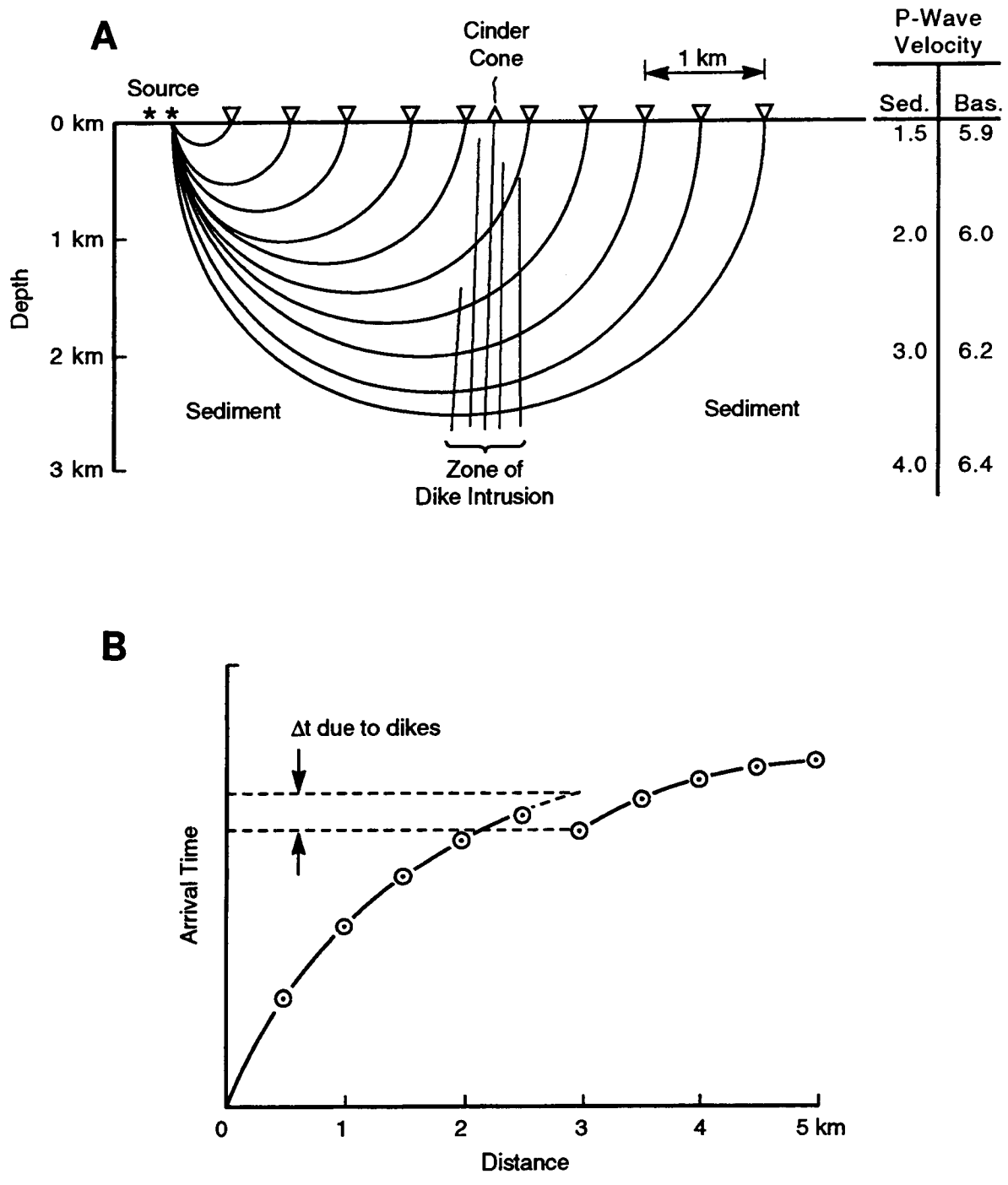

Figure 5-10. (a) Cross section illustrating conceptual experiment with linear seismic array to determine intrusion/extrusion beneath basaltic cinder cone. (b) Schematic traveltime curve.

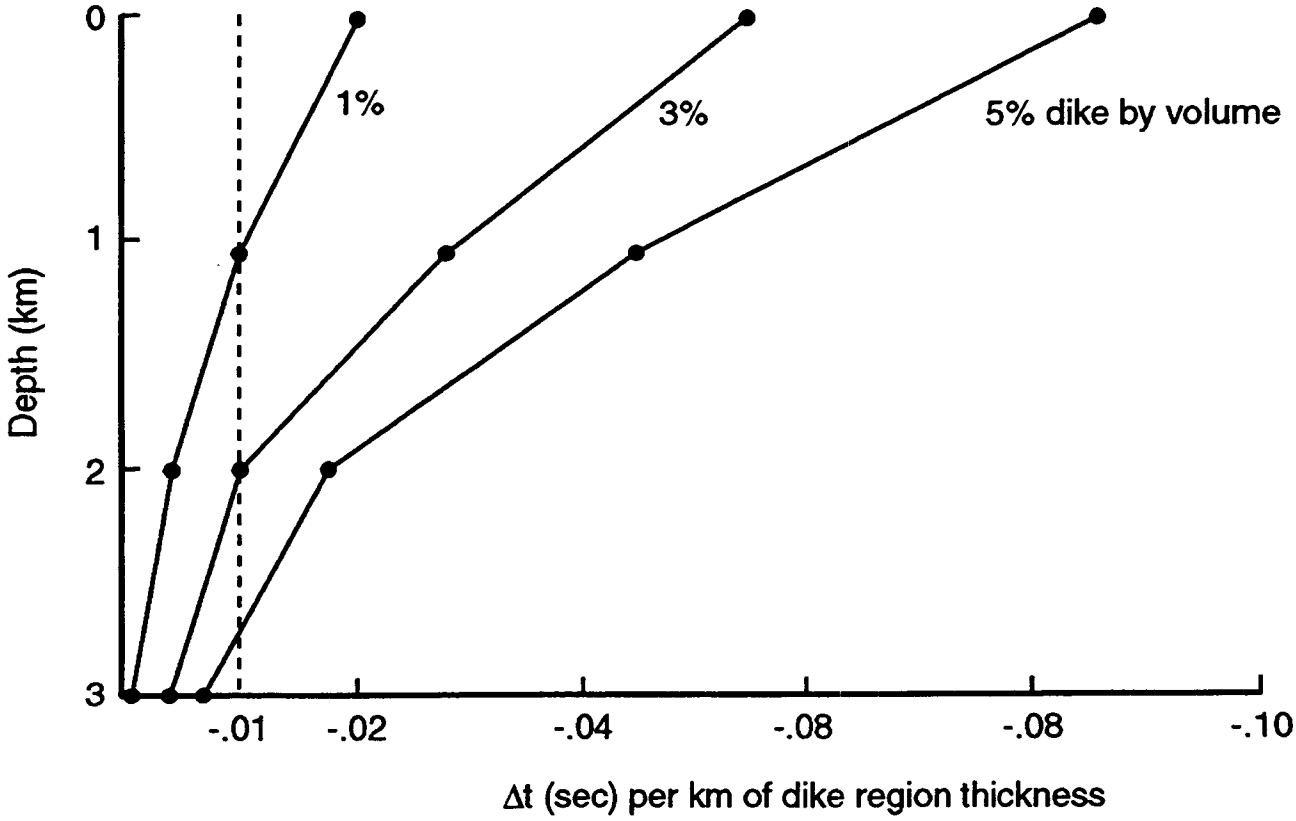

Figure 5-11. Graph illustrating traveltime decrease experienced by a ray that passes through a region of intrusives as a function of depth from the ground surface.

the depth at which the dike region was traversed. Plotted in Figure 5-11 are the Δt-depth curves for 1-km thick intrusion regions with dike volumes of 1, 3, and 5 percent. That is, dikes compose 1, 3, or 5 percent of the total rock mass in the intrusion region. These percentages are based on field observations of exhumed dike fields. Also plotted in Figure 5-11 is a dotted line at -0.01 s; this is about the minimum Δt measurable from the refraction records. The plot shows then that in the upper 1 km of the basin dike volumes as small as 1 percent may be discerned from the seismic data. As depth increases the minimum dike volume discernible increases. This plot illustrates the expected ability to image dike volume with the seismic refraction experiment.

The dikes would not have to be all vertical as shown in Figure 5-10 in order for the experiment to work. As long as the intrusions occurred within a restricted lateral zone beneath the cinder cone, the seismic waves would detect the bulk volume of intrusive material at any given depth.

Only one array deployment is needed to perform the experiment; however data from multiple arrays in different locations would increase the reliability of the interpretations, for instance, if two linear arrays were deployed, one across the cinder cone and one some distance away. The cross-cinder-cone line would show velocities through both sediment and intrusive, while the other line would show the velocities through purely sedimentary basin material. The second line would serve as a comparison to the

6 REFERENCES FOR SEISMIC TOMOGRAPHY

Achauer, U., L. Greene, J.R. Evans, and H.M. Iyer. 1986. Nature of magma chamber underlying the Mono Craters area, eastern California, as determined from teleseismic travel time residuals. *Journal of Geophysical Research* 91: 13,813–13,891.

Achauer, U., J.R. Evans, and D.A. Stauber. 1988. High-resolution seismic tomography of compressional wave velocity structure at Newberry volcano, Oregon Cascade Range. *Journal of Geophysical Research* 93: 10,135–10,147.

Aki, K., and W.H.K. Lee. 1976. Determination of three-dimensional velocity anomalies under a seismic array using first P arrival times from local earthquakes: 1. A homogeneous initial model. *Journal of Geophysical Research* 81: 4,381–4,399.

Aki, K., A. Christoffersson, and E.S. Husebye. 1977. Determination of the three-dimensional seismic structure of the lithosphere. *Journal of Geophysical Research* 82: 237–296.

Anderson, D.L., A. Ben-Menahem, and C.B. Archambeau. 1965. Attenuation of seismic energy in the upper mantle. *Journal of Geophysical Research* 70: 1,441–1,448.

Aster, R.C., and R.P. Meyer. 1988. Three-dimensional velocity structure and hypocenter distribution in the Campi Flegrei caldera, Italy. *Tectonophysics* 149: 195–218.

Bacon, C.R., W.A. Duffield, and K. Nakamura. 1980. Distribution of Quaternary rhyolite domes of the Coso Range, California: Implications for extent of the geothermal anomaly. *Journal of Geophysical Research* 85: 2,425–2,433.

Benz, H.M., and R.B. Smith. 1984. Simultaneous inversion for lateral velocity variations and hypocenters in the Yellowstone region using earthquake and refraction data. *Journal of Geophysical Research* 89: 1,208–1,220.

Burkhardt, H., J. Paffenholz, and R. Schutt. 1986. Measurements of Q on natural rock samples in different frequency ranges, in Absorption of Seismic Waves. H. Burkhardt, J. Paffenholz, and R. Schutt eds. *German Society for Petroleum Sciences and Coal Chemistry* Project 254, Hamburg: 203–238.

Chatterjee, S.N., A.M. Pitt, and H.M. Iyer. 1985. Vp/Vs ratios in the Yellowstone National Park region, Wyoming. *Journal of Volcanology Geothermal Research* 26: 213–230.

Clark, V.A., B.R. Tittmann, and T.W. Spencer. 1980. Effect of volatiles on attenuation (Q-1) and velocity in sedimentary rocks. *Journal of Geophysical Research* 85: 5,190–5,198.

Clawson, S.R., R.B. Smith, and H.M. Benz. 1989. P-wave attenuation of the Yellowstone Caldera from three-dimensional inversion of spectral decay using explosion source seismic data. *Journal of Geophysical Research* 94: 7,205–7,222.

Dawson, P.B., H.R. Evans, and H.M. Iyer. 1990. Teleseismic tomography of the compressional wave velocity structure beneath the Long Valley region, California. *Journal of Geophysical Research* 95: 11,021–11,050.

Dines, K.A., and R.J. Lytle. 1979. Computerized geophysical tomography. *Proceedings Institute of Electrical and Electronic Engineers* 67: 1,065–1,073.

Duffield, W.A., C.R. Bacon, and G.B. Dalrymple. 1980. Late Cenozoic volcanism, geochronology, and structure of the Coso Range, Inyo County, California. *Journal of Geophysical Research* 85: 2,381–2,404.

Eberhardt-Phillips, D. 1986. Three-dimensional velocity structure in northern California Coast Ranges from inversion of local earthquake arrival times. *Bulletin of the Seismological Society of America* 76: 1,025–1,052.

Ellsworth, W.L. 1977. *Three-Dimensional Structure of the Crust and Upper Mantle Beneath the Island of Hawaii*. Ph.D. Thesis. Boston, MA: Massachusetts Institute of Technology: 377.

Ellsworth, W.L., and R.Y. Koyanagi. 1977. Three-dimensional crust and mantle structure of Kilauea volcano, Hawaii. *Journal of Geophysical Research*: 82.

Evans, J.R., and M. Smith, III. 1992. Teleseismic tomography of the Yucca Mountain region: Volcanism and tectonism. *Proceedings of the Third International High Level Radioactive Waste Management Conference*: La Grange, IL: Amercian Nuclear Society 2: 2,371–2,380.

Evans, J.R., and J.J. Zucca. 1988. Active high-resolution seismic tomography of compressional wave velocity and attenuation structure at Medicine Lake volcano, northern California Cascade Range. *Journal of Geophysical Research* 93: 15,016–15,036.

Fawcett, J.A., and R.W. Clayton. 1984. Tomographic reconstruction of velocity anomalies. *Bulletin of the Seismological Society of America* 74: 2,201–2,219.

Ferrucci, F., and A. Hirn. 1985. Differential attenuation of seismic waves at a dense array: A marker of the Travale field from sources at regional distances. *Geothermics* 14: 723–730.

Foley, J.E., M.N. Toksoz, and F. Batini. 1992. Inversion of teleseismic travel time residuals for velocity structure in the Larderello geothermal field, Italy. *Geophysical Research Letters* 19: 5–8.

Gilbert, P.F.C. 1972. Iterative methods for three-dimensional reconstructions of an object from projections. *Journal of Theoretical Biology* 36: 105–117.

Herman, G.T., A. Lent, and S.W. Rowland. 1973. ART: Mathematics and Applications. *Journal of Theoretical Biology* 42: 1–32.

Herrin, E. 1968. Seismological tables of P-phases. *Bulletin of the Seismological Society of America* 58: 1,193–1,241.

Hirn, A., and F. Ferrucci. 1985. P and S arrival time anomalies at a dense array: marker of the Travale field. *Geothermics* 14: 713–722.

Hirn, A., M. Sachpazi, and A. Nercessian. 1989. Elements for a model of the geothermal field of Milos from seismological data. *Geothermics* 18: 579–595.

Ho-Liu, P.H.-Y. 1988. I. *Attenuation Tomography: II. Modeling Regional Love Waves: Imperial Valley to Pasadena*. Ph.D. Dissertation. Pasadena, CA: California Institute of Technology.

Ho-Liu, P., H. Kanamori, and R.W. Clayton. 1988. Applications of attenuation tomography to Imperial Valley and Coso-Indian Wells region, Southern California. *Journal of Geophysical Research* 93: 10,501–10,520.

Ho-Liu, P., J.-P. Montagner, and H. Kanamori. 1989. Comparison of iterative back-projection inversion and generalized inversion without blocks: Case studies in attenuation tomography. *Journal of Geophysical Research* 97: 19–29.

Hoffman, L.R., and W.D. Mooney. 1984. *A Seismic Study of Yucca Mountain and Vicinity, Southern Nevada: Data Report and Preliminary Results*. Open-File Report 83–588: Reston, VA: U.S. Geological Survey.

Humphreys, E.D., and R.W. Clayton. 1988. Adaptation of tomographic reconstruction to seismic travel time problems. *Journal of Geophysical Research* 93: 1,073–1,085.

Humphreys, E.D., and R.W. Clayton. 1990. Tomographic image of the southern California mantle, *Journal of Geophysical Research* 95: 19,725–19,746.

Humphreys, E.D., R.W. Clayton, and B.H. Hager. 1984. A tomographic image of mantle structure beneath southern California. *Geophysical Research Letters* 11: 625–627.

Ito, K. 1990. Effects of H_2O on elastic wave velocities in ultrabasic rocks at 900 °C under 1 GPa. *Physics of the Earth and Planetary Interiors* 61: 260–268.

Ito, H., J. DeVilbiss, and A. Nur. 1979. Compressional and shear waves in saturated rock during water-steam transition. *Journal of Geophysical Research* 84: 4,731–4,735.

Ivansson, S. 1983. Remark on an earlier proposed iterative tomographic algorithm. *Geophysical Journal of the Royal Astronomical Society* 75: 855.

Iyer, H.M. 1984. Geophysical evidence for the locations, shapes, and sizes and internal structures of magma chambers beneath regions of Quaternary volcanism. Phil. *Transactions of the Royal Society of London Series* A 310: 473–510.

Iyer, H.M. 1988. Seismological detection and delineation of magma chambers beneath interplate volcanic centers in western U.S.A., *Modeling of Volcanic Processes*. C. King and R. Scarpa eds. Amsterdam, The Netherlands: Friedr. Vieweg and Sohn.

Iyer, H.M., J.R. Evans, G. Zandt, R.M. Stewart, J.M. Coakley, and J.N. Roloff. 1981. A deep low-velocity body under the Yellowstone caldera, Wyoming: Delineation using teleseismic P-wave residuals and tectonic interpretation: Summary. *Geological Society of America Bulletin* 92: 792–798.

Jones, T., and A. Nur. 1983. Velocity and attenuation in sandstone at elevated temperatures and pressures. *Geophysical Research Letters* 10: 140–143.

Kampfmann, W., and H. Berckhemer. 1985. High temperature experiments on the elastic and anelastic behavior of magmatic rocks. *Physics of the Earth and Planetary Interiors* 40: 223–247.

Kissling, E. 1988. Geotomography with local earthquake data. *Reviews of Geophysics* 26: 659–698.

Lees, J.M. 1992. The magma system of Mount St. Helens: non-linear high-resolution P-wave tomography. *Journal of Volcanology and Geothermal Research* 53: 103–116.

Lees, J.M., and R.S. Crosson. 1989. Tomographic inversion for three-dimensional velocity structure at Mount St. Helens using earthquake data. *Journal of Geophysical Research* 94: 5,716–5,728.

Levenberg, K. 1944. A method for the solution of certain non-linear problems in least squares. *Quarterly of Applied Mathematics* 2: 164–168.

Majer, E.L., and T.V. McEvilly. 1979. Seismological investigations at The Geysers geothermal field. *Geophysics* 44: 246–269.

Marquardt, D.W. 1963. An algorithm for least-squares estimation of non-linear parameters. *Journal of Society of Industrial Applied Mathematics* 11: 431–441.

Mavko, G.M. 1980. Velocity and attenuation in partially molten rocks. *Journal Geophysical Research* 85: 5,173–5,189.

Mavko, G.M., and A. Nur. 1979. Wave attenuation in partially saturated rocks. *Geophysics* 44: 161–178.

Mizutani, H., and H. Kanamori. 1964. Variation of elastic wave velocity and attenuation property near the melting temperature. *Journal of Physical Earth* 12: 43–49.

Moos, D., and M.D. Zoback. 1983. *In situ* studies of velocity in fractured crystalline rocks. *Journal of Geophysical Research* 88: 2,345–2.358.

Murase, T., and A.R. McBirney. 1973. Properties of some common igneous rocks and their melts at high temperatures. *Geological Society of America Bulletin* 84: 3,563–3,592.

Murphy, W.F. 1983. Effect of partial water saturation on attenuation in Massilon sandstone and Vycor porous glass. *Journal of the Acoustical Society of America* 71: 1,458–1,468.

Nercessian, A., A. Hirn, and A. Tarantola. 1984. Three-dimensional seismic transmission prospecting of the Mont Dore volcano, France. *Geophysical Journal of the Royal Astronomical Society* 76: 307–315.

Nicholson, C., and D.W. Simpson. 1985. Changes in Vp/Vs with depth: Implications for appropriate velocity models, improved earthquake locations, and material properties of the upper crust. *Bulletin of the Seismological Society of America* 75: 1,105–1,123.

Nixon, L.D. 1992. *Three-Dimensional S-Wave Attenuation Structure of Long Valley Caldera, California, From Three-Component S-to-P Amplitude Ratio Data*. M.S. Thesis. Pheonix, AZ: Arizona State University.

Nur, A., and G. Simmons. 1969. The effect of saturation on velocity in low porosity rocks. *Earth Planet Science* 7: 183–193.

Ochmann, N., D. Hollnack, and J. Wohlenberg. 1989. Seismological exploration of the Milos geothermal reservoir. Greece: *Geothermics* 18: 563–577.

O'Connell, R.J., and B. Budiansky. 1974. Seismic velocities in dry and saturated cracked solids. *Journal of Geophysical Research* 79: 5,412–5,426.

O'Connell, R.J., and B. Budiansky. 1977. Viscoelastic properties of fluid-saturated cracked solids. *Journal of Geophysical Research* 82: 5,719–5,735.

Oppenheimer, D.H., and K.E. Herkenhoff. 1981. Velocity-density properties of the lithosphere from three-dimensional modeling at The Geysers-Clear Lake region, California. *Journal of Geophysical Research* 86: 6,057–6,065.

Paige, C.C., and M.A. Saunders. 1982. LSQR: An algorithm for sparse linear equations and sparse least squares. *Transactions in Mathematical Software* 8: 43–71.

Pavlis, G.L., and J.R. Booker. 1980. The mixed discrete-continuous inverse problem: Application to the simultaneous determination of earthquake hypocenters and velocity structure. *Journal of Geophysical Research* 85: 4,801–4,810.

Pearson, C.F., M.C. Fehler, and J.N. Albright. 1983. Changes in compressional and shear wave velocities and dynamic moduli during operation of a hot dry rock geothermal system. *Journal of Geophysical Research* 88: 3,468–3,475.

Ponko, S.C., and C.O. Sanders. 1994. Inversion for P- and S-wave attenuation structure, Long Valley caldera, California. *Journal of Geophysical Research* 99: 2,619–2,635.

Press, F. 1966. Seismic velocities. Handbook of physical constants. S.P. Clark Jr., ed. *Geological Society of America Memoir 97*: 97–173.

Reasenberg, P., W. Ellsworth, and A. Walter. 1980. Teleseismic evidence for a low-velocity body under the Coso geothermal area. *Journal of Geophysical Research* 85: 2,471–2,483.

Roberts, P.M., K. Aki, and M.C. Fehler. 1991. A low-velocity zone in the basement beneath the Valles Caldera, New Mexico. *Journal of Geophysical Research* 96: 21,583–21,596.

Robinson, R., and H.M. Iyer. 1981. Delineation of a low-velocity body under the Roosevelt Hot Springs geothermal area, Utah, using teleseismic P-wave data. *Geophysics* 46: 1,456–1,466.

Roecker, S.W. 1982. Velocity structure of the Pamir-Hindu Kush region: Possible evidence of a subducted crust. *Journal of Geophysical Research* 87: 945–959.

Rowan, L.R., and R.W. Clayton. 1993. The three-dimensional structure of Kilauea volcano, Hawaii, from travel time tomography. *Journal of Geophysical Research* 98: 4,355–4,375.

Sanders, C.O. 1984. Location and configuration of magma bodies beneath Long Valley, California, determined from anomalous earthquake signals. *Journal of Geophysical Research* 89: 8,287–8,302.

Sanders, C.O. 1993. Reanalysis of S/P amplitude ratios for gross attenuation structure, Long Valley caldera, California. *Journal of Geophysical Research* 98: 22,069–22,080.

Sanders, C., P. Ho-Liu, D. Rinn, and H. Kanamori. 1988. Anomalous shear-wave attenuation in the shallow crust beneath the Coso volcanic region, California. *Journal of Geophysical Research* 93: 3,321–3,338.

Sato, H., and M.H. Manghnani. 1985. Ultrasonic measurements of VP and QP: Relaxation spectrum of complex modulus in basalt melts. *Physics of the Earth and Planetary Interiors* 41: 18–33.

Sato, H., and I.S. Sacks. 1989. Anelasticity and thermal structure of the oceanic upper mantle: Temperature calibration with heat flow data. *Journal of Geophysical Research* 94: 5,705–5,715.

Sato, H., I.S. Sacks, and T. Murase. 1989. The use of laboratory velocity data for estimating temperature and partial melt fraction in the low-velocity zone: Comparison with heat flow and electrical conductivity studies. *Journal of Geophysical Research* 94: 5,689–5,704.

Scherbaum, F. 1990. Combined inversion for the three-dimensional Q structure and source parameters using microearthquake spectra. *Journal of Geophysical Research* 95: 12,423–12,438.

Scherbaum, F., and M. Wyss. 1990. Distribution of attenuation in the Kaoiki, Hawaii, source volume estimated by inversion of P wave spectra. *Journal of Geophysical Research* 95: 12,439–12,448.

Schwartz, E.A. 1993. *Three-Dimensional Variations in the Compressional to Shear Wave Velocity Ratio for Long Valley Caldera, California*: M.S. Thesis. Pheonix, AZ: Arizona State University.

Solomon, S.C., and M.N. Toksoz. 1970. Lateral variation of attenuation of P and S waves beneath the United States. *Bulletin of the Seismological Society of America* 60: 819–838.

Spakman, W., and G. Nolet. 1988. Imaging algorithms, accuracy and resolution in delay time tomography. D. Reidel, N.J. Boston, G. Vlaar, M.J. Nolet, J.R. Wortel, and S.A.P.L. Cloetingh, eds. *Mathematical Geophysics*: 1,155–1,187.

Stauber, D.A. 1982. Two-dimensional compressional wave velocity structure under San Francisco volcanic field, Arizona, from teleseismic P-residual measurements. *Journal of Geophysical Research* 87: 5,451–5,459.

Stauber, D.A., S.M. Green, and H.M. Iyer. 1988. Three-dimensional P velocity structure of the crust below Newberry Volcano, Oregon. *Journal of Geophysical Research* 93: 10,095–10,107.

Steeples, D.W., and H.M. Iyer. 1976. Low-velocity zone under Long Valley as determined from teleseismic events. *Journal of Geophysical Research* 81: 849–860.

Stocker, R.L., and R.B. Gordon. 1975. Velocity and internal friction in partial melts. *Journal of Geophysical Research* 80: 4,828–4,836.

Tarantola, A., and A. Nercessian 1984. Three-dimensional inversion without blocks. *Geophysical Journal of the Royal Astronomical Society* 76: 299–306.

Teng, T.-L. 1968. Attenuation of body waves and the Q structure of the mantle. *Journal of Geophysical Research* 73: 2,195–2,208.

Thurber, C.H. 1983. Earth structure and earthquake locations in the Coyote Lake area, central California. *Journal of Geophysical Research* 88: 8,226–8,236.

Thurber, C.H. 1984. Seismic detection of the summit magma complex of Kilauea volcano, Hawaii. *Science* 233: 165–167.

Thurber, C.H., and S.R. Atre. 1993. Three-dimensional Vp/Vs variations along the Loma Prieta rupture zone. *Bulletin of the Seismological Society of America* 83: 717–736.

Toksoz, M.N., C.H. Cheng, and T. Aytekin. 1976. Velocities of seismic waves in porous rock. *Geophysics* 41: 621–645.

Toomey, D.R., G.M. Purdy, S.C. Solomon, and W.S.D. Wilcock. 1990. The three-dimensional seismic velocity structure of the East Pacific Rise near latitude 9° 30 N. *Nature* 347: 639–645.

Um, J., and C. Thurber. 1987. A fast algorithm for two-point seismic ray tracing. *Bulletin of the Seismological Society of America* 77: 972–986.

Umino, N., and A. Hasegawa. 1984. Three-dimensional Q_s structure in the northeastern Japan arc. *Journal of the Seismological Society of Japan* 31: 217–228.

Van der Sluis, A., and H.A. van der Vorst. 1987. Numerical solution of large, sparse linear algebraic systems arising from tomographic problems. D. Reidel, Boston, and G. Nolet, ed. *Seismic Tomography*: 49–83.

Walck, M.C. 1988. Three-dimensional V_p/V_s variations for the Coso region California. *Journal of Geophysical Research* 93: 2,047–2,052.

Walck, M.C., and R.W. Clayton. 1987. P wave velocity variations in the Coso region, California, derived from local earthquake travel times. *Journal of Geophysical Research* 92: 393–406.

Walsh, J.B. 1969. New analysis of attenuation in partially melted rock. *Journal of Geophysical Research* 74: 4,333–4,337.

Ward, R.W., and C.-Y. Young. 1980. Mapping seismic attenuation within geothermal systems using teleseisms with application to the Geysers-Clear Lake region. *Journal of Geophysical Research* 85: 5227–5236.

Winkler, K., and A. Nur. 1979. Pore fluids and seismic attenuation in rocks. *Geophysical Research Letters* 6: 1–4.

Young, C.-H., and R.W. Ward. 1980. Three-dimensional Q-1 model of the Coso Hot Springs known geothermal resource area. *Journal of Geophysical Research* 85: 2,459–2,470.

PART II: MAGNETIC METHODS

7 OVERVIEW OF MAGNETIC METHODS

7.1 INTRODUCTION

Of all geophysical methods used to date in site characterization in the YMR, aeromagnetic methods, coupled with ground magnetic surveys, have been used most frequently and with greatest success to search for buried volcanic features (Oliver et al., 1990; Ponce et al., 1992; Langenheim et al., 1993). These studies use aeromagnetic maps compiled and discussed by Kane and Bracken (1983), Kane et al. (1981), Bath and Jahren (1984), Langenheim et al. (1991), and others, supplemented in some instances with ground magnetic data, for a variety of site characterization tasks. The rock magnetic properties of the Paintbrush Tuff and related lithologies in the YMR have been discussed by Scott and Rosenbaum (1986), Sclinger et al. (1988), Rosenbaum (1986), and others. Cumulatively, these studies represent a comprehensive effort to identify and evaluate major geophysical trends and anomalies in the region.

One of these studies (Langenheim et al., 1993) focused on the relationship between aeromagnetic anomalies and buried volcanic centers and/or intrusives in Amargosa Valley, south of the YMR. Recognition of the Amargosa Valley magnetic anomalies and correlation of these anomalies with basaltic volcanism has been an important step in site characterization. These magnetic anomalies, two of which have been drilled and found to be related to basalts located at shallow depths, have been incorporated into models for the recurrence of volcanism in the YMR and the probability of volcanic disruption of the candidate repository (Crowe et al., 1993; Connor and Hill, 1993a). These magnetic surveys have been used to suggest that all major volcanic centers in the region have been identified (Crowe et al., 1993). Crowe et al. (1993, page 132) conclude that, based on aeromagnetic data "we have a relatively high degree of confidence that all significant sites of possible buried basalt have been identified in the Yucca Mountain area." The presence, or absence, of shallow intrusive features is less certain.

Because such emphasis has been placed on the application of magnetic methods to the identification of volcanic features, it is important to review the capabilities of magnetic methods with regard to identification and mapping of subsurface, either buried extrusive or intrusive, igneous features. The goal of the following sections is to review magnetic methods in geophysics and their application to volcanological problems in the YMR. Specific topics addressed include:

- Discussion of physical bases for magnetic methods and their application in geophysics
- A brief review of the application of ground magnetic and aeromagnetic surveys to investigations of selected volcanic areas
- A parametric study of the amplitude and wavelength of magnetic anomalies, with particular emphasis on expected magnetic anomalies produced by dikes in the Tiva Canyon Tuff and in alluvial valleys of the YMR
- An investigation of the impact of magnetized terrain on our ability to identify intrusive structures near basaltic cinder cones and lava flows

- Application of frequency-domain map enhancement techniques for the delineation of subtle magnetic anomalies in complex, noisy magnetic environments

The intent of this report is not to present new magnetic data nor to make new interpretations of magnetic anomalies in the YMR, but rather to explore the utility and limitations of magnetic methods and their application to basaltic volcanism in the YMR, including the identification of basaltic centers which lack subsurface expression and determination of intrusion geometry.

7.2 BACKGROUND

The geophysical literature is replete with examples of derivations of magnetic anomalies associated with basaltic dikes, application of various algorithms for calculating anomalies associated with dikes, and discussion of the use and limitations of forward and inverse approaches to modeling dike geometries (Bhattacharyya, 1964; Talwani, 1965; Talwani and Heirtzler, 1964; Rao et al., 1973; Plouff, 1975; Cady, 1980; Khurana et al., 1981; Ku and Sharp, 1983; Webring, 1985; Babu et al., 1986; Chenot and Debeglia, 1990). Relatively few examples of the application of ground magnetic surveys are found in the literature, nor are aeromagnetic studies of volcanic fields common (Flanigan et al., 1986; Flanigan and Long, 1987; Young and Lucas, 1988; Zeyen et al., 1991; Zoback et al., 1994). This arises because magnetic equations can be cast in relatively simple form for anomalies related to dikes. Nonetheless, measured magnetic anomalies related to dikes are often complex due to numerous factors, including variation in the magnetic contrast between dikes and the rocks they intrude, rotation or reversal of the magnetic polarization of dikes, topographic effects, and the influence of rapid variations in the magnetic properties of areas of high topographic relief (Grauch, 1985). The complexity of the measured magnetic anomalies in igneous terrains has prompted the development of numerous statistical and empirical map enhancement and interpretation techniques (Dean, 1958; Spector and Grant, 1970; Clarke, 1971; Bhattacharyya and Leu, 1975; Bhattacharyya and Chan, 1977). Of particular importance have been developments in the analysis and reduction of magnetic terrain effects (Grauch, 1985) and the integration of aeromagnetic data with other geophysical data, notably gravity data, through the application of Poisson's relation (Poisson, 1826; Kanasewich and Agnarwal, 1970; Botezatu and Calota, 1973; Gunn, 1975, Serpa and Cook, 1984; Young and Lucas, 1988; Chandler and Malek, 1991). Cross-correlation of aeromagnetic data with LandSat TM imagery and other remotely sensed data (Paterson and Reeves, 1985) and seismic data (Andrew et al., 1991), has been most successful where the goal of the study has been delineation of tectonic or volcanic features for the purpose of better understanding geologic processes, rather than simple characterization of geophysical anomalies.

7.2.1 Modeling Magnetic Anomalies

A method for the calculation of total magnetic field anomalies was developed for bodies of arbitrary geometry and magnetization by Talwani (1965). Talwani (1965) was the first to subdivide the equation for the magnetic field caused by a magnetic body into separate geometric and magnetic components in order to simplify the calculation. In the most general case, consider a 3D body in an

orthogonal coordinate system, x, y, z. The magnetic potential, Ω, at the origin due to a volume element within this 3D body is

$$\Omega = \frac{\mu \cdot \mathbf{R}}{R^3} \tag{7-1}$$

where μ is the magnetic moment of the volume element and $\mathbf{R}$ is a vector of length R, the distance from the origin of the coordinate system to the center of this volume element. Assuming that the intensity of magnetization, $\mathbf{J}$, within this element is uniform:

$$\mu = \mathbf{J}\Delta x \Delta y \Delta z \tag{7-2}$$

$$\Omega = \frac{J_x x + J_y y + J_z z}{R^3} \; \Delta x \; \Delta y \; \Delta z \tag{7-3}$$

Therefore the three components of magnetic intensity are

$$\Delta X = \int \int \int \; - \frac{\partial \Omega}{\partial x} \; dx \; dy \; dz \tag{7-4}$$

$$\Delta Y = \int \int \int \; - \frac{\partial \Omega}{\partial y} \; dx \; dy \; dz \tag{7-5}$$

$$\Delta Z = \int \int \int \; - \frac{\partial \Omega}{\partial z} \; dx \; dy \; dz \tag{7-6}$$

Substituting in Eq. 7-3, the expression for the components of magnetization becomes

$$\begin{bmatrix} \Delta X \\ \Delta Y \\ \Delta Z \end{bmatrix} = \begin{bmatrix} V_1 & V_2 & V_3 \\ V_2 & V_4 & V_5 \\ V_3 & V_5 & V_6 \end{bmatrix} \begin{bmatrix} J_x \\ J_y \\ J_z \end{bmatrix} \tag{7-7}$$

where

$$V_1 = \int_V \frac{3x^2 - R^2}{R^5} \, dx \, dy \, dz \tag{7-8}$$

$$V_2 = \int_V \frac{3xy}{R^5} \, dx \, dy \, dz \tag{7-9}$$

$$V_3 = \int_V \frac{3xz}{R^5} \, dx \, dy \, dz \tag{7-10}$$

$$V_4 = \int_V \frac{3y^2 - R^2}{R^5} \, dx \, dy \, dz \tag{7-11}$$

$$V_5 = \int_V \frac{3yz}{R^5} \, dx \, dy \, dz \tag{7-12}$$

$$V_6 = \int_V \frac{3z^2 - R^2}{R^5} \, dx \, dy \, dz \tag{7-13}$$

Talwani's approach is of great utility because the volume integrals V_1—V_6 can be calculated independently of the vector of magnetization (Talwani and Heirtzler, 1964; Talwani, 1965). Note that volume integrals, V_2, V_3, and V_5 produce asymmetry in the magnetic anomaly caused by the volume. This gives rise to the dipolar shape of magnetic anomalies (Plouff, 1975). Since Talwani's seminal papers, numerous investigators have proposed computationally efficient solutions to the volume integrals for specific, generally simplified, geometries (Bhattacharyya, 1964; Rao et al., 1973; Plouff, 1975; Cady, 1980; Babu et al., 1986; Rao and Babu, 1991, 1993). Many of these solutions can be directly applied to anomalies related to dikes, because dike geometry is simple: dikes can often be approximated as long, vertically-sided prisms, or dipping prisms. Plouff (1976) provides a thorough derivation of the volume integrals from simple geometric shapes. Rao and Babu (1991) offer a simple and computationally efficient solution for the volume integrals V_1—V_6 for vertically-sided prisms. Their algorithm is used for the majority of calculations presented here.

The intensity of magnetization $\mathbf{J}_{tot}$, is the sum of the intensity induced magnetization, $\mathbf{J}_i$, and remanent magnetization, $\mathbf{J}_r$. The induced portion of the field is the product of the Earth's magnetic and the rock magnetic susceptibility, which depends largely on the percentage, mineralogy, and grainsize of magnetic minerals in the rock. The intensity of induced magnetization is

$$\mathbf{J}_i = k\mathbf{H} \tag{7-14}$$

where k is the rock magnetic susceptibility and $\mathbf{H}$ is the Earth's magnetic field. As the name implies, remanent magnetization is a component of $\mathbf{J}_{tot}$ that does not depend on the current strength or orientation of the Earth's magnetic field, but rather on past field orientation, usually the field present at the time the rock formed. Various types of remanent magnetization occur, collectively termed normal remanent magnetization. In basalts, the most important form of normal remanent magnetization is thermo-remanent magnetization, acquired at the time the basalt cooled below the Curie blocking temperatures for the magnetic grains within the rock. As these blocking temperatures are between 600 and 350 °C for most magnetic minerals in basalts, the remanent magnetization vector recorded the orientation of the Earth's magnetic field at the time the basalt solidified. Remanent magnetization in basalts is often the most important component of $\mathbf{J}_{tot}$ because of the high thermo-remanent magnetization carried by magnetic minerals in basalts (Hood, 1964; Lindsey et al., 1966). Subsequent movement, such as rafting and rotation of the flow or fault block rotation, will also rotate the vector of remanent magnetization, often producing complex magnetic anomalies. Numerous investigators have suggested analytical, empirical, and statistical approaches to the characterization and modeling of magnetic anomalies produced by arbitrarily oriented vectors of remanent magnetization (Am, 1972; Grant, 1972; Shurbet et al., 1976; Arkani-Hamed and Celetti, 1989; Roest and Pilkington, 1993). By definition, the components of the total vector of magnetization $\mathbf{J}_{tot}$, (Plouff, 1975) are:

$$J_x = k\mathbf{H}l + \mathbf{J}_r L \tag{7-15}$$

$$J_y = k\mathbf{H}m + \mathbf{J}_r M \tag{7-16}$$

$$J_z = k\mathbf{H}n + \mathbf{J}_r N \tag{7-17}$$

where k and $\mathbf{H}$ are defined as before, $\mathbf{J}_r$ is the intensity of remanent magnetization $l, m,$ and $n,$ and $L, M,$ and N are direction cosine terms for the induced and remanent components of magnetization, respectively:

$$l = \cos I_o \cos D_o \tag{7-18}$$

$$m = \cos I_o \sin D_o \tag{7-19}$$

$$n = \sin I_o \tag{7-20}$$

where I_o is the inclination of the Earth's field, measured positive downward, and D_o is the declination of the Earth's field, measured clockwise from N. Similarly:

$$L = \cos I_r \cos D_r \tag{7-21}$$

$$M = \cos I_r \sin D_r \tag{7-22}$$

$$N = \sin I_r \tag{7-23}$$

where I_r and D_r are the inclination and declination of $\mathbf{J}_r$, respectively. Normally, the magnetic anomaly due to a magnetized body is small compared to the Earth's field strength. The total magnetic anomaly measured by a magnetometer at a field point is given by:

$$T = \sqrt{\left[(lH + \Delta X)^2 + (mH + \Delta Y)^2 + (nH + \Delta Z)^2\right]} - H \tag{7-24}$$

As long as the magnetic field anomaly is small compared with the Earth's magnetic field strength, this equation becomes:

$$T = (l\Delta X + m\Delta Y + n\Delta Z) \tag{7-25}$$

The total magnetic field anomaly can then be calculated given some knowledge of the magnetic properties of the rock and the geometry of geologic units that can be assumed to have reasonably uniform magnetic properties. A basic limitation of all potential field methods, including magnetics, is that the inference of the geometry and properties of the causative body is an underdetermined problem. Assumptions must be made about the properties of the geologic structure producing the anomaly, such as its geometry or susceptibility, in order to make inferences from magnetic data about its other properties. In the absence of other data, for example from boreholes or rock magnetic studies, an infinite set of solutions may be invoked to explain a given magnetic anomaly. Bearing this in mind, a variety of modeling approaches have been developed to interpret magnetic anomalies. Forward modeling (Bhattacharyya, 1964; Bruckshaw and Kunaratam, 1963; Rao et al., 1973; Babu et al., 1986) or inversion techniques (Khurana et al., 1981; Ku and Sharp, 1983; Webring, 1985; Chenot and Debeglia, 1990; Xia and Sprowl, 1992; Rao and Babu, 1993) are most commonly used. Other methods have been developed to determine the properties of a dike (e.g., its vector of magnetization, depth, and dip), using the magnetic signature of the geologic body. These methods are appropriate when it is known with some certainty that the causative body has a simple dike shape. Most of these methods rely on analysis of horizontal and vertical gradients in the total magnetic field (Babu et al., 1982; Kunaratnam, 1982; Pal, 1985; Marobhe, 1990).

7.2.2 Note on Magnetic Units

Magnetic units are sometimes confusing, primarily because two nomenclature systems are currently in use. The system most widely used, especially in rock magnetic studies, is the International System (SI). The Gaussian (also known as the cgs or emu) system is also widely used, particularly in the older geophysical literature (Payne, 1981). Unfortunately, units are occasionally used from both systems interchangeably. The two systems use different basic quantities on which the magnetic measurements and parameters are built. In the Gaussian system there are three basic quantities. These are mass (g), length (cm) and time (s). The magnetic permeability, μ_o, of space is taken as unity and is dimensionless in the Gaussian system. This is important because in the Gaussian system:

$$\mathbf{B} = \mu_o \mathbf{H} = \mathbf{H} \qquad (7\text{-}26)$$

where **B** is magnetic induction and **H** is magnetic field strength. In the SI system there are four basic quantities: mass (kg), length (m), time (s), and electrical current (A, amperes). In the SI system, μ_o equals $4\pi \times 10^{-7}$, so **B** does not equal **H**. Since a small loop of wire carrying an electrical current produces the same magnetic field as a dipole, it is possible to define the magnetic field in terms of these four units. SI units will be used throughout this report because it is currently the preferred system.

Table 7-1 summarizes the conversion between SI and Gaussian units for the most common terms used in geophysical studies. Normally, the total magnetic field is calculated and measured in aeromagnetic and ground magnetic surveys. The unit for the total field anomaly is a Tesla ($A^{-2}kg\ s^{-2}$). Because total field anomalies are small compared to a Tesla, total field anomalies in geophysics are normally reported in nanoTeslas (nT). One nT is equivalent to one gamma (γ) in Gaussian units.

7.2.3 Magnetic Properties of Basalts

Basalts typically exhibit both high magnetic susceptibilities and high remanent magnetizations. This means that by volume, dikes and buried basaltic lava flows and cones are easily detected using a magnetic survey. Susceptibilities for effusive igneous rocks have been summarized by Dobrin and Savit (1988). Susceptibilities vary from 5.2×10^{-4} (SI) to 1.2×10^{-1} (SI) in 78 samples, with a mean of 3.3×10^{-2} (SI). This agrees well with the compilation of Tarling (1983), based on which he finds that susceptibilities are lognormally distributed in igneous rocks with a geometric mean of 2.5×10^{-2} (SI). Lindsey et al. (1966) found that approximately 80 percent of basalts have susceptibilities between 1.5×10^{-3} (SI) and 5.0×10^{-2} (SI). These magnetic susceptibilities are about three orders of magnitude greater than those measured for sediments. Although silicic igneous rocks, including welded and nonwelded tuffs, often have much lower magnetizations than basalts, there is considerable overlap between these groups. Under some circumstances sufficient magnetic susceptibility contrast will exist between tuffs and basaltic dikes to create a substantial total field anomaly, in other cases it will not.

Tarling (1983) found that nearly all igneous rocks carry remanent magnetizations between 1 and 100 Am^{-1}. This means that most dikes and lava flows have total field anomalies that are dominated by the remanent vector of magnetization. Nearly all of this remanent magnetization occurs as thermo-remanent magnetization in igneous rocks. As a result, lava flows, dikes, and agglutinated spatter are likely to carry a high remanent magnetization. Cinder cones in which the cinders and ash are highly brittle are not likely to carry a large remanent magnetization. In older cones and lava flows the remanent magnetization may be reversed or rotated. In these cases the resulting magnetic anomaly map will likely have a complex pattern.

7.3 MAGNETIC SURVEYS IN VOLCANIC FIELDS

It is slightly ironic that the development of quantitative methods for the interpretation of magnetic data far outpaces the application of these methods to surveys of volcanic fields or to the solution of geological problems in general. Early investigations applying magnetic methods to problems in volcanology and tectonics include Dubois and Carey (1964), Harrison (1968), Cole and Hunt (1968), and Spector and Grant, 1970. Recent examples of the application of magnetic methods in volcanology and tectono-magmatic problems include Nunziata and Rapolla (1981, 1987), Goulty et al. (1984), Dzurisin

Table 7-1. Conversion from SI units to Gaussian units for common magnetic terms

Quantity	Symbol	SI Units	Conversion	Gaussian
Magnetic Induction	**B**	Tesla ($A^{-2}kg\ s^{-2}$)	1 Tesla=10^{4}gauss 1 nT=1γ=10^{-5} gauss	gauss ($g^{1/2}cm^{-1/2}s^{-1}$ ($\mu^{1/2}$))
Magnetic Field Strength	**H**	(Am^{-1})	1 Am^{-1}=4 $\pi 10^{-3}$ Oe	oersted ($g^{1/2}cm^{-1}s^{-1}$ ($\mu^{-1/2}$))
Magnetic Susceptibility	*k*	dimensionless	1 (SI)=1/4π (emu)	dimensionless
Intensity of Magnetization	**I** or **J**	Tesla ($A^{-2}kg\ s^{-2}$)	1 Tesla=10^{4} gauss 1 nT=1γ=10^{-5} gauss	gauss ($g^{1/2}cm^{-1/2}s^{-1}(\mu^{1/2})$)

et al. (1990), Young and Lucas (1988), Rout et al. (1993), and Zeyen et al. (1991). Four examples of the application of magnetics to volcanological and tectono-magmatic problems are discussed in the following sections. Aeromagnetic surveys of the island of Hawaii (Flanigan et al., 1986; Flanigan and Long, 1987) provide a state-of-the-art example of the application of low-level draped (nearly constant height above the surface) aeromagnetic surveys to the study of dike complexes and related anomalies in basaltic terrains. The second example, from the northern Nevada tectonic corridor (Zoback et al., 1994), involves the use of regional aeromagnetic data, coupled with more detailed ground geophysical investigations and geologic mapping to help construct a tectono-magnetic model of the region. The third example, from a ground magnetic survey in the San Francisco volcanic field, illustrates the use of magnetic data in the identification of individual dikes on a local scale, a problem relevant to issues such as the area of the repository likely to be disrupted should volcanism occur. The final example summarizes aeromagnetic and ground magnetic studies in Amargosa Valley (Langenheim et al., 1993). These studies in Amargosa Valley have already had direct impact on volcanism probability models and our understanding of the recurrence and distribution of volcanoes in the YMR.

7.3.1 Hawaii

Flanigan et al. (1986) and Flanigan and Long (1987) have summarized aeromagnetic surveys and the interpretation of aeromagnetic anomalies on the island of Hawaii. Two detailed aeromagnetic surveys have been made of all or part of Hawaii, including a 300 m elevation draped aeromagnetic survey (Godson et al., 1984) and a more localized very low elevation (90 m) draped survey of parts of Kilauea and Mauna Loa volcanoes (Figure 7-1) (Flanigan et al., 1986). In the low-level survey, Flanigan et al. (1986) report that variance in flight elevation was 1$\pm$30 m, except over pit craters and cinder cones. These features produced short-wavelength, large-amplitude anomalies on the aeromagnetic map.

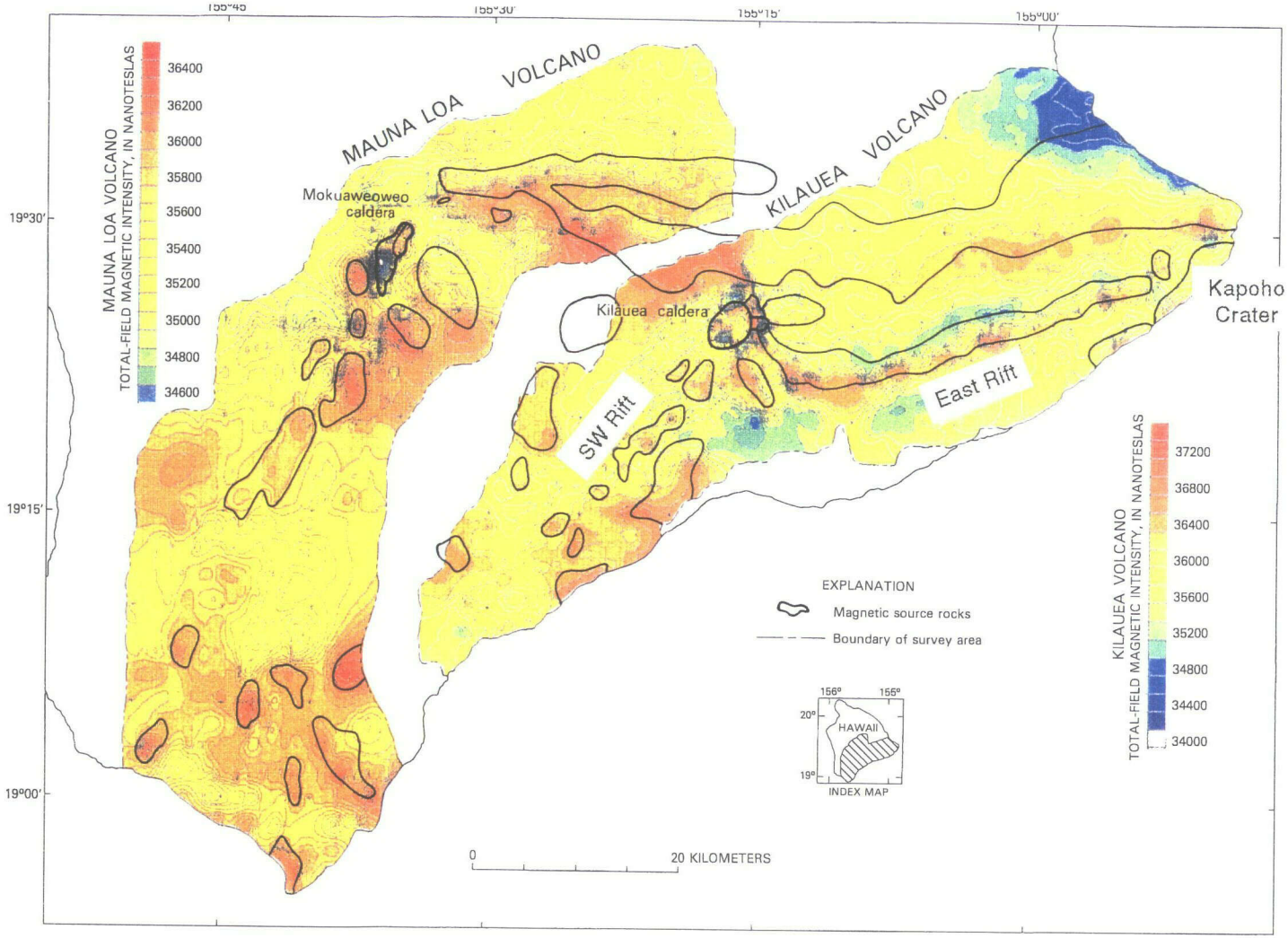

Figure 7-1. Low-level (90 m, draped) aeromagnetic survey of Kilauea and Mauna Loa volcanoes (from Flanigan and Long, 1987). Prominent aeromagnetic anomalies are outlined.

Flanigan and Long (1987) note that remanent magnetization is about ten times the strength of induced magnetization in Hawaiian basalts. Furthermore, dikes on Hawaii carry a higher apparent remanent magnetization than lava flows. Flanigan and Long (1987) attribute this to post-cooling rotation and breakup of lava flows. As a result, on average the remanent magnetization of the lavas is low. Anomalies associated with flows are complex but of comparatively low amplitude, especially when the magnetometer is relatively far from these blocks, as in the case in aeromagnetic surveys. The disparity in the remanent magnetization vectors between the basaltic lava flows and dikes provides, in some cases, sufficient magnetization contrast for dikes to be identified beneath and within lava flow sequences.

The most prominent feature identified on the aeromagnetic map (Figure 7-1) of Kilauea is a 2,000 nT anomaly over the East Rift, which extends for 7 km eastward from the summit caldera. This anomaly is likely the result of a massive dike complex injected to shallow depth beneath the rift zone (Flanigan and Long, 1987). Magnetic anomalies associated with the SW rift of Kilauea and the NE rift of Mauna Loa are more subtle. These rift zones are manifest by a series of comparatively short-wavelength, isolated magnetic anomalies that together delineate the rift trend in the magnetic data (Figure 7-1) (Flanigan and Long, 1987). Anomalies along these rift zones have amplitudes of 100–500 nT. Comparison of these anomalies with the dramatic anomaly along the East Rift of Kilauea epitomizes the difficulty in delineating subsurface dike complexes in basaltic terrains. The anomalies associated with the East Rift are unmistakable. In comparison, the SW rift zone of Kilauea, also a substantial dike complex, especially when compared with small volume dike complexes in continental volcanic fields, lacks a continuous anomaly pattern even at a flight elevation of 90 m. This absence of a distinct anomaly pattern may be attributable, in part, to differences in dike orientation relative to the orientation of the vectors of magnetization for these basalts. Map enhancement techniques, such as reduction to the pole (Hildenbrand, 1983), or reduction of terrain effects through cross-correlation with topography (Grauch and Campbell, 1984; Gregotski et al., 1991) may help differentiate the SW rift zone anomalies from the surrounding flows and reveal their true map extent.

Other anomalies include 900–1,200 nT anomalies associated with Kapoho crater and Halemaumau pit crater, Kilauea Caldera. These anomalies are likely the result of rock or magma at shallow depth and at temperatures higher than the Curie point for these rocks. Such magnetic anomalies are the result, therefore, of a contrast between high-temperature zones, within which the remanent magnetization is low, and surrounding cool rock, which has a high remanent magnetization. Similar thermal anomalies have been mapped at different scales using magnetic methods at Usu volcano, Japan (Nishida and Miyajima, 1984), Mount St. Helens (Dzurisin et al., 1990), and Colima Volcano, Mexico (Lane et al., 1993; Connor et al., 1993). Flanigan and Long (1987) modeled these anomalies as conduits, using nonmagnetized vertical-sided prisms.

7.3.2 SW Nevada Tectonic Corridor

Studies of the Nevada tectonic corridor illustrate the utility of integrated regional aeromagnetic, ground geophysical, and geological investigations with the goal of describing tectonic and tectono-magmatic processes. Zoback et al. (1994) recently summarized the geological and geophysical setting of the northern Nevada rift, a NNW-trending belt of basaltic dikes and related igneous rocks. The entire Nevada rift extends from north-central Nevada to central-east Nevada. This zone is over 500 km long and is defined primarily by aeromagnetic anomalies (McKee and Blakely, 1990; Blakely et al., 1989; Zoback and Thompson, 1978).

Aeromagnetic data collected in the National Uranium Resource Evaluation (NURE) program were used to identify and determine the extent of the Nevada tectonic corridor. Details of the magnetic profiles, including those presented in Zoback et al. (1994) and modified from Hildenbrand and Kucks (1988), were used to describe the length width, and offsets within the rift zone. In this regional survey, the simple identification and mapping of the aeromagnetic anomaly, coupled with cross-correlation with regional geologic data, has been most useful for investigation of the rift zone, rather than the forward or inverse modeling of these aeromagnetic data.

Zoback et al. (1994) produced geologic maps of the northern part of the corridor, mapping dikes of more than 15 percent by volume in some parts of the northern rift zone. Ground magnetic and gravity surveys were also made across the northern rift zone. The magnetic data reveal a 600 nT anomaly over a 4-km-wide dike swarm within the rift zone. Zoback et al. (1994) assumed a uniform dike susceptibility of 0.034 (SI) to model the long-wavelength component of the anomaly. Their forward model indicates that the dike zone extends vertically to depths of at least 12 to 15 km, and that no more than 25–30 percent of this volume is occupied by dikes, a high intrusive to country rock ratio for continental, extensional settings. Complications in the relationship between the gravity and magnetic data (Zoback et al., 1994) indicate that further data collection may refine the models considerably. Nevertheless, the integrated approach to the regional setting of dikes in the Nevada corridor provides a framework for additional studies and debate (Li et al., 1990) and the development of tectonic models for the evolution of the region.

7.3.3 Spider Web Ranch, San Francisco Volcanic Field, Arizona

Ground magnetic surveys are normally employed on a considerably more local scale than is possible using aeromagnetic surveys for the delineation of individual dikes or dike swarms. Normally, these ground magnetic surveys focus on collecting sufficient data to map the length, width, orientation, and depth of subsurface dikes, in order to better constrain structural and volcanological models of a local area. Magnetic anomalies associated with the Spider Web Ranch vent complex in the San Francisco volcanic field provide a useful example of the utility of ground magnetic surveys for the delineation of individual dikes. Conway[2] made a series of gravity and ground magnetic traverses across the Spider Web Ranch complex, on the NE edge of the San Francisco volcanic field, Arizona. The Spider Web Ranch complex consists of several basaltic cinder cones and lava boccas which align on a roughly NE trend and which are located at the NE end of a cinder cone alignment that transects the eastern part of the San Francisco volcanic field (Connor and Hill, 1993b). The Spider Web Ranch complex lies directly over the lower sandstone member of the Triassic Moenkopi formation, which crops out throughout the region.

Basaltic lavas of the Spider Web Ranch complex are reversely magnetized. One K-Ar date from a flow in the complex gives an age of 1.2 ± 0.3 Ma (Tanaka et al., 1990). Seven basaltic dikes crop out within the complex, four of which are oriented NE, parallel to the trend of the cinder cone alignment and to other regional structures. The northernmost dike outcrop in the complex is located within a small-displacement, normal, NE-trending fault. The lava flows, agglutinate, and dikes of the Spider Web Ranch complex are petrographically identical plagioclase-phyric basalts. Crustal xenoliths, particularly from the Moenkopi formation, are abundant in many of the dikes. Many of these features indicate that the Spider Web Ranch complex and other nearby centers are excellent examples for the study of vent alignment

[2] Conway, M.F. 1994. Written communication to C.B. Connor.

development, the relationship between faults, joints, and dike injection on a local scale (McDuffie et al., 1994), and some aspects of the mechanics of small-volume cinder cone eruptions.

Conway[2] made a series of detailed ground magnetic traverses across the Moenkopi sandstone NE and SW of the Spider Web Ranch complex to determine the map extent of dikes in the area. Station spacing along these traverses varied from 50 to 2.5 m due to the large-amplitude and short-wavelength anomalies identified along the traverses. Two magnetic profiles, one 50 m NE of the NE margin of the Spider Web Ranch basalt, and the other 750 m SW, are shown in Figures 7-2(a) and 7-2(b). Both profiles have large-magnitude ($>1{,}000$ nT) magnetic anomalies that have wavelengths of less than 50 m. In combination with other nearby traverses, these data indicate the presence of one or more shallow, thin dikes, which carry a strong remanent magnetization. These dikes trend NE and extend beneath the Spider Web Ranch complex basalts, parallel to the trend of the cinder cone alignment.

The Spider Web Ranch magnetic survey indicates the utility of ground magnetic surveys in basaltic volcanic fields under special circumstances. The magnetization contrast between the Moenkopi sandstone and the Spider Web Ranch basalts is substantial and the dikes extend well beyond the limits of the flows at a shallow depth. Conway[2] plans further field work in order to better delineate the extent of the dikes in the Moenkopi and document details of their relationship to mappable geologic structures.

Parenthetically, it is notable that magnetic measurements could not be collected on the lava flows in the Spider Web Ranch complex because of the unusually high magnetic gradients found there. Multiple readings at some stations on the basalt flows, for example, show spatial variations on the order of 1,000 nT/m. This variation strongly suggests the lava flows and other basalts in the area carry a strong isothermal remanent magnetization, produced by lightning strikes over time. The density of lightning strikes on a 1 Ma basalt exposed in the San Francisco volcanic field may be as high as 1 m^{-2}.[3] This high isothermal remanent magnetization prevents collection of any useful magnetic data on the lava flows themselves.

7.3.4 Amargosa Desert

The ability to delineate large igneous features in sedimentary sequences using magnetic methods is well illustrated by the recognition and mapping of magnetic anomalies associated with the Amargosa volcanic centers (Langenheim et al., 1991; 1993) in the YMR. Langenheim et al. (1993) identified five aeromagnetic anomalies in the Amargosa Valley using aeromagnetic data collected at a flight elevation of 122 m above the surface (labeled *A-E* in Figure 7-3) (Langenheim et al., 1991). The locations of these magnetic anomalies with respect to Yucca Mountain and the basaltic cinder cones of Crater Flat are shown in Figure 7-4.

These five anomalies vary in amplitude considerably. All of the anomalies are recognized by their distinctive dipolar character, indicating they are the result of shallow, areally restricted magnetized bodies. The largest and most complex aeromagnetic anomaly is anomaly ***B*** (Figure 7-3), having an amplitude of 350 nT at a flight elevation of 122 m (Langenheim et al., 1993). Ground magnetic traverses across anomaly ***B*** have robust signatures with a total amplitude variation of more than 1,000 nT. This

---

[3] E. Shoemaker. 1993. Personal communication to C.D. Condit, U.S. Geological Survey, Flagstaff, AZ.

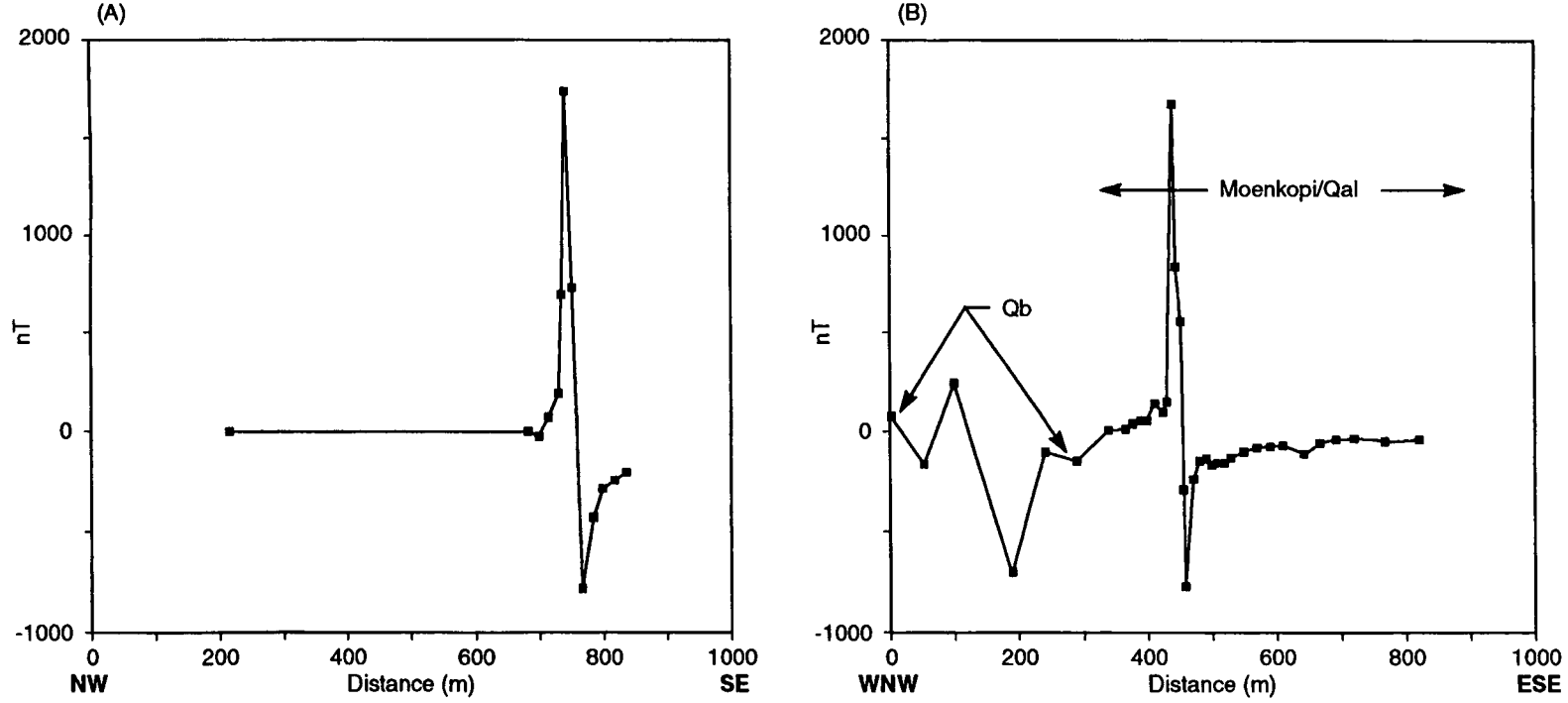

Figure 7-2. Ground magnetic traverses across subsurface dikes (a) NE and (b) SW of the Spider Web Ranch vent complex

Figure 7-3. Aeromagnetic map of the Amargosa Valley (From Langenheim et al., 1993). Contour interval is 20 nT. Magnetic anomalies A–E are labeled.

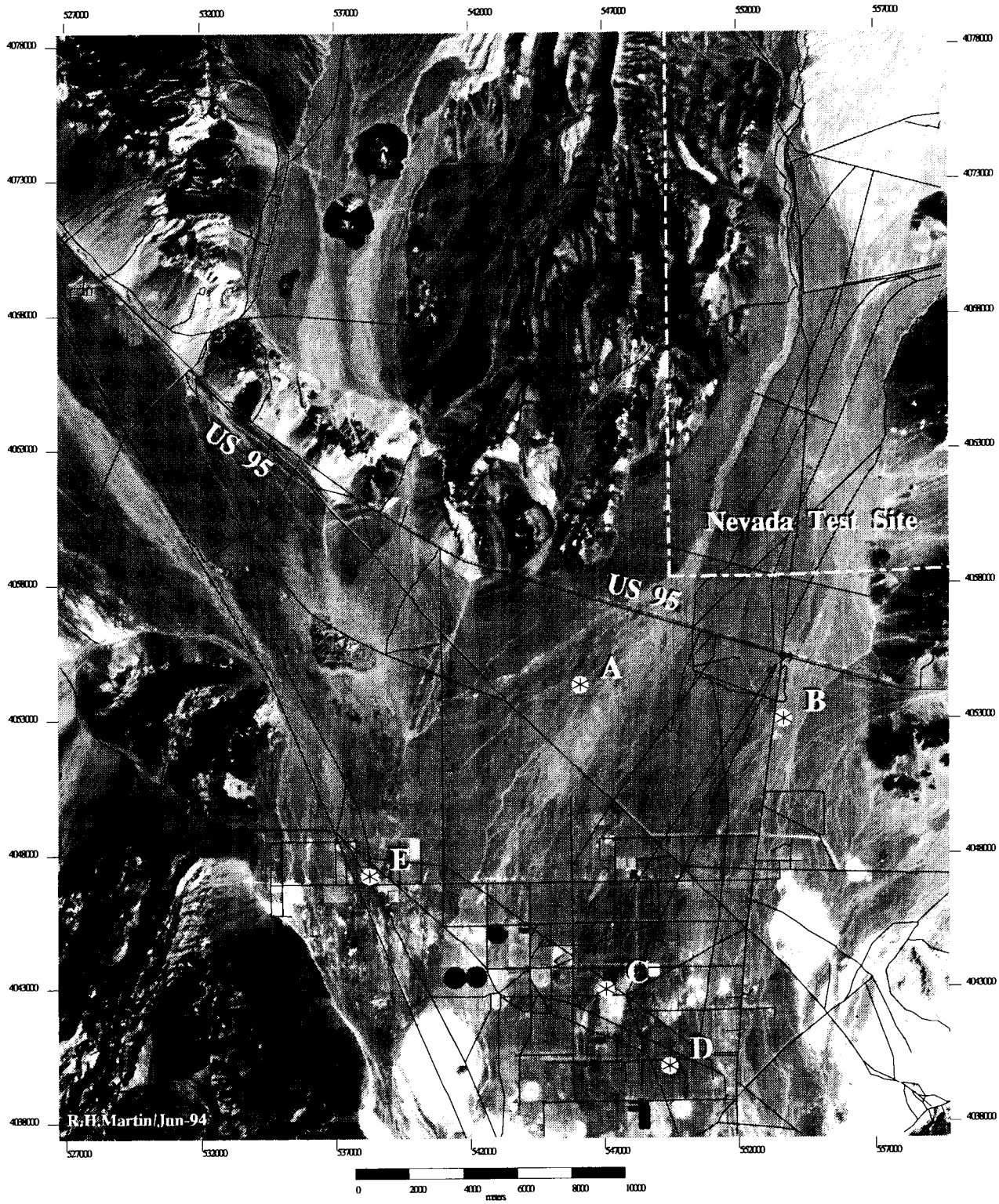

Figure 7-4. Aeromagnetic anomalies in the Amargosa Valley (labeled *A–E*) and their geographic relationship to volcanoes in Crater Flat Valley and Yucca Mountain

indicates a shallow source of the anomaly. Anomaly ***B*** is reversely polarized. Langenheim et al. (1993) created several 2D and 2.5D models using ground magnetic data across anomaly ***B*** and suggested that the source of the anomalies is a dike and flow complex. Crowe et al. (1993) indicate these anomalies are largely extrusive structures that have subsequently been buried by sediments during the Plio-Quaternary.

Other aeromagnetic anomalies in the Amargosa Valley have smaller amplitudes, on the order of 100 nT or less. These anomalies are reversely or normally polarized and some of the anomalies, such as anomaly ***E*** (Figure 7-3), appear to have been rotated. Walker and Eakin (1963) report intersecting basalt in a drill hole at a depth of 183 m near anomaly ***D***. This basalt layer was 9 m thick. It is uncertain whether the other anomalies are produced by basalt, but given the robust character of the anomalies and the presence of basalt at anomalies ***B*** and ***D***, it seems reasonable to assume the other anomalies are also related to buried volcanic or intrusive features.

Identification of basalts at the location of anomalies ***B*** and ***D*** is important for two reasons. First, recognition of the anomalies and sampling of the basalt through drilling lends credence to the idea that large, shallow, probably extrusive, volcanic structures can be recognized in deep alluvial basins using low-level aeromagnetic surveys in the YMR. By the same token, the survey (Langenheim et al., 1991) also indicates some of the limitations of the aeromagnetic data. On the edges of the Amargosa Valley, the aeromagnetic data exhibit a high-frequency component due to the shallowing basement and outcrops of Miocene tuff on the basin edge (Figure 7-3). Smaller aeromagnetic anomalies, such as anomalies***A*** or ***E***, would be difficult to identify at locations where the basement is comparatively shallow. Thus, the correlation of the aeromagnetic anomalies with the deeper portions of the Amargosa Valley may result from limitations of the aeromagnetic method: older, buried volcanic centers may be present elsewhere in the Amargosa Valley in locations where shallow basement produces complex magnetic anomalies. Magnetic anomalies associated with possible buried volcanic centers would be obscured by these basement magnetic anomalies. Second, the Amargosa Valley basalts are relatively close to Lathrop Wells and Crater Flat (Figure 7-4). Recognition of these volcanic centers essentially doubles the number of Pliocene (?) volcanic centers in the vicinity of Yucca Mountain and provides further evidence that basaltic volcanism has been widespread in the area. This has an important impact on most models for the recurrence rate of volcanism and the probability of volcanic disruption of the candidate repository (Connor and Hill, 1993a; Crowe et al., 1993). The change in polarity of the anomalies suggests that some of the anomalies, for example anomaly ***E***, may be substantially older or younger than drilled and sampled anomalies. This too may impact probability calculations.

8 PARAMETRIC STUDY OF MAGNETIC ANOMALIES

8.1 MAGNETIC ANOMALIES RESULTING FROM DIKES—SIMPLE CASES

Magnetic anomalies are complex due to the many parameters that influence their shape. The parameters that most influence magnetic anomalies associated with basaltic igneous features are:

- The magnitude of the contrast between total magnetization vectors in the basalt and surrounding rock. The magnitude of the total magnetization vectors in turn, depends on the normal remanent magnetization vector, $\mathbf{J}_r$, and the induced magnetization vector, $k\mathbf{H}$.
- The orientation of the Earth's magnetic field in the area and the orientation of remanent magnetization vectors in the basalt and in the surrounding rock.
- The size of the basaltic feature with respect to the sample interval of the magnetic survey.
- In the case of basaltic dikes, the orientation of the dike with respect to the vector of total magnetization contrast.
- In the case of basaltic dikes, the dip of the dike.
- The distance of the magnetometer from the feature. Usually the depth of the top of the feature is of primary importance.

These parameters act together to control the amplitude and wavelength of magnetic anomalies. Figures 8-1(a)–8-1(d) illustrate the impact of parameter variation on the magnetic anomaly resulting from a N-S traverse across an E-W-trending, normally-polarized dike. A dike geometry is chosen because it is the most common intrusive igneous structure in basaltic volcanic fields, and because recognition and characterization of dikes is an important aspect of site characterization. In all of these examples the surrounding medium is assumed to be magnetically transparent in order to simplify the anomaly shape.

The depth to the top of a dike is an important parameter controlling the amplitude of the magnetic anomalies. Figure 8-1(a) shows the anomaly produced by an E-W-trending, 5-m-wide dike at various depths. The dike is assumed to be normally polarized and the direction of total magnetization is oriented parallel to the Earth's magnetic field. The Earth's field is assumed to have inclination 62° and declination 14°. The calculations are made on a N-S trending line, orthogonal to the dike and the dike extends for a distance of 5 km in both directions from the traverse line, essentially giving it an infinite extent (Rao and Subrahimanyam, 1985). The five curves shown in Figure 8-1(a) show the anomaly produced by a dike, where the depth to the top of the dike is 1, 5, 10, 50, and 100 m, with increasing depth corresponding to a decrease in the amplitude of the magnetic anomaly. The magnitude of the anomaly (difference between anomaly maximum and minimum) decreases by about two orders of magnitude with an increase in depth to the top of the dike from 1 to 100 m. The effect of changing dike thickness is illustrated in Figure 8-1(b). Here the top of the dike is assumed to be at a depth of 4 m. The total field anomaly is calculated for dike thicknesses of 15, 5, 1 m, 50, and 10 cm, in order of decreasing amplitude. In Figure 8-1(c), the geometry of the dike is held constant (a 5-m wide, E-W-trending dike; depth to the top of the dike is 4 m) and the magnetization of the dike is changed from 1, 5, 10, and 50 Am^{-1}. This range encompasses the likely range of magnetizations in basalts.

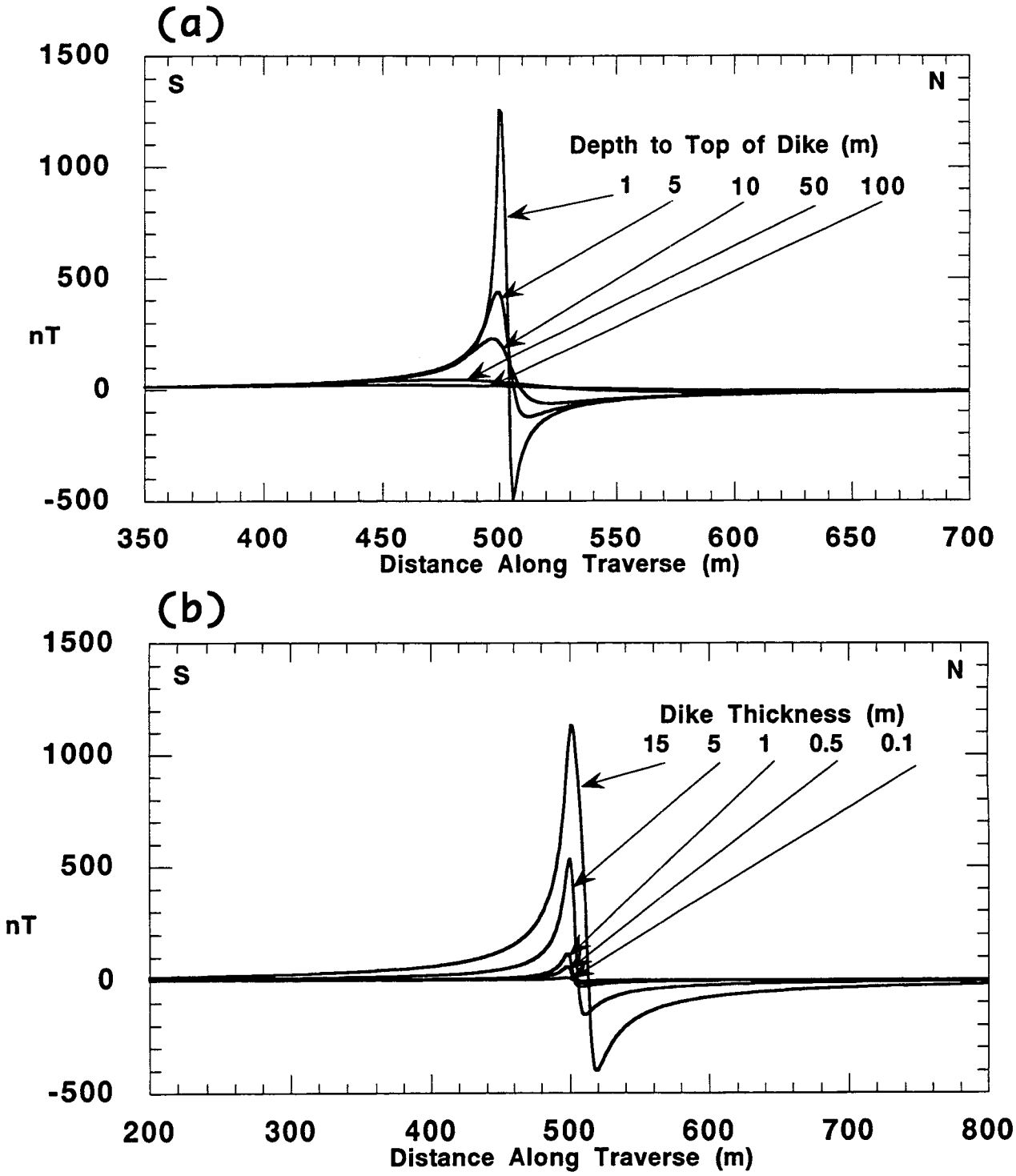

Figure 8-1. Change in anomaly magnitude, wavelength, and shape with changing depth to the top of the dike: (a) dike depth, (b) dike thickness

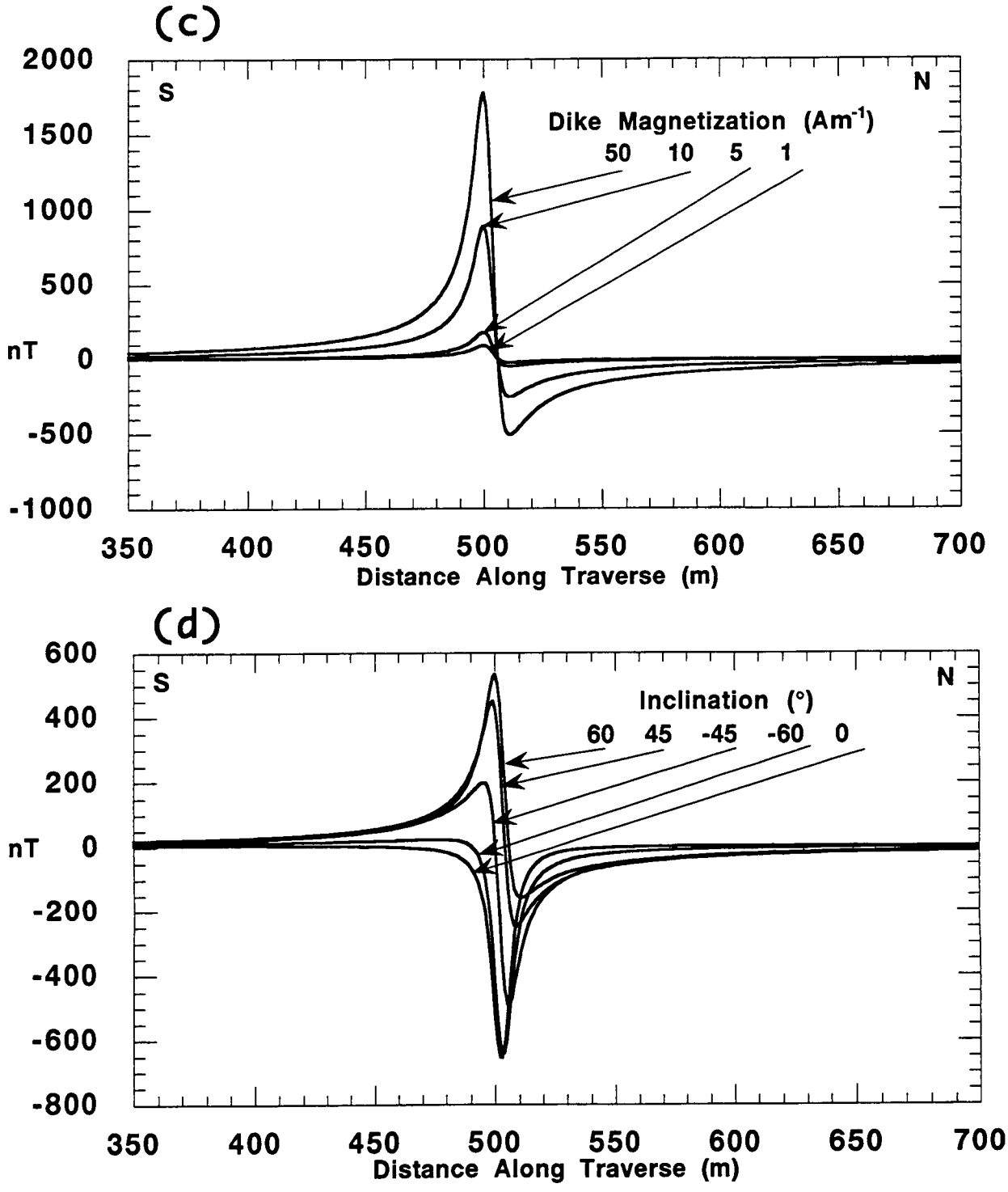

Figure 8-1. Change in magnetic anomaly with change in (c) dike magnetization, and (d) inclination of the vector of magnetization (Cont'd.)

Variation in these parameters may produce widely varying map patterns in magnetic anomalies, especially where dikes are emplaced adjacent to one another. Comparing Figures 8-1(a)–8-1(c), it is clear that changing dike thickness has a similar effect to changing the depth to the top of the dike on the amplitude of the anomaly. For shallow dikes, the wavelength of the anomaly increases more rapidly with changing thickness than results from increasing depth. However, in practice it is possible to model a given magnetic anomaly in an infinite number of ways by changing these geometric terms. The indeterminate nature of forward magnetic modeling results in ambiguity in the interpretation of magnetic map anomalies. Orientation of the vector of total magnetization complicates the interpretation of anomalies further [Figure 8-1(d)]. In this case, changing the inclination from 60° through −60° produces a substantial change in the amplitude of the positive and negative portions of the anomaly. Rotating the declination of the vector of magnetization with respect to north and the dike trend have a similar impact on the character of magnetic anomalies. This effect is usually quite important in basalts because of their high Kŏnisberger ratio (ratio of remanent to induced magnetization) (Hood, 1964).

The trend of a dike will further impact the character of the total magnetic field anomaly. Rao and Babu (1991) cast the equations developed by Talwani (1965) in a more computationally efficient form, enabling rapid calculations of vertical sided prisms of any dimension, depth, and magnetization. Figure 8-2(a) illustrates the magnetic anomaly pattern resulting from the intrusion of a single vertical dike into magnetically quiet alluvium. The dike (dike 3 in Table 8-1) is reversely polarized and trends N-S. Because of its orientation and polarity, the anomaly associated with this dike is comparatively subtle, considering its shallow depth and thickness. The shape of the anomaly does not well reflect the orientation of the dike, primarily because of the dike orientation. The largest portion of the anomaly is 100 nT in amplitude, centered on the southern tip of the dike. Adding dikes 1 and 2 [Table 8-1, Figure 8-2(b)], which are assumed to be normally polarized, produces a complex anomaly pattern. The total field magnetic anomaly is most influenced by dike 2, the shallowest of the dikes. As a result of the interaction between the magnetic anomalies related to dikes 2 and 3, the trend of the steepest magnetic gradient is not parallel to dike 2; rather, it trends at an azimuth of approximately 30°. Dike 1 influences the map pattern but is comparatively indistinct on the total magnetic field anomaly map.

Figure 8-2(b) further illustrates the indeterminacy related to the interpretation of magnetic anomalies. Numerous interpretations of the map pattern are possible. For example, a straightforward, but incorrect, interpretation of the magnetic map pattern would be that the magnetic anomaly results from a single dike trending at approximately 30°, centered below the steepest gradient in the anomaly. This ambiguity needs to be kept in mind because it exists in all facets of the interpretation of magnetic data.

8.2 DIKES IN THE TIVA CANYON TUFF

A dike located within or near the candidate repository site intrudes the Paintbrush Tuff. Basalt intruding a welded tuff will have an induced and remanent component of magnetization. The welded tuff will also carry these two components of magnetization. The difference in the sum of the magnetization vectors for each unit defines the total magnetization contrast between those two units, and the character of the magnetic anomaly resulting from this contrast. The magnetic properties of tuff units at Yucca Mountain have been investigated in detail by Rosenbaum (1986). The magnetic properties of the Tiva Canyon Member of the Paintbrush Tuff are important in particular because the Tiva Canyon is the uppermost tuff in the Paintbrush Formation, capping Yucca Mountain. Here the magnetization of the Tiva Canyon is discussed in terms of its effect on the magnetic anomalies likely to be produced by dikes within the Tiva Canyon. The results, however, are equally applicable to other tuff units in the region.

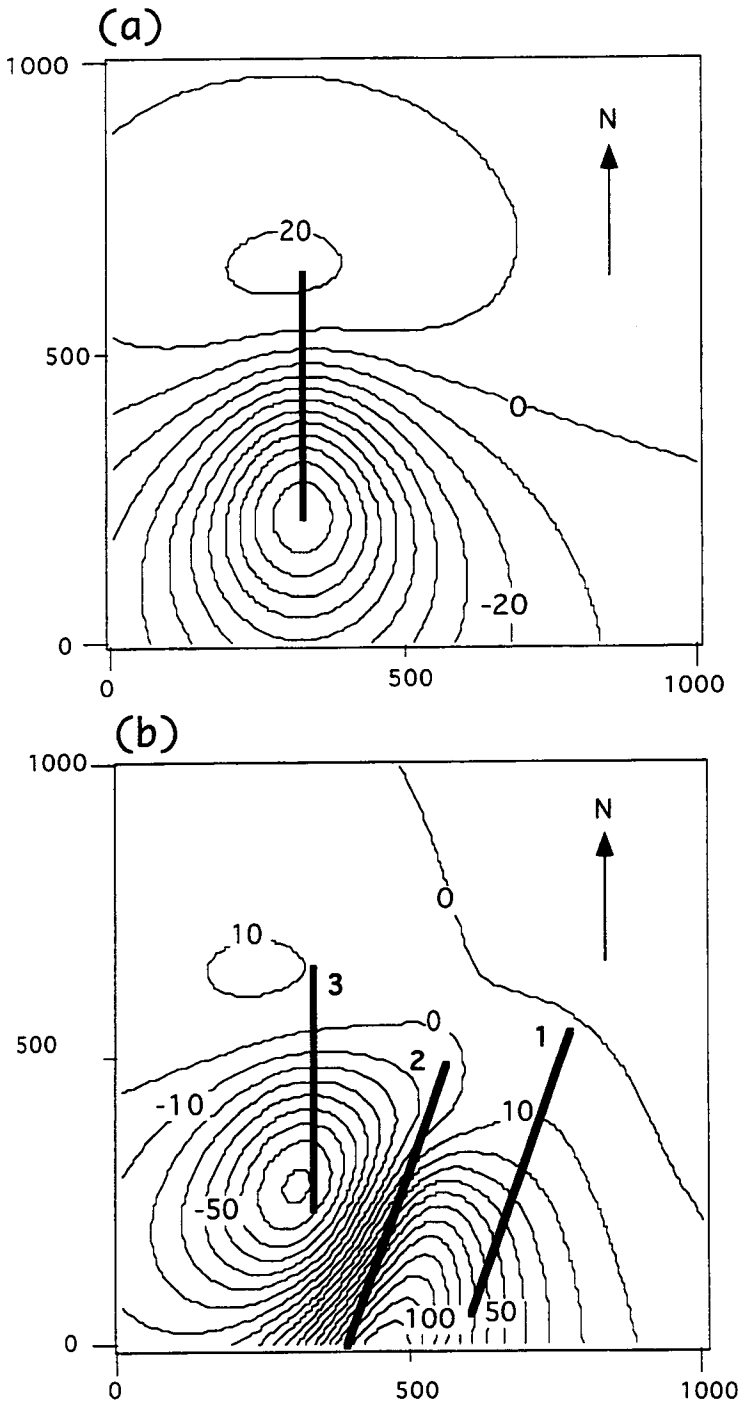

Figure 8-2. Magnetic map anomaly patterns resulting from (a) a single dike and (b) three dikes. Dike magnetic properties are summarized in Table 8-1. Map units are in meters and the magnetic anomalies are contoured in nT.

Table 8-1. Geometry and rock magnetic properties of the three dikes illustrated in Figure 8-2

	Geometry			Vector of Magnetization		
Dike	Depth (m)	Thickness (m)	Trend (degrees)	J Am^{-1}	D_r (degrees)	I_r (degrees)
1	25	5	20	15.8	14	62
2	15	5	20	15.8	14	62
3	20	5	0	5.0	170	−45

The Tiva Canyon Tuff carries a magnetic susceptibility between 2×10^{-3} (SI) and 1.1×10^{-2} (SI) and a normal remanent magnetization, $\mathbf{J}_r$, with magnitude of 0.4–10 Am^{-1} (Oliver et al., 1990; Rosenbaum, 1986). The Paintbrush Tuff formed approximately 12.5 Ma and is reversely polarized. At Yucca Mountain, the Earth's magnetic field strength is approximately 560 Am^{-1} (0.56 Oe), the declination is 14° and inclination 62°. Therefore, the magnitude of the induced component of magnetization, $\mathbf{J}_i$, is between 8.9×10^{-2} and 4.9×10^{-1} Am^{-1}. The magnitude of $\mathbf{J}_r$ exceeds the magnitude of $\mathbf{J}_i$ by up to two orders of magnitude. For practical purposes, it can be assumed that the total magnetization vector, $\mathbf{J}_{tot}$, for the Tiva Canyon Tuff is equal to $\mathbf{J}_r$.

However, the declination and inclination of $\mathbf{J}_r$ vary substantially within the Tiva Canyon Tuff across Yucca Mountain (Rosenbaum, 1986). Oliver et al. (1990) have noted a clockwise rotation of the vector of remanent magnetization in the Tiva Canyon Tuff in the southern part of Yucca Mountain with respect to the northern part of the mountain. This change in declination may have a substantial impact on the magnetization contrast between the Tiva Canyon Tuff and a basaltic dike. For example, assuming that the Tiva Canyon Tuff carries a remanent magnetization vector of magnitude 5 Am^{-1}, declination 220°, and inclination −60°, recalling that the angle of inclination is positive downward, the components of the total vector of magnetization in the Tiva Canyon Tuff are:

$$\begin{aligned} J_{x,\,TC} &= \mathbf{J}_r \cos(I_r) \cos(D_r) = -1.9\ Am^{-1} \\ J_{y,\,TC} &= \mathbf{J}_r \cos(I_r) \sin(D_r) = -1.6\ Am^{-1} \\ J_{z,\,TC} &= \mathbf{J}_r \sin(I_r) = -4.33\ Am^{-1} \end{aligned} \qquad (8\text{-}1)$$

Consider the magnetizations of two hypothetical dikes intruding the Tiva Canyon Tuff. Both dikes carry mean susceptibilities for basalt, so that the magnitude of induced magnetization for both dikes is about $\mathbf{J}_i = 1$ Am^{-1}. The magnitude of the vector of normal remanent magnetization, $\mathbf{J}_r$ for both dikes is assumed to be 10 Am^{-1}. The first dike is normally polarized, with a declination 0° and inclination 62°. Adding the components of induced and remanent magnetization in the normally polarized dike, the components of magnetization are:

$$
\begin{aligned}
J_{x,\ \text{dike}} &= \mathbf{J}_r \cos(I_r) \cos(D_r) + \mathbf{J}_i \cos(I_o) \cos(D_o) = 5.1\ \text{Am}^{-1} \\
J_{y,\ \text{dike}} &= \mathbf{J}_r \cos(I_r) \sin(D_r) + \mathbf{J}_i \cos(I_o) \sin(D_o) = 0.1\ \text{Am}^{-1} \\
J_{z,\ \text{dike}} &= \mathbf{J}_r \sin(I_r) + \mathbf{J}_i \sin(I_o) = -9.7\ \text{Am}^{-1}
\end{aligned}
\tag{8-2}
$$

Subtracting the components of magnetization of the Tiva Canyon Tuff from those of the basalt gives the magnetization contrast between the dike and the Tiva Canyon Tuff:

$$
\begin{aligned}
J_x &= J_{x,\ \text{dike}} - J_{x,TC} = 7.1\ Am^{-1} \\
J_y &= J_{y,\ \text{dike}} - J_{y,TC} = 1.7\ Am^{-1} \\
J_z &= J_{z,\ \text{dike}} - J_{z,TC} = 14.0\ Am^{-1}
\end{aligned}
\tag{8-3}
$$

The magnitude of the total magnetization contrast between the dike and the tuff is 15.8 Am^{-1}, oriented at declination 13° and inclination 62°. In this case the contrast is large because of the opposite polarity of the units. This enhances the total field magnetic anomaly. The contrast is quite different if the intruding dike is reversely polarized. For example, if $D_r = 180°$ and $I_r = -60°$, and all other magnetic properties of the dike are the same as in the previous example, the magnitude of the magnetization contrast between the tuff and the reversely polarized dike will be about 4.6 Am^{-1}, with declination 143° and inclination −51°. Clearly, the normally and reversely polarized dikes have substantially different magnetization contrasts and will produce substantially different anomalies should they intrude the Tiva Canyon Tuff.

In order to assess the differences between anomalies due to normal and reversely polarized dikes, magnetic anomaly maps were calculated using the parameters discussed above, again using the methods of Rao and Babu (1991). Anomaly maps for the magnetization contrasts calculated above are illustrated in Figure 8-3(a) for a normally polarized dike and Figure 8-3(b) for a reversely polarized dike intruding the Tiva Canyon Tuff. The dike is assumed to be 5 m wide and approximately 500 m long, trending at an azimuth of 20° from true north, roughly parallel to magnetic north in the YMR. This orientation was chosen because it parallels major structures in the area, such as the Ghost Dance and Solitario Canyon faults, and is roughly orthogonal to the direction of minimum horizontal stress. The depth to the top of the dike is assumed to be 250 m and the dike extends vertically from 250 m depth to great depth. Topographic effects are ignored in these calculations.

Several features of these maps provide insight into the likely character of magnetic anomalies which might be produced by dikes within the Tiva Canyon Tuff. First, dikes trending at 20° will produce subtle anomalies in this region unless the $\mathbf{J}_r$ is large and strongly rotated with respect to the current declination of the Earth's magnetic field, 14°. Second, both anomalies are dipolar. Because of the inclination assumed for both $\mathbf{J}_i$ and $\mathbf{J}_r$, either approximately 60° or −60° depending on polarity, the largest amplitude anomaly is centered on the southern tip of most dikes intruding the Tiva Canyon Tuff. This means that magnetic anomalies are likely to be highly asymmetric with respect to the map extent and trend of the dike, rendering anomalies more difficult to interpret. Gradient techniques and frequency filtering work well in some circumstances (e.g., Dean, 1958; Fuller, 1967; Ku and Sharp, 1983), however, these enhancement techniques have to be used with caution if the goal is to identify NE-trending igneous intrusions in the Tiva Canyon Tuff, because of the effects of dike orientation on the anomaly pattern. Third, the overall shapes of the anomalies are broad and of low amplitude, even though the dike

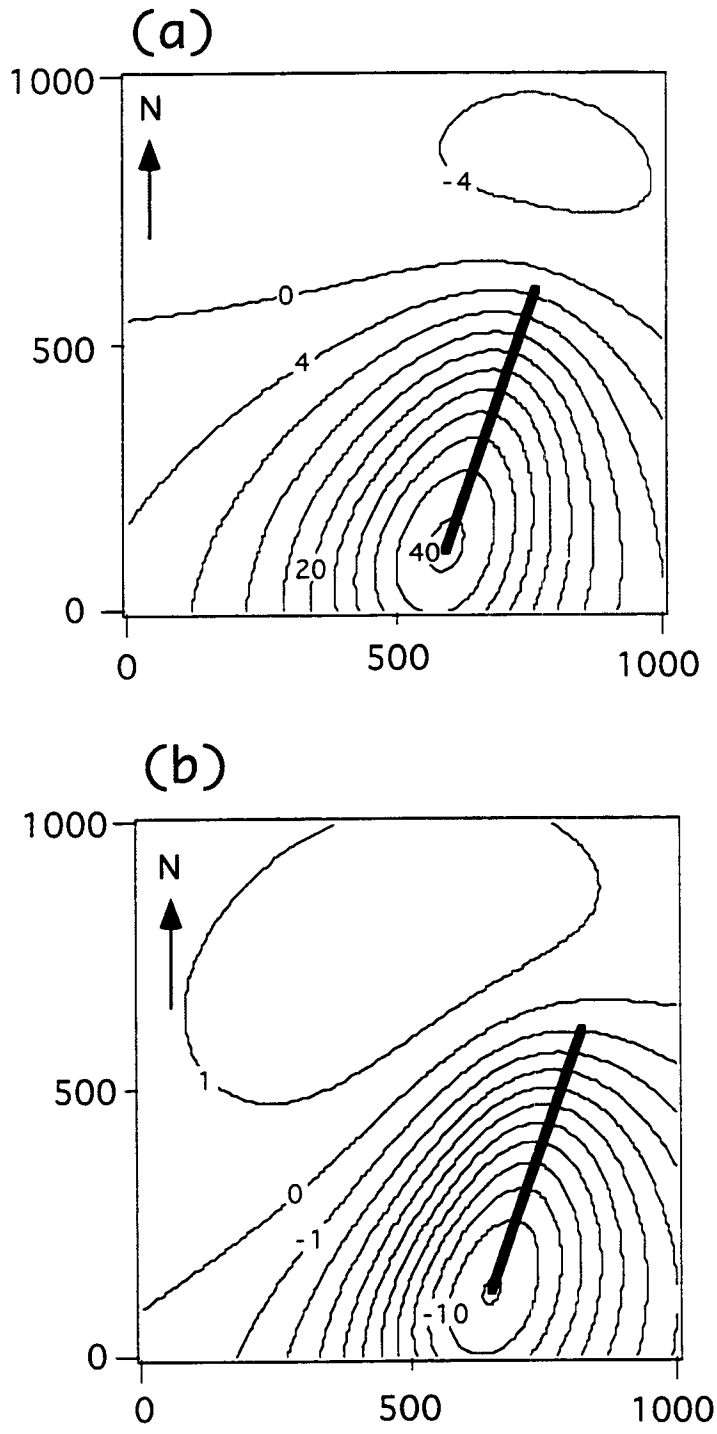

Figure 8-3. Anomaly maps calculated using (a) normal J_r and (b) reverse J_r for a basaltic dike intruding the Tiva Canyon tuff. Magnetization contrast between the dike and the tuff is discussed in the text. The dike is assumed to be 5 m wide and approximately 500 m in length, trending at an azimuth of 20°. The depth to the top of the dike is 250 m. Magnetic anomalies are contoured in nT. Note change in contour interval. Map distance is plotted in meters.

in this example intrudes to shallow depths relative to the candidate repository horizon. Ponce et al. (1992) showed that ground magnetic gradients on the Paintbrush tuff are quite high, commonly on the order of 100 nT per 100 m or more. These horizontal gradients are likely the result of block rotations since the deposition of the tuff, isothermal remanent magnetization, and differential cooling and flow within the tuff (Rosenbaum, 1986). Regardless of their origin, these large local gradients make recognition of anomalies such as those illustrated in Figures 8-3(a) and 8-3(b) extremely tenuous. Upward continuation of these anomalies may help differentiate between anomalies associated with variations in the tuff itself and variations related to dikes. However, this will only be true if the gradient of the magnetic anomalies within the tuff proves to be substantially different from those related to dikes at or more shallow than the repository horizon (<500 m).

8.3 DIKES IN ALLUVIUM

Dikes in alluvium and sedimentary sequences produce more distinctive magnetic anomalies than are likely in tuff for two reasons. First, the total magnetization contrast is usually greater. Sediments and sedimentary rocks usually have normal remanent magnetizations less than induced magnetization (Tarling, 1983). Although these lithologies can carry a significant depositional remanent magnetization caused by preferential orientation of fine grained material at the time of deposition, these rocks do not carry a thermo-remanent component of magnetization. Furthermore, the susceptibilities of sediments and sedimentary rocks are usually low compared with intrusive and extrusive basalts, even if there is a significant volcaniclastic component in the sediment (Tarling, 1983). In contrast with the magnetization of dikes, this essentially renders many sedimentary units magnetically transparent. Second, because of their magnetic properties, sedimentary lithologies tend to be magnetically quiet. These units do not produce the large horizontal magnetic gradients that characterize ground surveys on tuffs and other igneous or metamorphic rocks. These two characteristics make recognition of dikes and related intrusive, or buried extrusive, structures more likely in sedimentary sequences than in igneous or metamorphic rocks.

Recognition of smaller volume features, such as individual dikes or small dike swarms, is nonetheless problematic. These features will, of course, produce smaller magnetic anomalies than those identified in the Amargosa Valley (Langenheim et al., 1993), but may be important from a regulatory perspective because they represent igneous events. Recognition of small volume dikes, or increased confidence in their absence, will further constrain estimates of the recurrence rate of magmatism in the YMR. Finally, in the event that dikes can be mapped using magnetic methods, the extent and orientation of these dikes may be useful in constraining models of the interaction between structure and volcanism in the area, as well as the overall tectonic setting of the site.

Ponce et al. (1992) made six gravity and ground magnetic traverses across Fortymile Wash as a preliminary effort to map the extent of the Paintbrush Fault and in order to ascertain whether the wash in structurally controlled along most of its length (Figure 8-4). The source of the Fortymile Wash is north of Yucca Mountain at Fortymile Canyon. This canyon drains into Jackass Flats, a wide alluvial basin located east of Yucca Mountain. Fortymile Wash is a shallow incised feature transecting this basin and eventually empties into Amargosa Valley, south of Jackass Flat. It has been suspected that this wash may be structurally controlled, despite the lack of surface expression of a fault along most of the length of the wash, because of the linear nature of the wash and the coincidence of its trend with other mapped faults in the area (Huber, 1987; Ponce et al., 1992). Four of the six traverses of Ponce et al. (1992) are at, or north, of Busted Butte. As a result, ground magnetic traverses on these lines have steep and somewhat

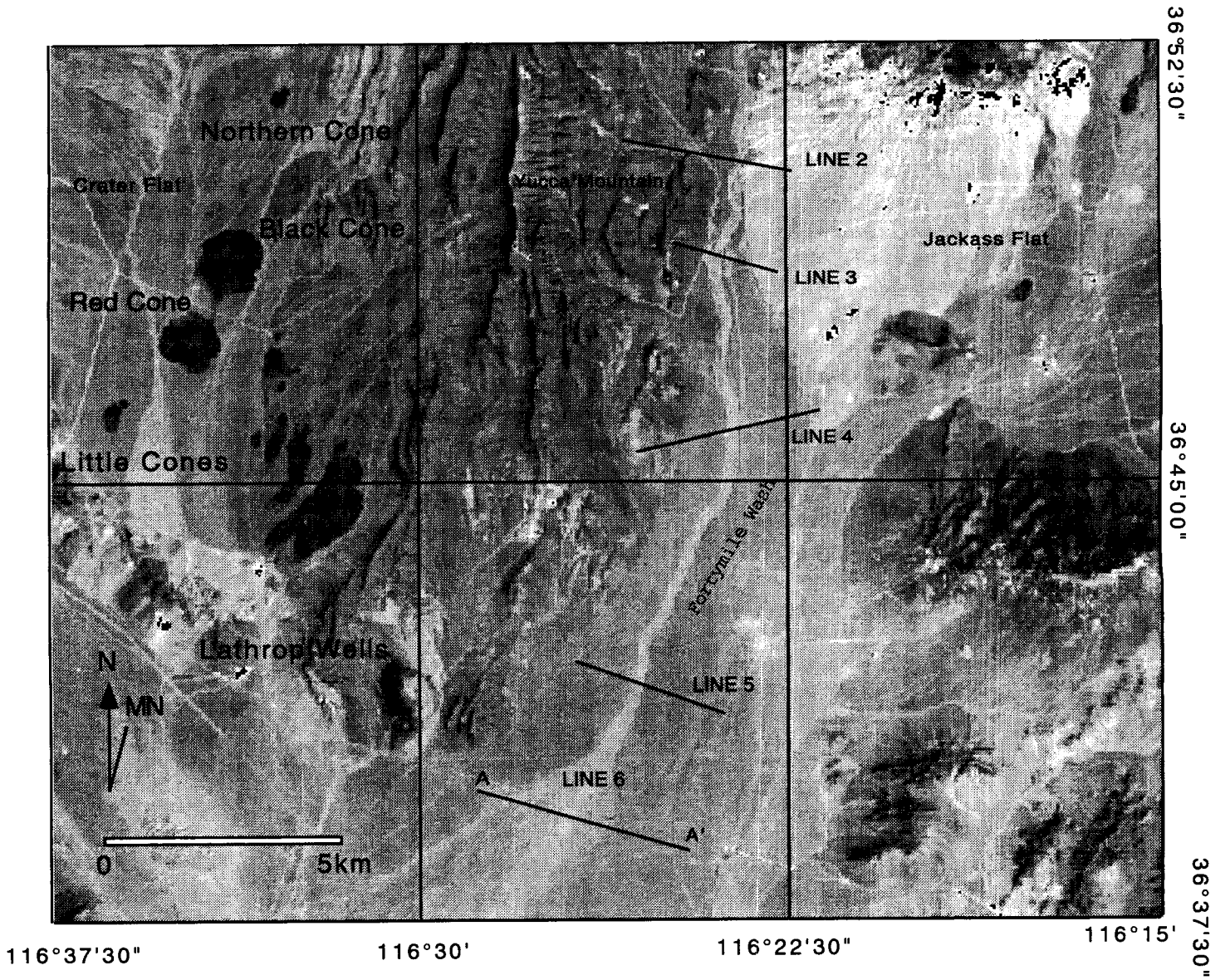

Figure 8-4. Locations of geophysical traverses surveyed by Ponce et al. (1992). Line 1 (not shown) is located North of Line 2 in Fortymile Canyon.

erratic gradients west of Fortymile Wash due to the shallow depth of alluvium and magnetization of the Paintbrush tuff. In contrast, lines 5 and 6, located south of Busted Butte, are located over thicker alluvium and are, comparatively, magnetically quiet.

Magnetic data collected along line 6 by Ponce et al. (1992) were digitized from graphs presented in their Appendix and are shown in Figure 8-5(a). Ponce et al. (1992) noted that pronounced large-amplitude and very short-wavelength magnetic anomalies appear to outline the wash along line 6, and suggested that these anomalies are likely produced by a continuous feature along the wash, possibly resulting from basaltic sediments deposited most recently in the wash. In the area of Line 6 the wash itself is topographically indistinct. Total elevation change along the traverse consists of a uniform and gradual increase from west to east of about 3.75 m/km. Ponce et al. (1992) concluded that additional profiles would be necessary in order to fully delineate any structural control on Fortymile Wash itself, or other related faults in the area.

Large-amplitude long-wavelength magnetic anomalies such as those associated with the Amargosa Valley centers do not occur in Jackass Flat along any of the lines surveyed. This produces an upper bound on the types and volumes of intrusive or buried extrusive volcanic features that could be concealed by alluvium in the area of the traverses. Large-amplitude short-wavelength anomalies, similar to those produced by individual dikes that nearly crop out at the surface, were identified along the traverses, but are readily explained by other features, such as the edge of the Fortymile Wash [Figure 8-5(a)]. Magnetic variation due to random variation in the magnetic properties of the alluvium is on the order of 10 nT, small compared with the horizontal gradients in the Tiva Canyon Tuff.

Magnetic data from line 6 of Ponce et al. (1992) can be used to illustrate the sensitivity of the ground magnetic response to the presence of dikes at repository depths (about 300 m), in alluvium. Initially, it was intended that the data along Line 6 be used as an example of the magnetic noise likely to be encountered in any traverse across volcaniclastic-rich alluvium. However, smoothing of the data indicates some structure in the variation in total field strength along the traverse. Plotting the midmean of the data (Tukey, 1977; Kleiner and Graedel, 1980) reveals a small positive anomaly centered on the wash with a wavelength of approximately 2 km [Figure 8-5(b)]. This anomaly is used here to illustrate the ground magnetic response to dikes at repository depths in alluvium.

This anomaly [Figure 8-5(b)] is of much longer wavelength than the anomalies discussed by Ponce et al. (1992) and may be result from a variety of sources. Variation in the magnetic properties of the basement rocks or faults cutting the basement and buried by alluvium are among the possible causes for this long-wavelength total magnetic field variation. Local topographic variation or abrupt changes in magnetization at shallow depths could not be reasonably responsible for an anomaly of this wavelength.

Given that Fortymile Wash trends at an azimuth of approximately 15°, and line 6 is orthogonal to the wash, a normally polarized dike could also produce the observed positive anomaly. Figures 8-6(a) and 8-6(b) show several models of the total field magnetic anomalies that dikes of varying depth and total magnetization would produce, together with the total field magnetic data collected by Ponce et al. (1992). In Figure 8-6(a), it is assumed that a dike trending parallel to the wash is buried beneath it at a depth of 250 m. The modeled dike is 5 m thick and extends to great depth. The dike is assumed to extend 5 km NE and SW of the traverse line, although the calculated anomaly is not sensitive to the dike length once it extends more than 1 km from line 6. Anomalies resulting from this geometry and three different total magnetization contrasts are illustrated in Figure 8-6(a). These contrasts are 10, 5, and 3 Am^{-1}, each producing successively lower-amplitude anomalies. These three models bracket the amplitude of the

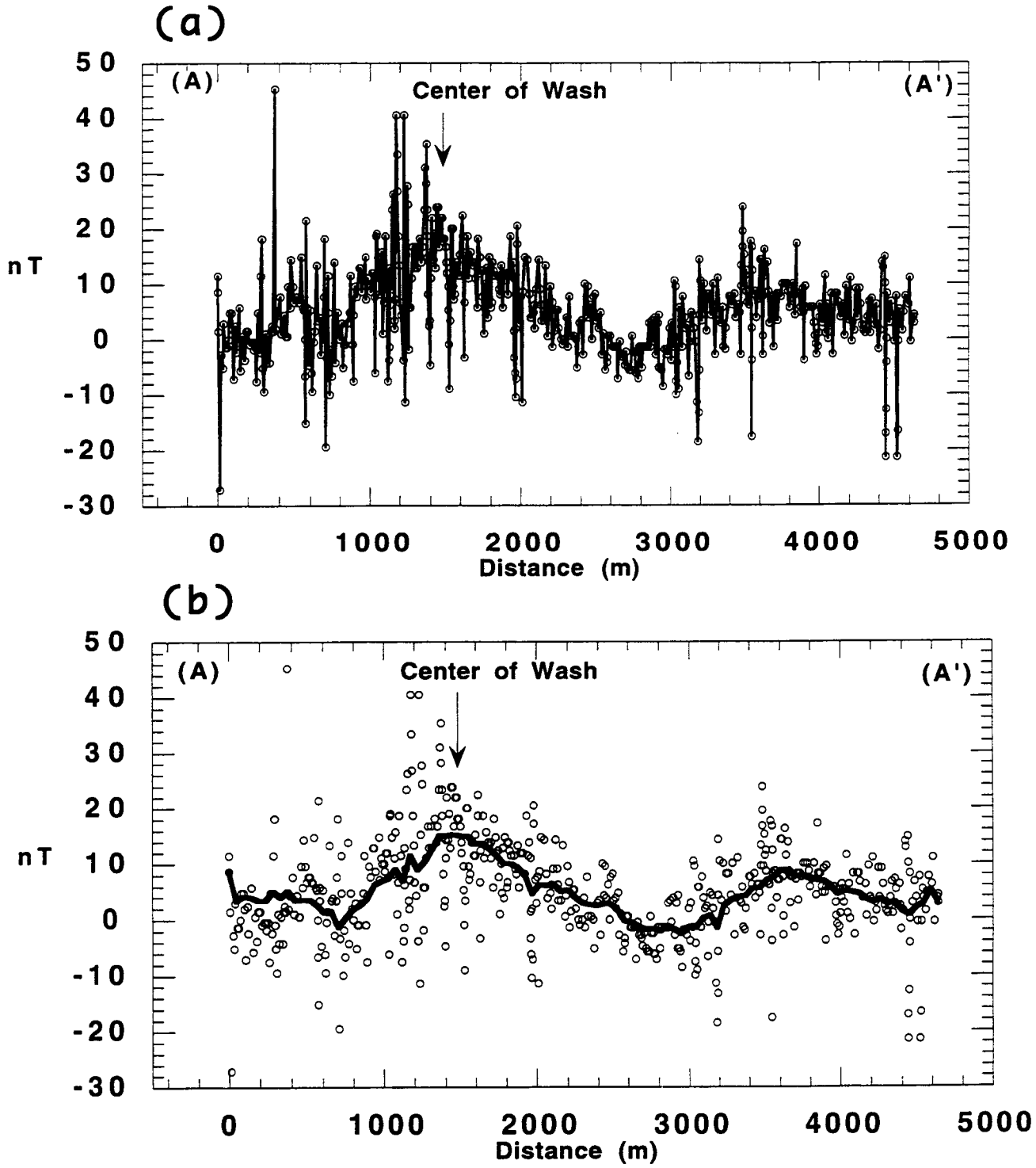

Figure 8-5. (a) Total field magnetic data collected along Line 6 (Figure 8-4) by Ponce et al. (1992); (b) smoothed magnetic anomaly along Line 6, calculated using the midmean approach of Tukey (1977). Open circles are data.

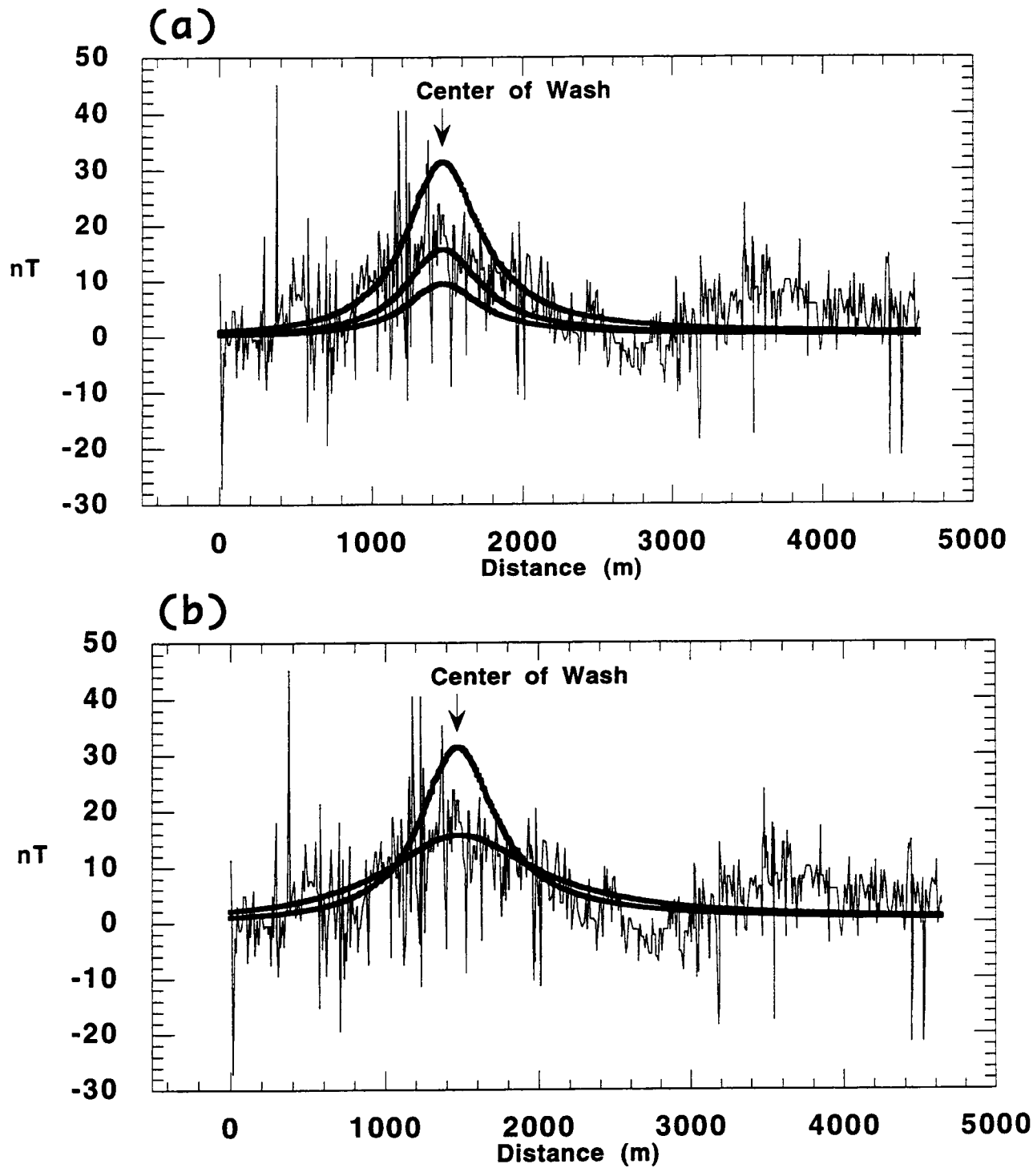

Figure 8-6. Observed total magnetic field variation along line 6 (Ponce et al., 1992) modeled with dikes of varying (a) magnetization, and (b) depth. See text for discussion of the model parameters.

observed change in total field well, with the exception of large-amplitude spikes in the observed data related to near-surface variation. The anomalies are also of comparable wavelength to the observed magnetic anomaly. Figure 8-6(b) shows the change in the calculated anomaly with change in depth to the top of the dike. The large-amplitude calculated profile in Figure 8-6(b) is the magnetic anomaly resulting from a total magnetization contrast of 10 Am^{-1} and depth to the top of the dike of 250 m. This is the same as the large-amplitude curve in Figure 8-6(a). Increasing the depth to the top of the dike from 250 m to 500 m and leaving other parameters unchanged produces the second, comparatively low-amplitude magnetic anomaly illustrated in Figure 8-6(b). This lower-amplitude curve provides a reasonable fit to the observed magnetic data in the vicinity of Fortymile wash.

It is clear that the observed anomaly on line 6 can be modeled using a variety of dike models, as well as other source geometries. The purpose of this exercise is not to suggest that a dike is buried at repository depths beneath line 6 in the Amargosa Valley, although the presence of dikes at these depths would not be surprising given the proximity of line 6 to aeromagnetic anomalies in the Amargosa Valley (Figure 8-4). Rather, the analysis is intended to illustrate the sensitivity of total magnetic field to the presence of dikes at repository depths in alluvium and to compare these calculated anomalies to measured anomalies located along traverses in the area. Ponce et al. (1992) point out that additional geophysical information can better constrain the tectonic setting of the YMR. Collection of ground magnetic data along closely spaced traverses may in fact help determine the significance and cause of small-amplitude, long-wavelength total magnetic field variation in Jackass Flats.

8.4 SUMMARY OF PARAMETRIC STUDY

The results of the parametric study indicate that practical bounds can be placed on the ability of aeromagnetic and ground magnetic data to identify basaltic dikes and other volcanic features. Based on ground magnetic data collected by Ponce et al. (1992) and Langenheim et al. (1993), it is apparent that the minimum amplitude anomaly likely to be resolved using ground magnetic data in alluvium in the YMR is one the order of 20–200 nT. This means that the magnitude of dipolar anomalies resulting from dikes or similar bodies needs to exceed this value. Ground magnetic anomalies with magnitudes greater than 200 nT will likely be recognized in alluvium under most circumstances; anomalies with amplitudes greater than 30 nT may also be recognized in alluvium, but only under fortuitous circumstances, such as where the alluvium is very thick and magnetically homogeneous. Anomalies with magnitudes smaller than these values will likely be obscured by magnetic variations in the alluvium, by regional anomalies, and will be too difficult to interpret unambiguously. Similarly, high-frequency and large-amplitude fluctuations in ground magnetic data on the Paintbrush tuff (Ponce et al., 1992) indicate that anomalies would normally need to exceed several thousand nanoTeslas in order to be identified unambiguously.

This analysis provides a basis for bounding the geometries of dikes readily identified in intruding rocks and sediments in the YMR using interpretations based on magnetic observations. Figure 8-7(a) shows the magnitude of anomalies expected for igneous dikes as a function of depth, thickness, and orientation, given a normal polarization and $J_{tot} = 10$ Am^{-1}. Figure 8-7(b) shows the likely magnitude of a magnetic anomaly for constant dike thickness and varying magnetization contrast. These curves provide a sense of the sizes of basaltic dikes likely to be identified in alluvium and tuff. For example, in some circumstances it may be difficult to identify anomalies with amplitudes of less than 100 nT in alluvium. Under these conditions, it will be possible to map a relatively wide, 10-m, E-W trending dike that reaches to within approximately 200 m of the surface. The same dike, oriented N-S, would need to reach a shallower depth before it could be mapped with confidence [Figure 8-7(a)].

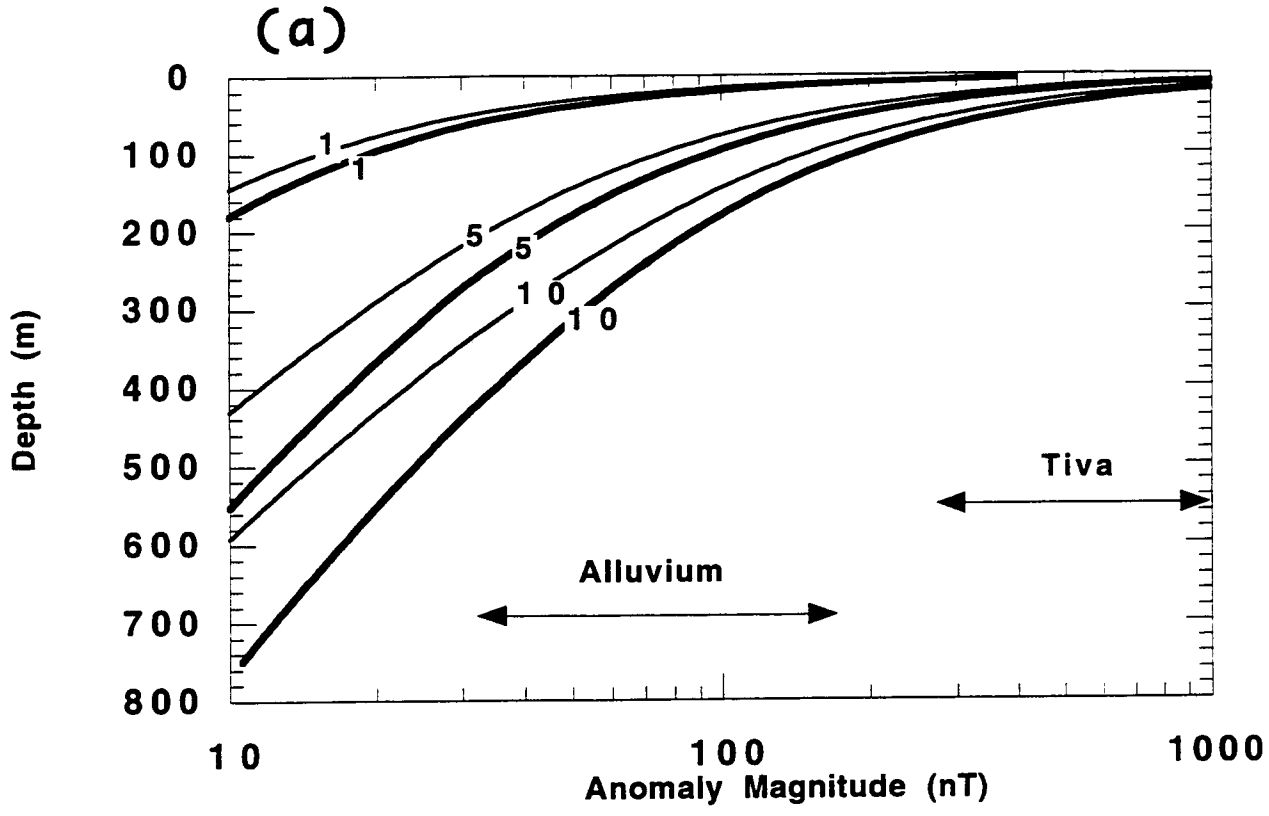

Figure 8-7a. Magnetic anomaly magnitude as a function of depth for 1-, 5-, and 10-m thick dikes. Dikes are normally polarized, have a total magnetization of 10 Am^{-1} and are oriented E-W (heavy lines) and N-S (light lines). The range of minimum anomaly magnitudes necessary to identify the anomaly are indicated for alluvium and Tiva Canyon tuff. Under excellent circumstances in alluvium, the minimum amplitude for an anomaly to be recognized unambiguously is on the order of 30 nT, and may need to be as high as 200 nT if the alluvium is comparatively noisy. Anomalies produced by basaltic dikes would need to have exceptional magnitudes to be identified in the Tiva Canyon or other tuffs having similar magnetic properties.

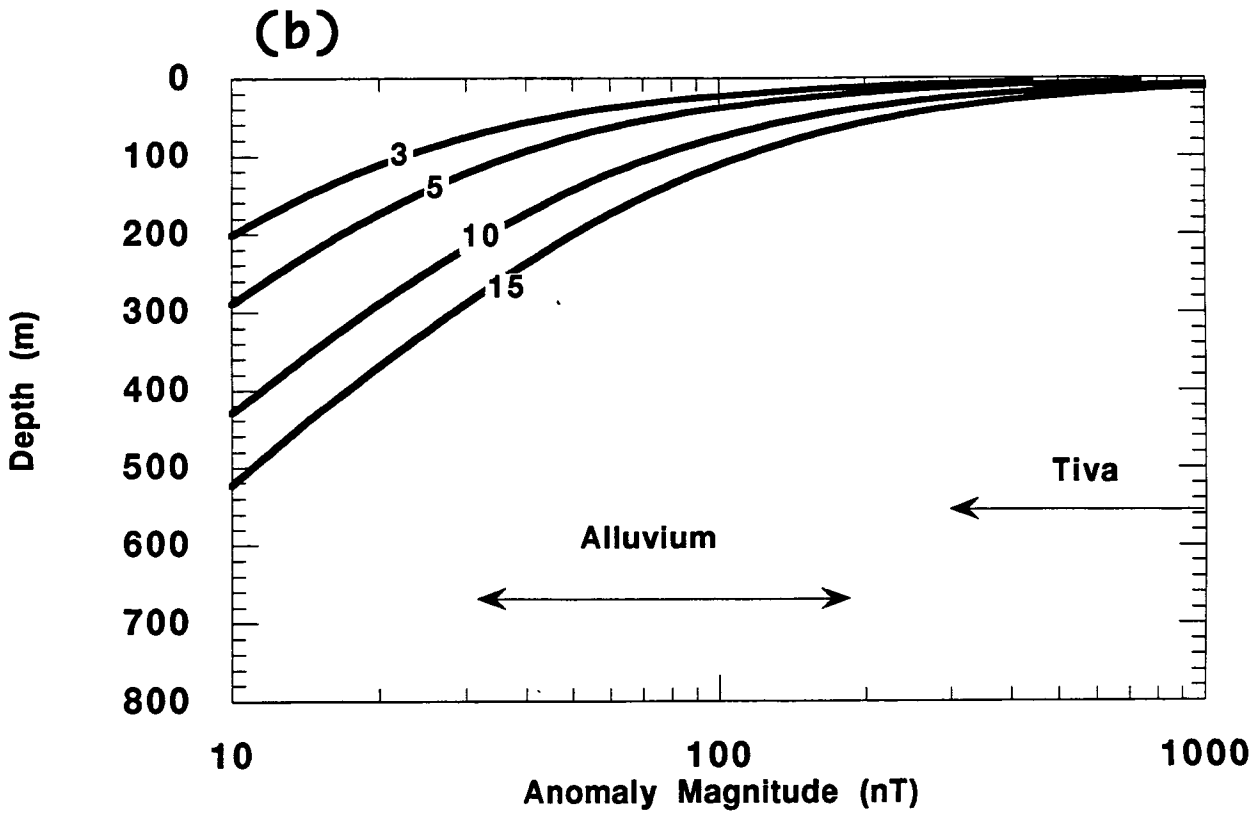

Figure 8-7b. Magnitude of magnetic anomalies resulting from 5-m wide, normally polarized, E-W trending vertical dikes with varying magnetization contrasts. Curves are calculated for magnetizations of 3–15 Am^{-1}. The range of minimum anomaly magnitudes necessary to identify the anomaly are indicated for alluvium and Tiva Canyon tuff. Under excellent circumstances in alluvium, the minimum amplitude for an anomaly to be recognized unambiguously is on the order of 30 nT, and may need to be as high as 200 nT if the alluvium is comparatively noisy.

However, a more typical dike width is 1 m. A 1-m-wide dike must reach to E-W-trending within 20 m of the surface before it is likely to be identified from ground magnetic data. In Tiva Canyon Tuff, it is unlikely that any dike could be mapped due to the magnetic properties of the tuff, unless that dike reaches to within several meters of the surface. This limit in the resolution of magnetic data needs to be considered when attempting to estimate the number or volume of basaltic features in the YMR.

9 TOPOGRAPHIC EFFECTS AND MAGNETIC ANOMALIES NEAR CINDER CONES

Identification of dikes, or dike complexes, associated with cinder cones and cinder cone alignments is important to site characterization and development of an understanding of basaltic volcanism in the YMR. Characterization of dike geometries may provide insight into the area of the repository that would be affected by dike injection during magmatic events. Furthermore, dike geometries beneath cinder cone alignments, like the Crater Flat alignment, may improve our understanding of the evolution of these structures. For example, the presence of continuous, or nearly continuous, dikes beneath the Crater Flat cinder cone alignment may indicate that this alignment should be treated as a single, large and long-duration volcanic event in probability models, rather than as a series of discrete events. Magnetic methods have been suggested as a means of identifying dikes beneath the Crater Flat alignment (Crowe et al., 1993). However, terrain effects complicate the interpretation of magnetic data in basaltic volcanic fields. Terrain effects are particularly important if the goal of the survey is to resolve dikes and similar igneous features beneath cinder cones and lava flows which carry substantial magnetic signatures themselves. Therefore, it is important to bound the limits of magnetic methods for delineating these dikes and dike swarms where they are overlain by magnetized cinder cones, lava flows, and related structures.

Numerous investigators have noted the importance of identifying terrain effects in ground magnetic and aeromagnetic data (Clarke, 1971; Marsh, 1971; Plouff, 1976; Bhattacharyya and Chan, 1977; Grauch and Campbell, 1984; Grauch, 1985). Early approaches involved assigning a uniform magnetization to an entire region and calculating the resulting total field anomaly solely due to topography (e.g., Marsh, 1971). Plouff (1976) recommended assigning varying magnetic properties to areas within a study region and incorporating this into a terrain correction, making it more analogous to terrain corrections to gravity data that account for variable surface rock density in the Bouguer correction. This method was adapted by Blakely (1981) and a similar approach was used by Blakely and Grauch (1983) to interpret magnetic anomalies over crystalline basement. Other methods, such as those of Clarke (1971) and further developed by Grauch and Campbell (1984) and Grauch (1985), use statistical techniques to identify cross-correlation between magnetic anomalies and topography. Grauch (1985) recommends statistical methods to reduce regional magnetic data to account for highly variable rock magnetizations and where target anomalies might be located at variable depths. In large regions, such as the YMR, a statistical approach (Grauch, 1985) should be adopted. However, in situations where the magnetic properties of rocks are not likely to be highly variable and the topography of the area is comparatively simple, Grauch (1985) recommends the calculation of synthetic magnetic terrain maps, essentially following the approach of Plouff (1976), rather than statistical methods. Application of fractal and stochastic approaches to modeling magnetic terrain effects (Gregotski et al., 1991) also have great potential for application to data collected in volcanic fields, where magnetic gradients are high and difficult to interpret deterministically in sufficient detail.

9.1 MAGNETIZED TERRAIN EXPERIMENT

A numerical experiment was constructed to assess the impact of magnetized terrain on magnetic anomalies associated with shallow dikes in basaltic volcanic fields. A synthetic magnetic anomaly map was calculated following the approach of Plouff (1976). All magnetic calculations were performed using the algorithm of Rao and Babu (1991).

Quaternary cinder cones in Crater Flat Valley were used in the experiment. These include Black, Red and the two Little Cones [Figure 9-1(a)]. These four cinder cones lie on a gently sloping alluvial surface in Crater Flat valley. Magnetic terrain effects were calculated over a 7.3×7.3-km area, centered on Red Cone. Within this region, the elevation of the alluvial surface changes from approximately 900 m above sea level in the south to 1,060 m in the northeast. Red Cone and Black Cone are the two most prominent topographic features within this area. These cones have relief of approximately 80 and 110 m above the surrounding alluvium, respectively. Both cinder cones are surrounded by lava flows, especially on their downslope (south) sides. Smith (1994) mapped the geology of these cones and their surrounding lava flows in detail. The two Little Cones, located approximately 4 km southwest of Red Cone, have relief of 20 to 30 m and also have lava flows about them. Together, these cinder cones form a NE-trending alignment. Given their similarity in age (Crowe et al., 1993; Hill et al., 1993) and aligned nature, it has been suggested by Smith et al. (1990) and Crowe et al. (1993) that these cinder cones are structurally controlled, either because dikes feeding the cinder cones are controlled by a buried fault zone as they ascend from depth, or because dikes are emplaced in a NE-trend due to regional stress state. A fifth cinder cone in this alignment, Northern Cone, is located north of the study region.

For purposes of the terrain effects experiment, the relief of the four cinder cones above the local alluvial surface was quantified using a 30-m^2 digital elevation model (DEM) (Connor and Hill, 1994). Subtracting regional elevation of the alluvial surface from the DEM data outlines the topographic expression of Red and Little Cones and their lava flows, where the lava flows are more than 5 m thick. The resulting surface agrees well with the maps of Smith (1994) because the flows associated with Red and Black Cones are generally more than 5 m thick. Topographic relief of the Little Cones also was determined in this manner. However, because the lava flows near the Little Cones lack significant topographic expression, the magnetic anomalies associated with these flows were neglected in the analysis.

Several other geologic features in the area have significant magnetizations with respect to alluvium, including Yucca Mountain, Bare Mountain, and the Pliocene lava flows in eastern Crater Flat. These features likely affect aeromagnetic data, but their effects are not included in the calculation of magnetic terrain effects.

Numerous age determinations on the four cinder cones in the study area consistently indicate that they are Matuyama in age (Crowe et al., 1993; Hill et al., 1993), and therefore are reversely polarized. It is assumed that most of the magnetization in these rocks is carried as thermo-remanent magnetization and that the total magnetization vector has a magnitude of 10 Am^{-1}, average for a basalt, inclination $-6°$ and declination 180°. Lava flows and cinder cones are assumed to carry the same magnetization vector. In reality, several factors likely complicate the magnetization of these rocks. Although most of the lava flows do likely carry a uniform remanent magnetization, some parts of the flow field may have experienced considerable rotation after the flow cooled below the blocking temperatures for minerals in these flows (Flanigan and Long, 1987). This rotation results in a more complex magnetic anomaly pattern. Also, brittle cinders in the cones, deposited cool during the eruption, will not carry a significant remanent magnetization. Agglutinated spatter, lava lakes, such as the lava lake in the crater of Black Cone (Smith et al., 1990), and rheomorphic flows present within the cone, however, will carry significant remanent magnetization. These details add considerable complexity to the aeromagnetic anomalies associated with these volcanoes. However, because of the large volume of flows and spatter at these volcanoes compared to cinders, the assumption of a uniform magnetization vector seems reasonable.

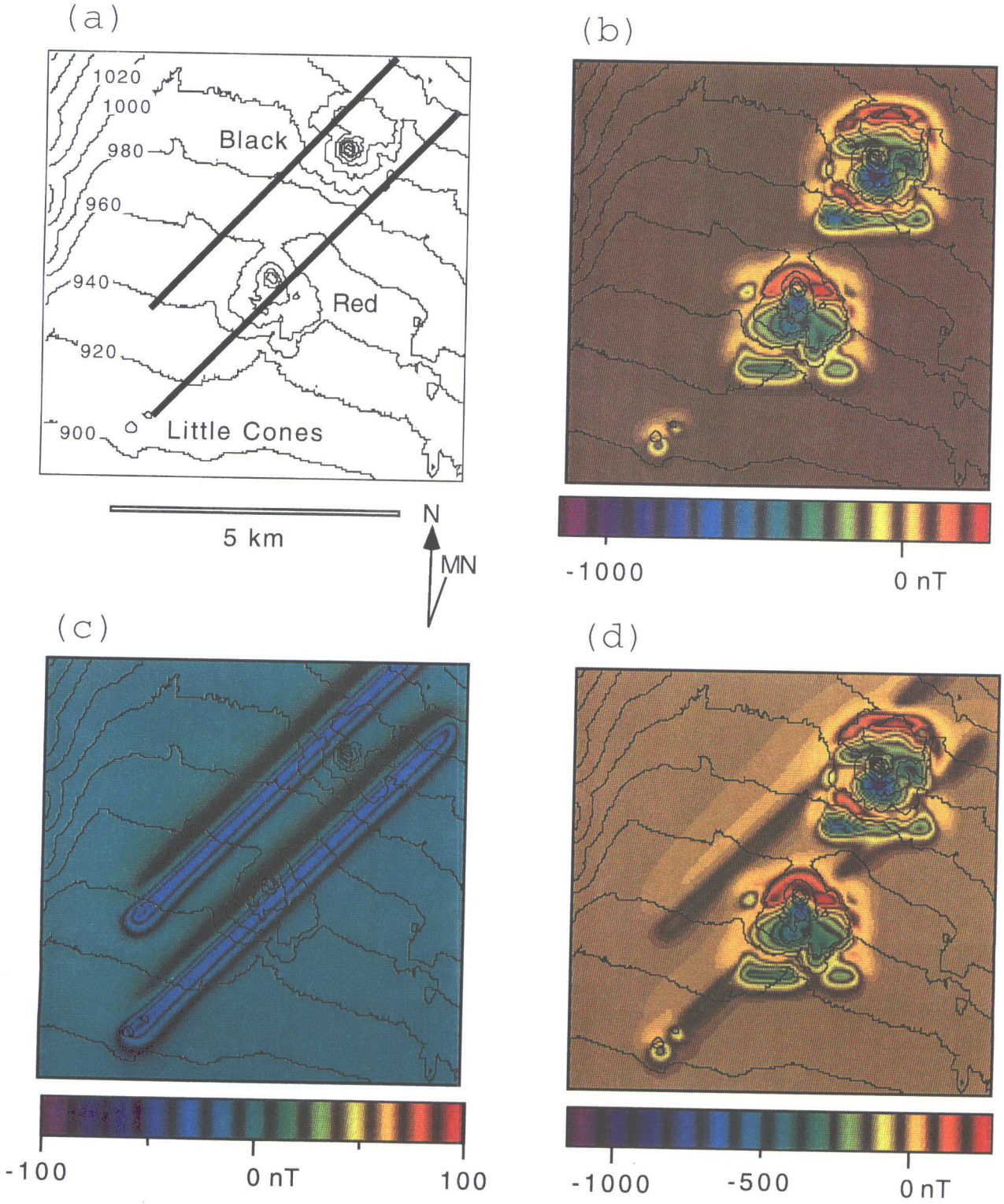

Figure 9-1. (a) Topography and dike geometry used in the experiment, (b) magnetic terrain effect, (c) magnetic anomalies due to the dikes, and (d) the total field anomaly due to the magnetized topography and dikes. See text for discussion of model assumptions and parameters.

The alluvium in Crater Flat is assumed to be magnetically transparent, although the alluvium likely carries a magnetization similar to that observed in Jackass Flat (Ponce et al., 1992). This assumption is based on the observation that the magnetization of alluvium is small compared with that associated with the cinder cones.

A uniform magnetization vector was assigned to each 30-m^2 cell in which the elevation was greater than 5 m above the surrounding alluvium at one of the four cinder cones. A total of 5,743 of the DEM cells in the study region met these criteria and were assigned uniform basalt magnetization vectors. Individual cell thicknesses ranged from 5 m at flow margins to 117 m at the center of Black Cone. Each of these cells was represented as a parallel-sided vertical prism of magnetized rock. The total field magnetic anomaly was determined by summing the magnetic anomalies associated with each of these 5,743 prisms. The magnetic anomaly due to this terrain was calculated on a 100-m^2 grid (73×73 grid points), assuming a flight elevation of 150 m above the alluvium. Thus, the aeromagnetic survey is assumed to be flown draping the topography, rather than at a constant flight elevation. Draped aeromagnetic surveys have been standard practice most recently in the area (Oliver et al., 1990). The flight elevation assumed in the terrain experiment is also comparable to recent aeromagnetic surveys flown in the YMR. The flight elevation is constant with respect to the alluvial surface, meaning that the hypothetical flight line passes a mere 33 m above the crater of Black Cone.

The resulting total magnetic field map is shown in Figure 9-1(b). Complex, large-amplitude magnetic anomalies are associated with both Red and Black Cones. The total magnitude of these anomalies, approximately 1,500 nT, is attributed to the volume of the cones and is large because the flight line, 150 m above the surrounding alluvium, passes within 30–60 m of the top of each cone. The anomalies are mostly negative because the cones are reversely magnetized and a steeply dipping remanent magnetization is assumed to dominate the total magnetization vector. At this low flight elevation, the anomalies associated with the cinder cones extend only a short distance, on the order of 250 m, beyond the map extent of the lava flows. Much smaller anomalies are associated with the Little Cones, primarily because of the small volume of these cinder cones and their low topographic relief.

Magnetic anomalies were then calculated for two hypothetical dikes to assess the impact of magnetized terrain on anomalies associated with feeder dikes related to these cones. The map extent of these dikes is shown in Figure 9-1(a). It is assumed that the dikes have the same magnetization as the basaltic lava flows and cones. The dikes have a uniform thickness of 5 m and the tops of both dikes are a constant 25 m below the alluvial surface. Note that the dikes used in this experiment are thick and shallow along their entire map extent. Actual feeder dikes may have a more limited map extent and variable depth. The dike geometry chosen serves to maximize the magnitude of the magnetic anomalies. Also, the continuous nature of the dikes between the cinder cones tends to maximize the map extent of the anomaly. In these respects, the hypothetical dikes shown here are similar to the Fortification Hills dikes, which crop out over a distance of several kilometers south of Fortification Hill, a series of basaltic flows on the south side of Lake Mead[4]. Again, it is emphasized that, although the dikes used in this experiment are geologically tenable, in reality dikes beneath the Crater Flat alignment might not be continuous between cinder cones, as large, or as shallow as the dikes depicted in this model.

---

[4] J. Mills. 1993. Written Communication to B. Hill. Center for Nuclear Waste Regulatory Analyses. San Antonio, Texas.

The magnetic anomalies at a flight elevation 150 m above the alluvial surface associated with these hypothetical dikes is shown in Figure 9-1(c). The anomalies have a total magnitude of approximately 50 nT and a simple form. The anomalies are dominantly negative, again due to the steep inclination assumed for the remanent magnetization vector.

The combined magnetized terrain and dike anomalies are plotted in Figure 9-1(d). As expected, the anomalies associated with the two dikes are quite subtle compared to those associated with the cinder cones. Naturally, the magnetic anomalies associated with the dikes are completely obscured close to and beneath the cinder cones. Far from the cinder cones, the magnetic anomalies associated with the dikes remain visible.

Recall several of the assumptions used in the model. First, it was assumed that the alluvium has a uniform and inconsequential magnetization. Any nonuniform character to the magnetization in the alluvium will complicate the aeromagnetic map further, making interpretation of low-amplitude anomalies, such as those associated with the dikes, more tenuous. Second, it was assumed that only the cinder cones carry a substantial magnetization in the area. However, buried lava flows, particularly those of Pliocene age, will also complicate the magnetic map and make interpretation of anomalies in terms of intrusive structures a difficult task. It is difficult to identify intrusive structures associated with cinder cones, even in the best of circumstances, using magnetic methods.

9.2 ENHANCING MAGNETIC DATA

Clearly, magnetic anomalies associated with dikes located beneath cinder cones, at best, will be difficult to identify. Under such circumstances, map enhancement techniques are often applied to bring out features, in this case dike anomalies, that are otherwise indistinct (Hildenbrand, 1983). One common approach to analysis of complex magnetic maps is through digital filtering. Digital filtering and enhancement techniques are widely used (Hinze, 1985) to make the interpretation of magnetic maps more straightforward. The simplest filtering techniques involve the application of the 2D Fast Fourier Transform (FFT). Using 2D FFTs it is possible to remove magnetic anomalies to the magnetic pole, and perform bandwidth filtering and directional filtering. Other filters include upward and downward continuation, which provide a simple method for comparing aeromagnetic maps created using different flight elevations, and in some cases differentiating between anomalies produced by shallow bodies from those related to deeper sources.

Magnetic data can be analyzed from a variety of perspectives by transforming it from the spatial domain into the frequency domain, filtering it, then calculating the inverse FFT to transform the data back into the spatial domain. All Fourier transforms are based on the Fourier series, which describes any function or signal as the sum of an infinite number of sine and cosine functions, each with an increasingly high frequency, of varying phase and amplitude. The FFT is a mathematical algorithm that makes frequency filtering computationally efficient (Cooley and Tukey, 1965). The application of the 2D FFT in map filtering was first discussed by Cote et al. (1962), and subsequently has been applied to numerous geophysical investigations (e.g., Hildenbrand, 1983; Hinze, 1985). Dobrin and Savit (1988) review map filtering of potential field data in detail and discuss the limitations of the method.

Here, 2D FFT map filtering was applied to the calculated magnetic anomalies resulting from magnetized topography and two hypothetical dikes in the experimental region around Red, Black, and Little Cones [Figure 9-2(a)]. The goal of this analysis is to determine whether map enhancement through

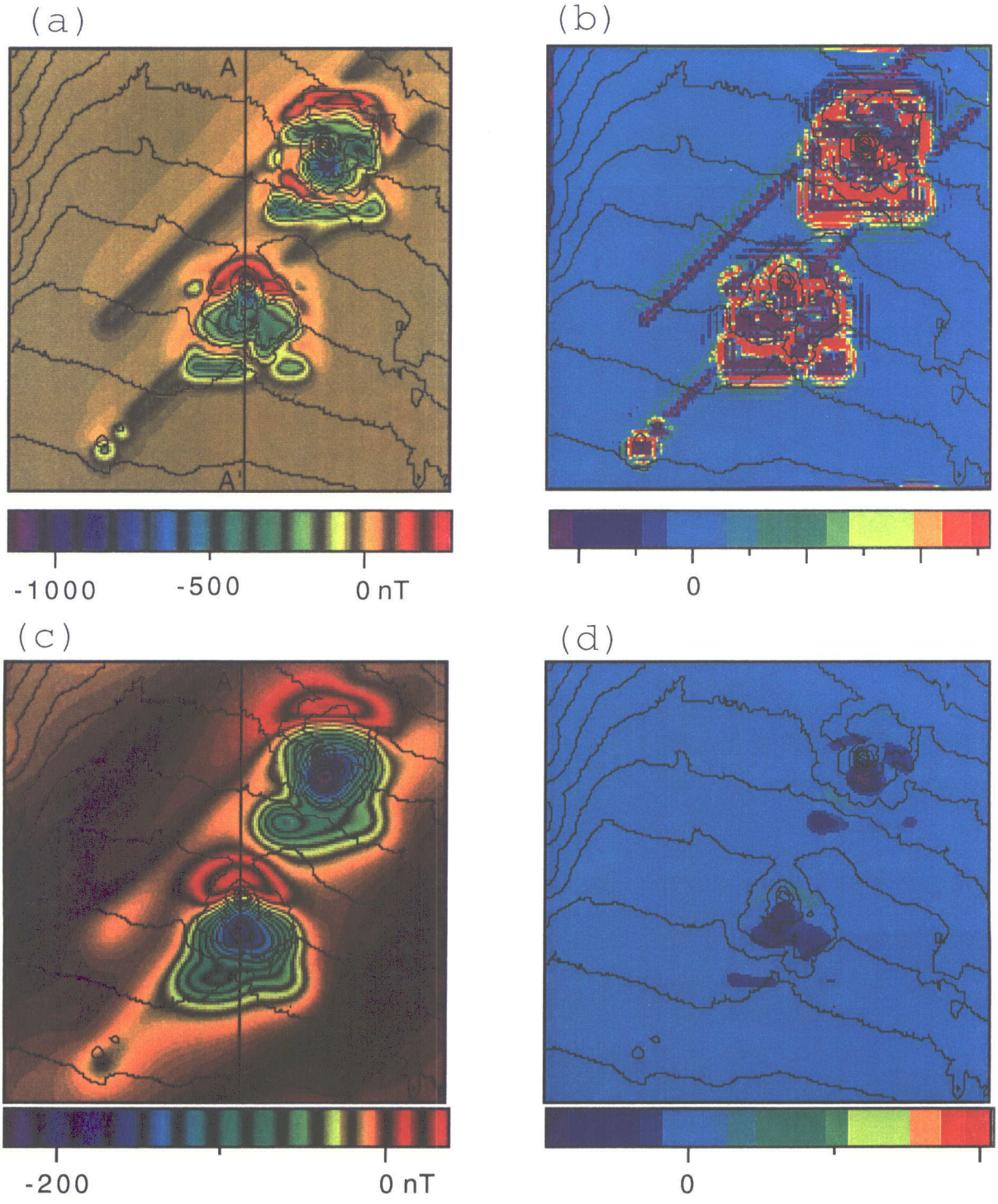

Figure 9-2. (a) Magnetic anomaly map due to magnetized topography and dikes, (b) the second vertical derivative of the magnetic anomaly map, (c) upward continuation of the magnetic anomaly map, and (d) second vertical derivative of upward continuation of the magnetic map

2D FFT filtering can result in better resolution of the two hypothetical dikes beneath these cinder cones [Figure 9-1(a)].

Briefly, any matrix, in this case the 73×73 grid calculated for the magnetized topography and dikes, can be transformed into the frequency domain using a discrete 2D FFT. This transform is written as:

$$F(k_x,k_y) = \int_{-\infty}^{\infty}\int_{-\infty}^{\infty} f(x,y)\cos(k_x x + k_y y)\,dx\,dy - \int_{-\infty}^{\infty}\int_{-\infty}^{\infty} f(x,y)\sin(k_x x + k_y y)\,dx\,dy \tag{9-1}$$

where k_x and k_y are wavenumbers in the x and y directions, respectively and have units of cycles per unit distance, and $f(x,y)$ is the matrix containing the calculated magnetic field data. Initially, $f(x,y)$ is a real discrete function in two dimensions. In the frequency domain this discrete function is completely described by real and imaginary, i, components. In practice, the 73×73 matrix was interpolated to 128×128 to increase the speed the transformation of the discrete function in the spatial domain into the frequency domain.

The transformed function $F(k_x,k_y)$ can then be multiplied by a filter $H(k_x,k_y)$ to enhance specific aspects of the magnetic data. For example, it is simple to calculate the second vertical derivative of the magnetic map by constructing the filter (Gunn, 1975) such that:

$$H(k_x,k_y) = (-k)^2 \; ; \; \left[k = \sqrt{k_x^2 + k_y^2}\right] \tag{9-2}$$

and

$$G(k_x,k_y) = F(k_x,k_y)\,H(k_x,k_y) \tag{9-3}$$

The inverse 2D FFT of G is then calculated:

$$\begin{aligned} g(x,y) = \frac{1}{2\pi} &\int_{-\infty}^{\infty}\int_{-\infty}^{\infty} G(k_x,k_y)\cos(k_x x + k_y y)\,dx\,dy \\ &+ \frac{i}{2\pi}\int_{-\infty}^{\infty}\int_{-\infty}^{\infty} G(k_x,k_y)\sin(k_x x + k_y y)\,dx\,dy \end{aligned} \tag{9-4}$$

to produce the second vertical derivative of the original data set.

The second vertical derivative is essentially a difference between the total magnetic field values at a given grid point and those at surrounding grid points. Thus the second vertical derivative map has the effect of emphasizing steep gradients and attenuating longer wavelength terms in the magnetic data. In effect, the second vertical derivative is a smooth high-frequency bandpass filter, which enhances shallow local anomalies, at the expense of longer wavelength, deeper anomalies (Gunn, 1975; Hildenbrand, 1983).

The second vertical derivative of the terrain and dike anomaly map [Figure 9-2(a)] is shown in Figure 9-2(b). The areal extent of lava flows and the shallow dikes are well delineated on the second vertical derivative map. Although the gradient in the magnetic field about the dikes is small compared with the cones, it is nonetheless substantial enough so that the dike trends are well delineated by this map enhancement technique. In particular, note that the continuity of the dike between Red and Black Cones can be inferred from the second vertical derivative map. Although the magnetic anomaly due to the dike is small compared to the lava flows between the cinder cones, the gradient due to the dike is large.

Several factors can act to complicate the magnetic anomaly map and make it more difficult to identify the dikes, even with the aid of map enhancement techniques. These include magnetic variation in the alluvium, and variation in depth of the basement or magnetic properties of the basement. Dikes may still be identifiable given these factors, provided the dikes are shallow and produce anomalies of wavelengths different from those related to alluvial and basement variations.

Higher flight elevations of the aeromagnetic survey will also strongly impact the ability to identify shallow dikes. To illustrate the impact of higher flight lines, the magnetic map in Figure 9-2(a) was upwardly continued to an elevation of 450 m above the alluvium. This flight elevation corresponds to that of a more regional survey (Oliver et al., 1990). The upward continuation was also done in the frequency domain. The filter used for upward continuation is:

$$H\left(k_x,k_y\right) = e^{-kz} \; ; \left(k = \sqrt{k_x^2 + k_y^2}\right) \tag{9-5}$$

where z is the distance of upward continuation in map units. Anomalies associated with the cinder cones have a lower amplitude and longer wavelength as a result of the upward continuation [Figure 9-2(c)]. As a result, the anomalies associated with the cones envelop much of the anomalies related to the two dikes. Calculation of the second vertical derivative of the upwardly continued map [Figure 9-2(d)] does not provide further definition of the dikes, because the magnetic gradients associated with the dikes are not distinct relative to the gradient resulting from the cinder cones and flows.

The effect of flight elevation is further illustrated by comparison of individual flight lines. A N-S trending flight line transecting Red Cone is shown in Figure 9-2(a). Magnetic variation is plotted for line A-A' in Figure 9-3(a). The magnetic anomaly (1,100 nT) associated with Red Cone dominates the profile. But, a 50-nT magnitude anomaly is associated with the northernmost of the dikes. Upward continuation from 150 to 450 m above the alluvium greatly subdues the magnitude of the Red Cone anomaly (200 nT) [Figure 9-3(b)], and renders the anomaly associated with the dike completely indistinct.

9.3 SUMMARY OF THE MAGNETIC TERRAIN AND MAP ENHANCEMENT STUDIES

Large and shallow dikes or dike complexes produce aeromagnetic anomalies on the order of tens of nanoTeslas on low flight line, draped aeromagnetic surveys. These anomalies can be completely obscured by magnetized terrain, such as cinder cones and lava flows. However, magnetic anomalies associated with cinder cones are of short wavelength as observed in low-level aeromagnetic or ground magnetic surveys. In fortuitous circumstances it may be possible to identify dikes at distances greater than approximately 100 m from the cinder cones and flows. These anomalies can be enhanced by calculating the second vertical derivative of the total magnetic field data. In the terrain effects experiment, the second vertical derivative of simulated low-level aeromagnetic data over the Crater Flat alignment captured the

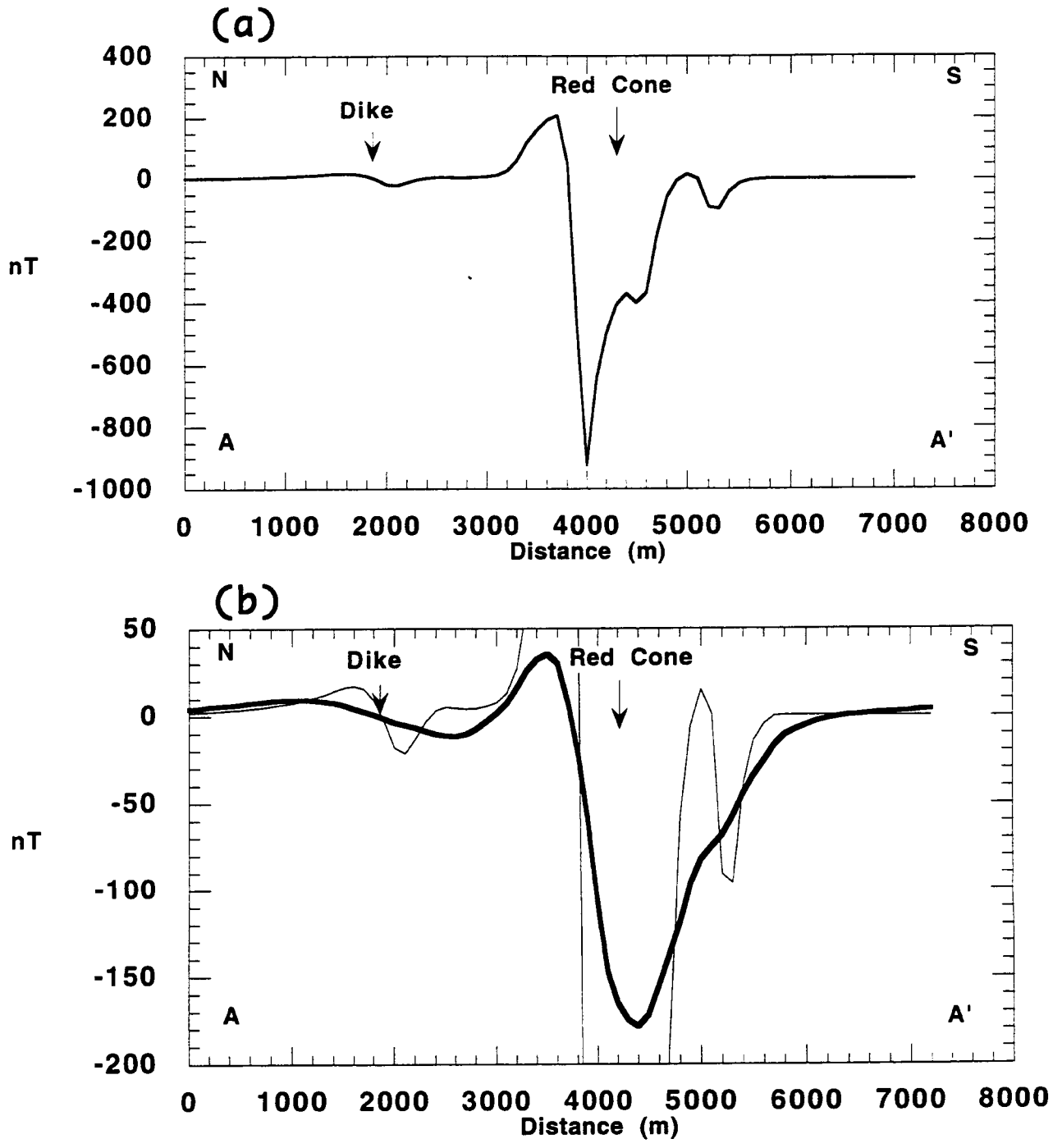

Figure 9-3. (a) Magnetic anomalies along a 150-m flight line [see Figure 9-2(a)], and (b) magnetic anomalies along a 450 m flight line [see Figure 9-2(c)]. The anomalies associated with a 150-m flight line are plotted (light line) at the same scale as the higher altitude survey (heavy line) in *b*. The attenuation of the anomaly associated with the shallow dike is evident.

map extent of two hypothetical dikes placed near the cones. Upward continuation indicates that even these anomalies are not detectable in data collected at higher flight elevations. Map enhancement techniques are not successful for interpretation of data collected at these elevations. The upward continuation data, coupled with parametric studies, place a practical limit on the sizes and depths of dikes that can be detected using magnetic methods in basaltic volcanic fields. Additional analysis could include application of a stochastic approach for depiction of magnetic variation in alluvium and lava flows to aid in the detection of shallow igneous features.

10 REFERENCES FOR MAGNETIC METHODS

Am, K. 1972. The arbitrarily magnetized dyke: Interpretation by characteristics. *Geoexploration* 10: 63–90.

Andrew, J.A., D.M. Edwards, R.J. Graf, and R.J. Wold. 1991. Empirical observations relating near-surface magnetic anomalies to high-frequency seismic data and Landsat data in eastern Sheridan County, Montana. *Geophysics* 56: 1,553–1,570.

Arkani-Hamed, J., and G. Celetti. 1989. Effects of thermal remanent magnetization on the magnetic anomalies of intrusives. *Journal of Geophysical Research* 94: 7,364–7,378.

Babu, H.V.R., A.S. Subrahmanyam, and D.A. Rao. 1982. A comparative study of the relation figures of magnetic anomalies due to two-dimensional dike and vertical step models. *Geophysics* 47: 926–931.

Babu, H.V.R., V. Vijayakumar, and D.A. Rao. 1986. A simple method for the analysis of magnetic anomalies over dike-like bodies. *Geophysics* 51: 1,119–1,126.

Bath, G.D., and C.E. Jahren. 1984. *Interpretations of Magnetic Anomalies at a Potential Repository Site Located in the Yucca Mountain Area, Nevada Test Site*. USGS Open-File Report 84-120. Reston, VA: U.S. Geological Survey.

Bhattacharyya, B.K., and K.C. Chan. 1977. Reduction of magnetic and gravity data on an arbitrary surface in a region of high topographic relief. *Geophysics* 42: 1,411–1,430.

Bhattacharyya, B.K., and L. Leu. 1975. Spectral analysis of gravity and magnetic anomalies due to two-dimensional structures. *Geophysics* 40: 993–1,013.

Bhattacharyya, B.K. 1964. Magnetic anomalies due to prism-shaped bodies with arbitrary polarization. *Geophysics* 29: 517–531.

Blakely, R.J. 1981. *A Program for Rapidly Computing the Magnetic Anomaly Over Digital Topography*. USGS Open-File Report 81-298. Reston, VA: U.S. Geological Survey.

Blakely, R.J., and V.J.S. Grauch. 1983. Magnetic models of crystalline terrane: accounting for the effect of topography. *Geophysics* 48: 1,551–1,557.

Blakely, R.J., and R.W. Simpson. 1986. Approximating the edges of source bodies from magnetic or gravity anomalies. *Geophysics* 51: 1,494–1,498.

Blakely, R.J., R.C. Jachens, and E.H. McKee. 1989. The northern Nevada rift: A 500 km long zone that resisted subsequent deformation. *Eos, Transactions of the American Geophysical Union* 70: 1,336.

Botezatu, R., and C. Calota. 1973. Cross-correlation as an aid in simultaneous gravity and magnetic analysis. *Geophysical Prospecting* 21: 472–483.

Bruckshaw, J.M., and K. Kunaratam. 1963. The interpretation of magnetic anomalies due to dykes. *Geophysical Prospecting* 11: 509–522.

Byerly, P.E. 1965. Convolution filtering of gravity and magnetic maps. *Geophysics* 30: 281–283.

Cady, J.W. 1980. Calculation of gravity and magnetic anomalies of finite length right polygonal prisms. *Geophysics* 45: 1,507–1,512.

Chandler, V.W., and K.C. Malek. 1991. Moving-window Poisson analysis of gravity and magnetic data from the Penokean orogen, east-central Minnesota. *Geophysics* 56: 123–132.

Chenot, D., and N. Debeglia. 1990. Three-dimensional gravity or magnetic constrained depth inversion with lateral and vertical variation of contrast. *Geophysics* 55: 327–335.

Clarke, G.K.C. 1971. Linear filters to suppress terrain effects on geophysical maps. *Geophysics* 36: 963–966.

Cole, J.W., and T.M. Hunt. 1968. Basaltic dikes of the Tarawera complex, New Zealand. *New Zealand Journal of Geology and Geophysics* 11: 1,203–1,206.

Connor, C.B., and B.E. Hill. 1993a. Estimating the probability of volcanic disruption at the Yucca Mountain site using nonhomogeneous Poisson models, *Focus '93*. La Grange, Park, IL: American Nuclear Society: 174–181.

Connor, C.B., and B.E. Hill. 1993b. *NRC High-Level Radioactive Waste Research at CNWRA. January 1–June 30, 1993. Chapter 10: Volcanism Research.* CNWRA 93-02S. San Antonio, TX: Center for Nuclear Regulatory Analyses.

Connor, C.B., and B.E. Hill. 1994. *The CNWRA Volcanism Geographic Information System Database.* CNWRA-94-004. San Antonio, TX: Center for Nuclear Waste Regulatory Analyses.

Connor, C.B., S.B. Lane, and B.M. Clement. 1993. Structure and thermal characteristics of the summit dome, March 1990—March, 1991. Special Volume on Volcán Colima, *Geofisíca Internacional* 32: 643–658.

Cooley, J.W., and J.W. Tukey. 1965. An algorithm for machine calculation of complex Fourier series. *Mathematical Computation* 19: 297–307.

Cote, L., J.O. Davis, W. Marks, R.J. McGough, E. Mehr, W.J. Pierson, J.F. Roper, G. Syephenson, and R.C. Vetter. 1960. The directional spectrum of a wind generated sea as determined from data by the stereowave observation project. *New York University Meteorological* Papers 2(6): 1–88.

Crowe, B.M., F.V. Perry, and G.A. Valentine. 1993. *Preliminary Draft: Status of Volcanic Hazard Studies for the Yucca Mountain Site Characterization Project.* Los Alamos, NM: Los Alamos National Laboratory.

Dean, W.C. 1958. Frequency analysis for gravity and magnetic interpretation. *Geophysics* 23: 97–127.

Dobrin, M.B., and C.H. Savit. 1988. *Introduction to Geophysical Prospecting*. New York, NY: McGraw-Hill.

Dubois, R.L., and W.W. Carey. 1964. Magnetic investigations of a ring dike, Buell Park, Arizona. *Geophysics* 29: 553–564.

Dzurisin, D., R.P. Denlinger, and J.G. Rosenbaum. 1990. Cooling rate and thermal structure determined from progressive magnetization of the dacite dome at Mount St. Helens, Washington. *Journal of Geophysical Research* 95: 2,763–2,780.

Flanigan, V.J., and C.L. Long. 1987. Aeromagnetic and near-surface electrical expression of Kilauea and Mauna Loa volcanic rift systems. R.W. Decker, T.L. Wright, and P.H. Stauffer, eds. *Volcanism In Hawaii*, USGS Professional Paper 1350: 935–946. Reston, VA: U.S. Geological Survey.

Flanigan, V.J., C.L. Long, D.H. Robert, and P.J. Mohr. 1986. *Aeromagnetic map of the rift systems of Kilauea and Mauna Loa volcanoes, Island of Hawaii.* USGS Miscellaneous Field Investigations Map MF-1845A. Reston, VA: U.S. Geological Survey.

Fuller, B.D. 1967. Two-dimensional frequency analysis and design of grid operators. *Mining Geophysics* 2: 658–708.

Godson, R.H., C.Z. Zablocki, H.A. Pierce, J.B. Fraser, C.M. Mitchell, and R.A. Sneddon. 1984. *Aeromagnetic map of the Island of Hawaii.* USGS Geophysical Investigations Map GP-946, Scale 1:250,000. Reston, VA: U.S. Geological Survey.

Goulty, N.R., T.E. Daley, K.G. Walters, and D.B. Emsley. 1984. Location of dykes in coalfield exploration. *First Break* 3(12): 15–21.

Grant, F.S. 1972. Review of data processing and interpretation methods in gravity and magnetics 1964–1971. *Geophysics* 37: 647–661.

Grant, F.S., and G.F. West. 1965. *Interpretation and Theory in Geophysics*. New York, NY: McGraw-Hill.

Grauch, V.J.S. 1985. Aeromagnetic terrain correction. *Geophysics* 50: 94–107.

Grauch, V.J.S., and D.L. Campbell. 1984. Does draping aeromagnetic data reduce terrain-induced effects? *Geophysics* 49: 75–80.

Grauch, V.J.S., and L. Cordell. 1987. Limitations of determining density or magnetic boundaries from the horizontal gradient of gravity or pseudogravity data. *Geophysics* 52: 118–121.

Gregotski, M.E., O. Jensen, and J. Arkani-Hamed. 1991. Fractal stochastic modeling of aeromagnetic data. *Geophysics* 56: 1,706–1,715.

Gunn, P.J. 1975. Linear transformations of gravity and magnetic fields. *Geophysical Prospecting* 23: 300–312.

Harrison, C.G.A. 1968. Formation of magnetic anomaly patterns by dyke injection. *Journal of Geophysical Research* 73: 2,137–2,142.

Hildenbrand, T.G. 1983. FFTFIL: *A Filtering Program Based on Two-Dimensional Fourier Analysis of Geophysical Data.* USGS Open-File Report 83–237. Reston, VA: U.S. Geological Survey.

Hildenbrand, T.G., and R.P. Kucks. 1988. Total-intensity magnetic anomaly map of Nevada. *Nevada Bureau of Mines and Geology*. Map 93A, Scale 1:750,000. Reston, VA: U.S. Geological Survey.

Hill, B.E., B.W. Leslie, and C.B. Connor. 1993. *A Review and Analysis of Dating Techniques for Neogene and Quaternary Volcanic Rocks.* CNWRA-93-018. San Antonio, TX: Center for Nuclear Waste Regulatory Analyses.

Hinze, W.J. 1985. *The Utility of Regional Gravity and Magnetic Anomaly Maps*. Society of Exploration Geophysicists: Tulsa, OK.

Hood, P. 1964. The Königsberger ratio and the dipping-dyke equation. *Geophysical Prospecting* 12: 440–456.

Huber, N.K. 1987. *Late Cenozoic Evolution of the Upper Amargosa River Drainage System, Southwestern Great Basin, Nevada and California.* USGS Open-File Report 87–617. Reston, VA: U.S. Geological Survey.

Kanasewich, E.R., and R.G. Agnarwal. 1970. Analysis of combined gravity and magnetic fields in the wavenumber domain. *Journal of Geophysical Research* 75: 5,702–5,712.

Kane, M.F., and R.E. Bracken. 1983. *Aeromagnetic map of Yucca Mountain and Surrounding Regions, Southwest Nevada.* USGS Open-File Report 83–616. Reston, VA: U.S. Geological Survey.

Kane, M.F., M.W. Webring, and B.K. Bhattacharyya. 1981. *A Preliminary Analysis of Gravity and Aeromagnetic Surveys of the Timber Mountain Area, Southern Nevada.* USGS Open-File Report 81-189. Reston, VA: U.S. Geological Survey.

Khurana, K.K., S.V.S. Rao, and P.C. Pal. 1981. Frequency domain least-squares inversion of thick dike magnetic anomalies using Marquardt algorithm. *Geophysics* 46: 1,745–1,748.

Kleiner, B., and T.E. Graedel. 1980. Exploratory data analysis in the geophysical sciences. *Reviews of Geophysics* 18: 699–717.

Ku, C.C., and J.A. Sharp. 1983. Werner deconvolution for automated magnetic interpretation and its refinement using Marquardt's inverse modeling. *Geophysics* 48: 754–774.

Kunaratnam, K. 1982. On: "Application of Gauss's method to magnetic anomalies of dipping dikes" by I.J. Won. *Geophysics* 47: 266–268.

Lane, S.B., B.M. Clement, G. Draper, and C.B. Connor. 1993. Three-dimensional physical and thermal structure of portions of the summit dome complex of Volcán Colima, Mexico, derived from magnetic investigations. *Eos, Transactions of the American Geophysical Union* 74: 688.

Langenheim, V.E., S.F. Carle, D.A. Ponce, and J.D. Phillips. 1991. *Revision of an Aromagnetic Survey in the Lathrop Wells Area, Nevada.* USGS Open-File Report 91–46. Reston, VA: U.S. Geological Survey.

Langenheim, V.E., K.S. Kirchoff-Stein, and H.W. Oliver. 1993. Geophysical investigations of buried volcanic centers near Yucca Mountain, Nevada. *Proceedings of the Third International High Level Radioactive Waste Management Conference.* La Grange Park, IL: American Nuclear Society. 1,840–1,846.

Li, Y., J.W. Geissman, A. Nur, H. Ron, and Q. Huang. 1990. Paleomagnetic evidence for clockwise block rotation in the northern Nevada rift. *Geology* 18: 79–82.

Lindsey, D.H., G.E. Andreasen, and J.R. Balsley. 1966. Magnetic properties of rocks and minerals. S.P. Clark eds. *Handbook of Physical Constants*, Geological Society of America Memoir 97: 543–552.

Marobhe, I.M. 1990. Application of the Hartley transform to the interpretation of magnetic anomalies due to two-dimensional dyke bodies. *Geoexploration* 26: 291–301.

Marsh, B.D. 1971. *Aeromagnetic Terrain Effects.* M.S. Thesis. Pheonix, AZ: University of Arizona.

McDuffie, S.M., C.B. Connor, and K.D. Mahrer. 1994. A simple model for dike fracture interaction. *Eos, Transactions of the American Geophysical Union* 75: 345.

McKee, E.H., and R.J. Blakely. 1990. Tectonic significance of north trending anomalies in north-central Nevada. *Geology and Ore Deposits of the Western Great Basin.* Geological Society of Nevada and the U.S. Geological Survey, Program with Abstracts: 49.

Murthy, I.V.R. 1985. The midpoint method: Magnetic interpretation of faults and dikes. *Geophysics* 50: 834–839.

Nishida, Y., and E. Miyajima. 1984. Subsurface structure of Usu volcano, Japan, revealed by detailed magnetic survey. *Journal of Volcanology and Geothermal Research* 22: 271–285.

Nunziata, C., and A. Rapolla. 1987. A gravity and magnetic study of the volcanic island of Ischia, Naples (Italy). *Journal of Volcanology and Geothermal Research* 31: 333–344.

Nunziata, C., and A. Rapolla. 1981. Interpretation of gravity and magnetic data in the Phlegraen Fields geothermal area, Naples, Italy. *Journal of Volcanology and Geothermal Research* 10: 209–225.

Oliver, H.W., E.L. Hardin, and P.H. Nelson. 1990. *Status of Data, Major Results, and Plans for Geophysical Activities, Yucca Mountain Project.* Springfield, VA: U.S. Department of Commerce: National Technical Information Service.

Pal, P.C. 1985. A gradient analysis-based simplified inversion strategy for the magnetic anomaly of an inclined and infinite thick dike. *Geophysics* 50: 1,179–1,182.

Paterson, N.R., and C.V. Reeves. 1985. Applications of gravity and magnetic surveys: the state of the art in 1985. *Geophysics* 50: 2,558–2,594.

Payne, M.A. 1981. SI and Gaussian CGS units, conversions and equations for use in geomagnetism. *Physics of the Earth and Planetary Interiors* 26: 10–16.

Plouff, D. 1975. *Derivation of formulas and FORTRAN programs to compute magnetic anomalies due to prisms.* USGS Report No. USGS-GD-75-014. Springfield, VA. National Technical Information Service.

Plouff, D. 1976. Gravity and magnetic fields of polygonal prisms and application to magnetic terrain corrections. *Geophysics* 41: 727–741.

Poisson, S.D. 1826. Memoire sur la theorie du magnetisme. *Memoires de l'Academie Royale des Sciences de l'Institut de France.* 247–348.

Ponce, D.A., S.B. Kohrn, and S. Waddell. 1992. Gravity and magnetic data of Fortymile Wash, Nevada Test Site, Nevada. USGS Open-File Report 92–343. Reston, VA: U.S. Geological Survey

Rao, B.S.R., I.V.R. Murthy, and C. V. Rao. 1973. Two methods for computer interpretation of magnetic anomalies of dikes. *Geophysics* 38: 710–718.

Rao, D.B., and N.R. Babu. 1991. A rapid method for three-dimensional modeling of magnetic anomalies. *Geophysics* 56: 1,729–1,737.

Rao, D.B., and N.R. Babu. 1993. A Fortran-77 computer program for three-dimensional inversion of magnetic anomalies resulting from multiple prismatic bodies. *Computers and Geosciences* 19: 781–801.

Rao, D.B., and N.R. Babu, and P.V.S. Narayan. 1981. Interpretation of magnetic anomalies due to dikes: the complex gradient method. *Geophysics* 46: 1,572–1,578.

Rao, T.K.S., and M. Subrahimanyam. 1985. Error analysis for the expression of vertical magnetic effect of finite tabular model of Grant and West (1965). *Geophysical Research Bulletin* 23: 225–247.

Rikitake, T., and Y. Hagiwara. 1965. Magnetic anomaly over a magnetized circular cone. *Bulletin of the Earthquake Research Institute* 43: 509–527.

Rosenbaum, J.G. 1986. Paleomagnetic directional dispersion produced by plastic deformation in a thick Miocene welded tuff, southern Nevada: implications for welding temperatures. *Journal of Geophysical Research* 89: 9,411-9,413.

Roest, W.R., and M. Pilkington. 1993. Identifying remanent magnetization effects in magnetic data. *Geophysics* 58: 653-659.

Rout, D.J., J. Cassidy, C.A. Lock, and I.E.M. Smith. 1993. Geophysical evidence for temporal and structural relationships within monogenetic basaltic volcanoes of the Auckland volcanic field, northern New Zealand. *Journal of Volcanology and Geothermal Research* 57: 71-83.

Sclinger, C.M., J.G. Rosenbaum, and D.R. Veblen. 1988. Fe-oxide microcrystals in welded tuff from southern Nevada: origin of remanence carriers by precipitation in volcanic glass. *Geology* 16: 556-559.

Scott, R.B., and J.G. Rosenbaum. 1986. Evidence of rotation about a vertical axis during extension at Yucca Mountain, southern Nevada. *Eos, Transactions of the American Geophysical Union* 67: 358.

Serpa, L.F., and K.L. Cook. 1984. Simultaneous inversion modeling of gravity and aeromagnetic data applied to a geothermal study in Utah. *Geophysics* 49: 1,327-1,337.

Shurbet, D.H., G.R. Keller, and J.P. Friess. 1976. Remanent magnetization from comparison of gravity and magnetic anomalies. *Geophysics* 41: 56-61.

Smith, E. 1994. Recent studies in Crater Flat Valley. *Nuclear Waste Technical Review Board Meeting*. San Francisco, CA.

Smith, E., D. Feuerbach, T. Naumann, and J. Faulds. 1990. The area of most recent volcanism near Yucca Mountain, Nevada: Implications for volcanic risk assessment. *High Level Radioactive Waste Management. Proceedings of the International Topical Meeting, 1990, Volume 1.* La Grange Park, IL: American Nuclear Society: 81-90.

Spector, A., and F.S. Grant. 1970. Statistical models for interpretation of aeromagnetic data. *Geophysics* 35: 293-302.

Talwani, M. 1965. Computation with the help of a digital computer of magnetic anomalies caused by bodies of arbitrary shape. *Geophysics* 30: 797-817.

Talwani, M., and J.R. Heirtzler. 1964. Computation of magnetic anomalies caused by two-dimensional structures of arbitrary shape. G.A. Parks ed. *Computers in the Mineral Industries*. Stanford, CA. Stanford University Press: 464-480.

Tanaka, K.L., T.C. Onstott, and E.M. Shoemaker. 1990. Magnetostratigraphy of the San Francisco volcanic field, Arizona. USGS Bulletin 1929. 15. Reston, VA: U.S. Geological Survey.

Tarling, D.H. 1983. *Geomagnetism*. London, England: Chapman and Hall.

Tukey, J.W. 1977. *Exploratory Data Analysis*. Reading, MA. Addison-Wesley.

Walker, G.E., and T.E. Eakin. 1963. Geology and ground water of Amargosa Desert, Nevada-California. *State of Nevada Department of Conservation and Natural Resources Ground Water Resources - Reconnaisance Series Report* 14.

Webring, M. 1985. SAKI: *A Fortran Program for Generalized Linear Inversion of Gravity and Magnetic Profiles*. USGS Open-File Report 85-122. Reston, VA: U.S. Geological Survey.

Xia, J., and D.R. Sprowl. 1992. Inversion of potential-field data by iterative forward modeling in the wavenumber domain. *Geophysics* 57: 126–130.

Young, R.A., and J.E. Lucas. 1988. Exploration beneath volcanics: Snake River Plain, Idaho. *Geophysics* 53: 444–452.

Zeyen, H.J., E. Banda, and E. Klingelé. 1991. Interpretation of magnetic anomalies in the volcanic area of northeastern Spain. *Tectonophysics* 192: 201–210.

Zoback, M.L., and G.A. Thompson. 1978. Basin and Range rifting in northern Nevada: Clues from a mide-Miocene rift and its subsequent offsets. *Geology* 6: 111–116.

Zoback, M.L., E.H. McKee, R.J. Blakely, and G.A. Thompson. 1994. The northern Nevada rift: Regional tectono-magmatic relations and middle Miocene stress direction. *Geological Society of America, Bulletin* 106: 371–382.